Università degli Studi Roma Tre

Department of Mathematics and Physics

Doctoral Program in Physics - XXXIV Cycle

A thesis submitted for the degree of
Doctor of Philosophy in Physics

Search for a visibly decaying Z' dark boson at Belle II in $e^+e^- \to \mu^+\mu^-\mu^+\mu^-$ events

Supervisor:
Enrico Graziani

Author:
Martina Laurenza

PhD Program Coordinator:
Giuseppe Degrassi

Contents

List of Figures

List of Tables

Abstract

The Standard Model (SM) of fundamental particles and interactions is a highly predictive theory. Despite this, it cannot be considered as a complete description of the nature, because of the many observed phenomena which are not taken into account. Among these phenomena not predicted by the SM, there are observations which could be explained through the presence of Dark Matter (DM). Many theoretical models postulate extensions of the SM with the aim of including the phenomenology associated to DM and predict the observed relic abundance. One of the simplest ways to extend the SM is by adding an extra $U(1)'$ gauge group to the theory. An additional gauge boson, the Z' , would rise and couple to both SM and undiscovered particles such as dark matter constituents [1, 2, 3, 4].

The work described here considers the visible decay of a Z' boson in the framework of the so-called $L_\mu - L_\tau$ model [4, 5], which gauges the difference between the muonic and tauonic lepton numbers. Under a $L_\mu - L_\tau$ symmetry, the Z' boson would couple only to μ, τ and the respective ν_μ and ν_τ neutrinos among the SM particles, with a coupling constant g'.
Two theoretical models based on the $L_\mu - L_\tau$ symmetry address the DM topic. They are identical from the mediator point of view (the Z') and differ as far as DM candidates are concerned: these are sterile neutrinos in one case [4] and light Dirac fermions in the other [3].
Two additional benefits of the $L_\mu - L_\tau$ model are its capability of explaining the observed discrepancy of the muon anomalous magnetic moment $(g-2)_\mu$ with respect to the SM prediction and of solving the flavour anomalies measured by the LHCb experiment.

Belle II operates at the SuperKEKB electron-positron collider [6] at the KEK laboratory in Tsukuba, Japan. Belle II is recording data since April 2018, mainly at the center-of-mass energy of the $\Upsilon(4S)$ resonance peak. Up to now the total integrated luminosity collected by the Belle II is 267.9 fb^{-1}.

The analysis aims at the investigation of the visible decay of the Z' into a muon pair in the reaction $e^+e^- \to \mu^+\mu^- Z'$ ($Z' \to \mu^+\mu^-$), in order to discover it or to set an upper limit on the coupling constant g'. The same search was performed by *BABAR* [7] and the Belle experiments, with $\sim$500 fb^{-1} and $\sim$640 fb^{-1}, respectively.

The work introduced here is based on a target luminosity of 54 fb^{-1} and was performed without looking at the data in the signal region. The entire 267.9 fb^{-1} Belle II data-set was not used because of the different reconstruction and trigger configurations, that would have required more time to be taken into account in the analysis. The final goal is to demonstrate that it is possible to set competitive or better limits with respect to the experiments results employing a different background reduction approach.

It will be shown later that such a luminosity is not sufficient to get a sensitivity

better than those of *BABAR* and Belle. For this reason, the analysis has not obtained the Belle II collaboration approval yet. Nevertheless, explicitly for this thesis, the permission to look at the 10% of the target luminosity has been granted, with the prescriptions that the performances of the analysis and the partial results obtained on real data in the signal region cannot be shown elsewhere. The projections of the g' coupling constant sensitivity using $54\,\text{fb}^{-1}$ and $200\,\text{fb}^{-1}$ are shown. With the latter we can set more restrictive limits on the coupling constant with respect to both *BABAR* and Belle, for Z' masses larger than 1 GeV/c^2, with much less luminosity.

Chapter 1

Theoretical overview and motivations

The Standard Model (SM) of elementary particles is the current theory that best describes the fundamental forces that rule the microscopic world. This theory is able to explain and predict all physics effects observed at a fundamental level, but at very different energy and space scales, astronomical and cosmological measurements reveal large effects non-explainable with SM interactions. Some of these macroscopic effects could have a microscopical origin out of SM theory. Examples are the *baryon asymmetry* (asymmetry between baryonic matter and antibaryonic matter in the observable universe, not explainable with CP violation from SM source), or *dark matter* (anomalies in gravitational effects explainable with a not-electromagnetic matter). Besides, several SM measurements show some tensions with respect to theoretical expectation, even if they are experimentally not significant enough to claim the discovery of New Physics.

In this chapter an overview on the SM and an introduction on dark matter are given.

1.1 The Standard Model

The Standard Model of particle physics is the best available theory to describe in the coherent framework of the Quantum Field Theory all the known fundamental particles (Figure 1.1) and three out of four of the fundamental interactions. These are briefly introduced in the following:

- the **strong interaction**, responsible for hadronic and nuclear binding;
- the **electromagnetic interaction**, is the only long-range force in the SM. It is well described by quantum electrodynamics. Electromagnetism is responsible for a wide range of phenomena including atomic electron shell structure, chemical bonds, electric circuits and electronics;
- the **weak interaction**, that accounts for many decays in particle physics.

Electromagnetic and weak force arise from the same symmetry group of the theory and can be treated as a single force, called *electroweak interaction*. The **gravitational**

interaction is too weak at the particle physics energy scales, and is not incorporated in the SM.

According to the SM, the elementary particles are divided in two groups: *fermions* and *bosons*.

Fermions

They have half-integer spin and are the constituents of matter. According to the spin–statistics theorem, fermions observe the Pauli exclusion principle. Each fermion has a corresponding antiparticle. They can be further divided in two categories: *quarks* and *leptons*.

Quarks. They interact through electroweak and strong forces. Quarks are classifiable in 3 generations of doublets. Each doublet contains an up-type quark with electric charge $\frac{2}{3}e$ and a down-type quark with electric charge -$\frac{1}{3}e$, where $e \approx 1.602 \cdot 10^{-19}$ C is the absolute value of the charge of the electron.

Different kind of quarks are classified according to a quantum number. The doublets are:

$$\begin{pmatrix} u \\ d \end{pmatrix} , \begin{pmatrix} c \\ s \end{pmatrix} , \begin{pmatrix} t \\ b \end{pmatrix} ,$$

where the letters correspond to *up*, *down*, *charm*, *strange*, *top*, *bottom*. They indicate the quantum numbers of the quarks, which are called flavour. Flavour quantum number is conserved in the strong and electromagnetic interaction, but not in the weak one. In this picture, 6 quantum numbers are assigned to each quark, with all values set to 0 except the one corresponding to its kind, that will be +1 for up quarks, -1 for down quarks (for example, a charm quark has $U = D = S = T = B = 0$ and $C = 1$, instead a bottom quark has $U = D = C = S = T = 0$ and $B = -1$). For each generation exists a completely specular generation of antiquarks (since quarks are $\frac{1}{2}$-spin fermions, they follow the Dirac equation), with reversed flavour number, electric charge, and color.

Isolated quarks are not observable because of color-confinement principle of QCD (all observable particles isolated must be colorless), but a bound state of one quark and one antiquark (*meson*) or a bound state of three quark (*baryon*) can be colorless and so observable as isolated states.

The number of quarks is not conserved in the SM processes, but the difference $N_q - N_{\bar{q}}$ is constant, implying that the lightest baryon (the proton) must be stable in the SM and that the baryon number N_B is a conserved quantity within the SM framework.

Leptons. They only interact through the electroweak force. They are classified in 3 generations of doublets:

$$\begin{pmatrix} e \\ \nu_e \end{pmatrix} , \begin{pmatrix} \mu \\ \nu_\mu \end{pmatrix} , \begin{pmatrix} \tau \\ \nu_\tau \end{pmatrix} ,$$

where each doublet is composed by a charged and massive lepton (with electric charge $-e$) and a massless and neutral neutrino. Three more quantum numbers called *lepton family number* (L_e, L_μ, L_τ) are defined. The lepton family number is conserved

in all the interactions included in the SM but in the neutrino oscillation process, which however is not included in the simplest version of the SM, but in an extension of it. Each lepton has the lepton family number of its generation equal to 1 and the numbers of the other generation equal to 0, in analogy with the quark flavour quantum number. Lepton number L is defined as the sum of lepton family number. As quarks, leptons have corresponding antileptons (with reversed electric charge and lepton family number).

Bosons.

Gauge bosons. In the SM gauge bosons are defined as *force carriers* that mediate the strong, weak, and electromagnetic fundamental interactions. They all have integer spin, equal to 1, so they do not follow the Pauli exclusion principle that constrains fermions. For this reason, bosons do not have a theoretical limit on their spatial density. The SM gauge bosons are the following:

- **gluons (g)**: they are massless bosons, mediating strong interaction through quarks. They exist in 8 color states, according to the Quantum Chromodynamic (QCD), the theory of strong interaction. The strong charge is called color and exists in three kinds, so that all colored particles interact strongly. Since gluons carry color charge they can interact with themselves. Through gluons, the strong force delineates the binding of the u, d and s quarks in mesons and baryons;

- **Photons (γ)**: they are massless boson mediating electromagnetic force between electrically charged particles. The photon is well described by the theory of *quantum electrodynamics*. They have 0 charge, so cannot interact with themselves;

- **W^+, W^- and Z^0 bosons**: mediate the weak interactions between particles of different flavours. They are massive, with the Z being more massive than the $W^{\pm}$;

Higgs boson. The Higgs Boson H is a scalar, electrically neutral and massive particle. The complex scalar field of the Higgs boson has non-zero vacuum expectation value, which induces the generation of the mass of the SM particles coupling with it. The Higgs boson explains why the photon has no mass, while the $W^{\pm}$ and Z^0 bosons are very heavy. The result is a non-trivial hierarchy of mass between the particles of the SM: the massive bosons have masses in the scale of 100 GeV/c^2, the quarks cover from few MeV/c^2 to about 173 GeV/c^2 of quark t and the massive leptons from about 0.5 MeV/c^2 to about 1.7 GeV/c^2 (in Figure 1.1 precise values are shown).

For both, quark and leptons, the three generations appear as three copies of the same structure that only differ in mass (and therefore in available decays and lifetime). This feature allows to state the *lepton universality* for leptons, meaning that the coupling of leptons to all types of gauge bosons are flavour-independent. This is not true for quarks generations, for which there are differences in couplings that generate the phenomenology of heavy flavour physics.

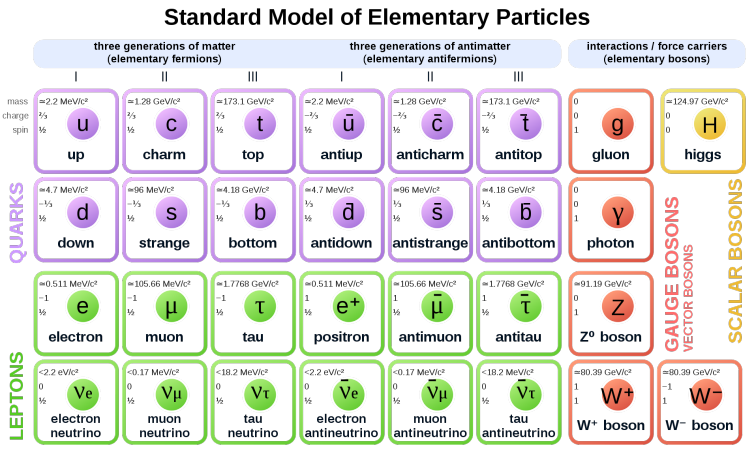

Figure 1.1: Summary table of elementary particles of SM and their classifications. Picture from: *Wikipedia.org*.

1.1.1 Brief introduction to the Standard Model Lagrangian

The *Quantum Field Theory* provides the mathematical framework for the SM, in which a Lagrangian controls the dynamics and kinematics of the theory. Each kind of particle is described in terms of a dynamical field. These fields are:

- the **fermion fields** ψ, which account for matter particles;
- the **electroweak boson fields** W_1, W_2, W_3 and B;
- the **gluon field** G_a;
- the **Higgs field** φ.

Furthermore, the SM is a gauge theory based on the local symmetry group:

$$SU(3)_C \otimes SU(2)_L \otimes U(1)_Y \ ,$$

where $SU(3)_C$ is the gauge group of QCD and acts on G_a (where the subscript C is for "color"), $SU(2)_L \otimes U(1)_Y$ is the gauge group of electroweak theory, and $SU(2)_L$ acts on $W_{1,2,3}$ and φ, and $U(1)_Y$ acts on B and φ (where the subscript L is for "left" and Y is for "hypercharge"). The dynamics of the quantum state and the fundamental fields are determined by the Lagrangian density $\mathcal{L}$. The terms that compose the lagrangian density will be briefly described below:

Kinetic terms

The first term is the sum of the *kinetic terms*. They take into account the gauge bosons self interactions:

$$\mathcal{L}_{\text{kin}} = -\frac{1}{4} B_{\mu\nu} B^{\mu\nu} - \frac{1}{2} \text{tr} W_{\mu\nu} W^{\mu\nu} - \frac{1}{2} \text{tr} G_{\mu\nu} G^{\mu\nu}, \tag{1.1}$$

where:

- the **gluon field tensor** is represented by $G_{\mu\nu}$;
- the **gauge field tensor of SU(2)** is denoted by $W_{\mu\nu}$;
- $B_{\mu\nu}$ represents the **gauge field tensor for the U(1)** of weak hypercharge.

Coupling terms

Coupling terms allow for the coupling between gauge field to the fermions. These terms are the responsible for interactions.

The Dirac Lagrangian describes the interactions between quarks and gluons and is given by:

$$\mathcal{L}_{\mathcal{QCD}} \;=\; \sum_{\psi} \bar{\psi}_i \left(i\gamma^\mu \left(\partial_\mu \delta_{ij} - i g_s G^a_\mu T^a_{ij} \right) \right) \psi_j \;-\; \frac{1}{2} G^a_{\mu\nu} G^{\mu\nu}_a, \tag{1.2}$$

where:

- ψ is the Dirac spinor of the quark field, where $i = r, g, b$ represents color;
- γ_μ are the Dirac matrices;
- $G_{a\mu}$ is the 8-component SU(3) gauge field;
- T^a_{ij} are the 3×3 Gell-Mann matrices, generators of the SU(3) color group;
- $G^a_{\mu\nu}$ represents the gluon field strength tensor;
- g_s is the strong coupling constant.

The electroweak interaction, instead, is described by:

$$\mathcal{L}_{\mathcal{EW}} \;=\; \sum_{\psi} \psi\gamma^\mu \left(i\partial_\mu - g' \frac{1}{2} Y_W B_\mu - g \frac{1}{2} \vec{\tau}_L \vec{W}_\mu \right) \psi \;-\; \frac{1}{4} W^{\mu\nu}_a W^a_{\mu\nu} \;-\; \frac{1}{4} B^{\mu\nu}_a B^a_{\mu\nu}, \tag{1.3}$$

where:

- B_μ is the U(1) gauge field;
- Y_W is the weak hypercharge, the generator of the U(1) group;
- $\vec{W}_\mu$ is the 3-component SU(2) gauge field;
- $\vec{\tau}_L$ are the Pauli matrices, with subscript L to indicate that they only act on left-chiral fermions;
- g' and g are the U(1) and SU(2) coupling constants respectively;
- $W^{a\mu\nu}$ are the field strength tensors for the weak isospin and weak hypercharge fields. (a=1,2,3) and $B^{\mu\nu}$ are the field strength tensors for the weak isospin and weak hypercharge fields.

Higgs mechanism

As already mentioned in the previous paragraphs, inside the lagrangian of the SM, there is a kinetic term (see Equations 1.1) of free field for B, W and G and a dynamical term of interaction between fermions and boson fields (see Equations 1.2 and 1.3).

A trivial mass term in the form $C^\mu C_\mu$ (where C is a generic field) is forbidden to keep the theory gauge invariant. The solution to this problem comes from the *Higgs mechanism*, which involves a complex scalar field ϕ:

$$\phi = \frac{1}{\sqrt{2}} \begin{pmatrix} \phi^+ \\ \phi^0 \end{pmatrix}, \tag{1.4}$$

where the superscripts + and 0 indicate the electric charge (Q) of the components. The Higgs part of the lagrangian is:

$$\mathcal{L}_H = \left[\left(\partial_\mu - i g W^a_\mu t^a - i g' Y_\phi B_\mu \right) \phi \right]^2 + \mu^2 \phi^\dagger \phi - \lambda (\phi^\dagger \phi)^2, \tag{1.5}$$

where $\lambda > 0$ and $\mu^2 > 0$ allow for the spontaneous symmetry breaking. This spontaneous symmetry breaking mechanism gives to the Higgs field a non-vanishing vacuum expectation value that represents a mass-scale of the model. In conclusion, the Higgs mechanism mix the four electroweak fields to obtain three massive fields, $W^{\pm}$ charged fields and the Z^0 field, and the photon massless field A (with own symmetry group $U(1)_{EM}$).

The Higgs mechanism can be extended to give to the fermions their masses adding a Yukawa term in the lagrangian:

$$\mathcal{L}_{\mathrm{YU}} = \overline{U}_{\mathrm{L}} G_{\mathrm{u}} U_{\mathrm{R}} \phi^0 - \overline{D}_{\mathrm{L}} G_{\mathrm{u}} U_{\mathrm{R}} \phi^- + \overline{U}_{\mathrm{L}} G_{\mathrm{d}} D_{\mathrm{R}} \phi^+ + \overline{D}_{\mathrm{L}} G_{\mathrm{d}} D_{\mathrm{R}} \phi^0 + \mathrm{h.c.}, \tag{1.6}$$

where $G_{u,d}$ are 3×3 matrices of Yukawa couplings, with the ij term giving the coupling of the generations i and j. The mass scales of the fermions (the coupling constant of these terms) are free parameters of the SM.

Neutrino masses. Since a right-handed neutrino does not exist, the Yukawa coupling would be ineffective and the neutrino would not get mass from the interaction. Nevertheless, there are experimental evidence that assert that neutrinos do have mass. A possible solution is to add a right-handed neutrino the theory: ν_R. This field however must be a sterile neutrino, since being right-handed it experimentally belongs to an isospin singlet ($T_3 = 0$) and also has charge Q = 0, implying $Y_W = 0$, thus it does not even participate in the weak interaction. Another possibility to consider is that the neutrino satisfies the Majorana equation, where essentially left-handed neutrinos and right-handed anti-neutrinos are flipped.

Both this theories would lie in an extension of the SM.

C, P and T symmetries

The SM does not have any of the simpler discrete symmetries:

- the **charge conjugation** C which inverts all the internal quantum numbers of a particle transforming particle into its antiparticle;
- the **parity operator** P which reverses the spatial coordinate and momenta of a particle;
- the **time reversal** T which inverts the arrow of time are not conserved in the SM processes.

.

The electroweak interaction violates also the combination of the two symmetries C and P (CP violation). Instead the combination of the three symmetries CPT is a symmetry of the SM.

1.2 Dark Matter

Astrophysical and cosmological observations of Dark Matter (DM) are perhaps the most persuasive experimental evidence of physics beyond the SM. DM may not be composed of particles at all (an example is primordial black holes), but the success of

the SM in describing ordinary matter gives us a strong reason to consider a particle description of DM as well.

Although there are several indirect evidences of its existence at different scales, very little is known about DM. Accordingly to the standard cosmological model DM constitutes about 25% of the energy density of our universe (being 5 times more abundant with respect to the known SM matter) [8] and also that has a key role in the comprehension of the evolution of the universe itself. Unlike normal matter, DM does not interact with the electromagnetic force. This means it does not absorb, reflect or emit light, making it extremely hard to spot. Moreover, we know that DM is likely coupled to SM particles [9], as well as by gravitational force, at most at the weak interaction scale and is stable on cosmological timescales. Most of the DM properties are still unknown.

Evidences of dark matter

The first and oldest evidence of the DM existence concerns the observation of the rotational velocity of galaxies, which could not be explained by only the barionic visible mass. Rubin and collaborators extensively studied more than 60 galaxies [10], measuring the rotational velocity from the analysis of the spectral lines (Doppler effect). In absence of invisible mass, the velocity of stars in the galaxy should be described as the velocity of our planet around the Sun, thus $v(r) = \sqrt{Gm(r)/r}$, where $v(r)$ is the velocity, G is the gravitational constant and $m(r)$ is the mass within a radius r. The dependence from the radius goes as $1/\sqrt{r}$, decreasing as the distance from the center increases. Surprisingly the data observed showed a flat behaviour, meaning that the velocity does not decrease with increasing distances. The expected and observed behaviours are shown in Figure 1.2. The agreement is restored if an invisible massive halo fills all the space and it is not concentrated, as the ordinary mass, close to the central bulge of the galaxy.

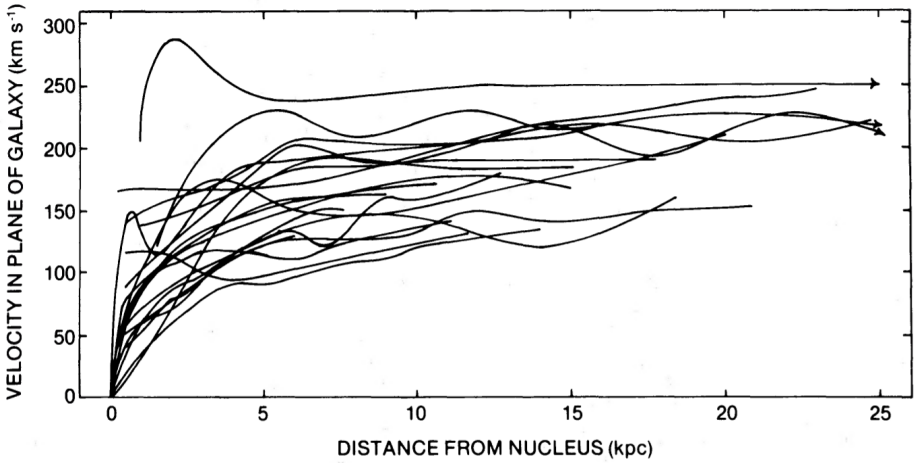

Figure 1.2: Rotational velocity of the galaxies (measured by Rubin and collaborators) as a function of their radius [10].

The second evidence derives from the observation of the gravitational lensing effect. This effect is due to the deformation of the space-time in presence of a mass affecting the motion of bodies and light. Gravitational lensing effect allows, due to the bending

of the light, to spot objects placed directly behind a closer one. Without entering into details, from the reconstructed image of the hidden object it is possible to determine the amount of mass generating the gravitational effect. As an example, observations performed on Abell 370 cluster (Figure 1.3) led to an estimation of the total mass of the cluster to be between 10^2 and 10^3 times the observed one [11].

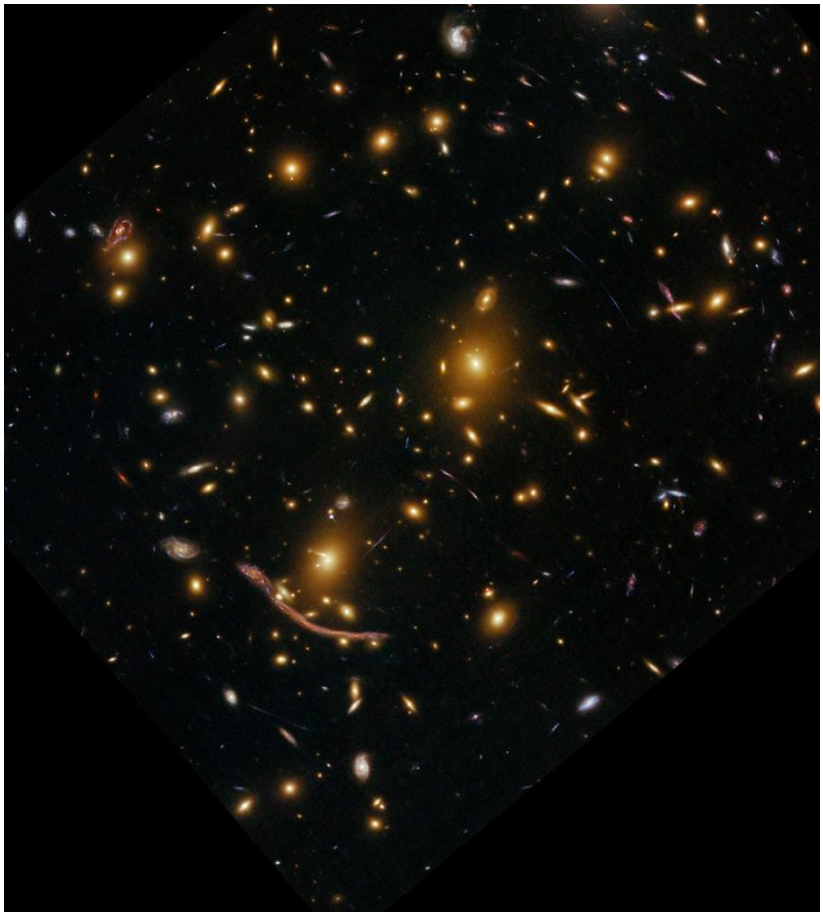

Figure 1.3: Abell 370: galaxy cluster gravitational lens observed in 2009. Picture from: *Esa/Hubble*

Other important evidences are provided by the measurement of the anisotropies in the cosmic microwave background and by collisions of a galaxy cluster, called "bullet", with a bigger one.

Detection methods

Currently there are three possible experimental methods used to investigate the particle nature of DM: **direct detection**, **indirect detection** and **direct production** at colliders (see Figure 1.4).

DM **direct detection** is based on the observation of the nuclear recoils rising from the DM scattering in terrestrial detectors. The experimental setup typically includes a huge detector which has to be optimized to minimize the background contamination: the most important background sources usually come from cosmic rays, natural radioactivity and the intrinsic radioactivity of the detector. The DM interaction with the detector's nuclei can have different features: it could be either elastic or inelastic,

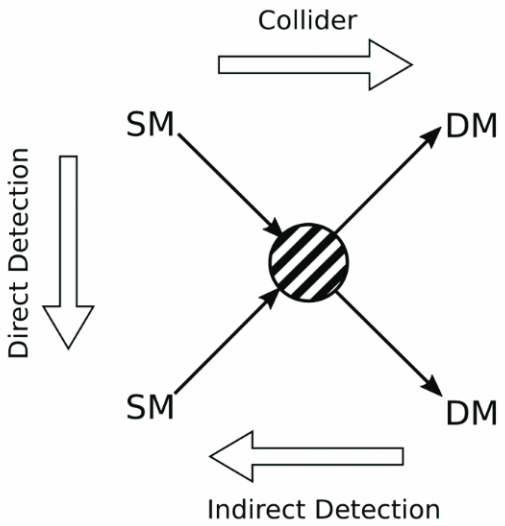

Figure 1.4: Scheme of possible dark matter detection methods.

spin-dependent or spin-independent. Up to now, experiments of direct detection just came to set upper and lower limits of the DM mass and couplings, without revealing their nature.

The idea behind the **indirect detection** is to detect the SM particles produced in the annihilation of DM particles far in the universe, that occurs with a high probability in regions of space with high density of DM, like galaxy centers. Antiparticles, neutrinos and gamma rays are the most useful annihilation products to be detected. For this reason the indirect strategy focuses on finding an excess in the flux of the annihilation products. Identifying the possible source of the flux and observe whether it could be a region containing a large density of DM or not helps to discriminate between background and DM decay products.

Assuming that DM particles interacts with the SM ones, they can also be **produced at colliders**. DM particles have to be stable and, as they only interact weakly with ordinary matter, they escape the detector. However, the presence of a DM particle would leave a distinctive signature inside the detector: as DM escapes detection, an energy inbalance is expected to be measured.

1.3 Dark mediators and portals

In many models, DM particles couple to SM through the effect of new dark mediators. Depending on the type of the dark mediator, different "portals" between the SM and the DM particles can be identified:

- a *scalar portal*, in which a new scalar particle S can couple to the SM Higgs field φ: $\mathcal{L} \supset \mu S\varphi^\dagger\varphi + \lambda S\varphi^\dagger\varphi$; if this scalar acquires a vacuum expectation, it can mix with the SM Higgs;

- a *pseudoscalar portal*, in which a new pseudoscalar particle a can couple to the SM fermionic fields ψ: $\mathcal{L} \supset (\partial_\mu a/f_a)\bar{\psi}\gamma^\mu\gamma^5\psi$; this term is obtained, for example, from the spontaneous breaking of a global symmetry, where f_a is the scale at which the symmetry is broken, and if the scale f_a is sufficiently large, the pseudoscalar particle naturally obtains a small mass and small couplings; in

addition to fermionic couplings, this kind of mediator generally induces couplings to the SM gauge bosons: $\mathcal{L} \supset -\sum_i (\alpha_i C_i / 8\pi f_a) F_{(i)\,\mu\nu} \tilde{F}^{\mu\nu}_{(i)} a$, where $i = Y, 2, 3$ labels the different gauge groups of the SM, $F_{(i)\,\mu\nu}$ denotes the corresponding field strength tensor and $\tilde{F}^{\mu\nu}_{(i)}$ is the dual field strength tensor;

- a *neutrino portal*, in which a new fermionic particle N can coupe to the SM fields: $\mathcal{L} \supset y_N L \varphi N$, where y_N is the Yukawa coupling and L is the $SU(2)_L$ fermionic doublet; in this case, N can be an heavy (sterile) right handed neutrino, typically invoked for generating a SM neutrino mass term;

- a *vector portal*, in which a new vector particle A' can couple to the SM fermionic fields: $\mathcal{L} \supset g' \bar{\psi} \gamma^\mu \psi A'_\mu$, where g' is the coupling constant of the new interaction; the A' can also couple with the ordinary SM photon through the kinetic mixing mechanism: $\mathcal{L} \supset (\epsilon/2) A'_{\mu\nu} F_Y^{\mu\nu}$, where ϵ is the kinetic mixing parameter and $A'_{\mu\nu}$ ($F_Y^{\mu\nu}$) is the field strength tensor of the A' (hypercharge) vector field.

Each of the new aforementioned particles might be also viable DM candidates [12], provided that they are sufficiently light and their couplings to the SM are so small that it appears stable on cosmological timescales.

Depending on the details of the model, the introduced mediators can couple to both quarks and leptons, only to quarks (*leptophobic*) or only to leptons (*leptophilic*). In principle, they can also couple with different strength to down-type quarks and to up-type quarks. The scalar mediators are furthermore expected to couple to fermions proportional to their mass.

The crucial point is that - in contrast to DM candidates, the mediators responsible of the portal interactions may have sizeable couplings to the SM, which can potentially be probed in particle colliders through the direct production. Once produced, mediators can have three different types of decays:

1. invisible decays;
2. leptonic decays;
3. hadronic decays.

If the DM mass is less than half of the mediator mass, the first decay mode is expected to be dominant and the production of the mediator will lead to missing energy/momentum in the detector. If invisible decays are kinematically forbidden, there will typically be both leptonic and hadronic decays (unless of course the mediator is either leptophilic or leptophobic). For scalar mediators the leptonic decay modes will be dominated by the heaviest lepton that is kinematically accessible, while vector mediators are usually postulated to couple more democratically with all the available leptons. Calculating the hadronic branching fractions for mediators in the GeV range is a difficult problem due to the onset of non-perturbative effects.

1.3.1 The $L_\mu - L_\tau$ model

In the framework of the vector portal extension of the SM, it is of particular interest the introduction of a dark boson Z' with mass of $\mathcal{O}(\text{MeV}) - \mathcal{O}(\text{GeV})$ through a theoretically well motivated model called $L_\mu - L_\tau$ [13, 14]. In this model the Z' has a coupling only to the second and third generation of leptons through the lagrangian term:

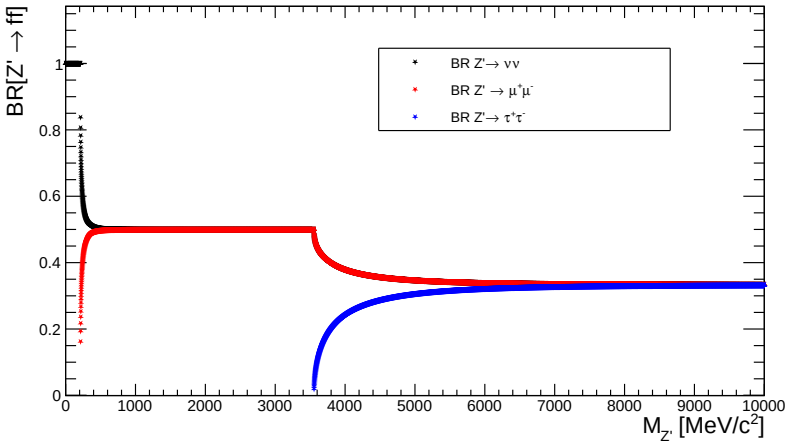

Figure 1.5: $BR(Z' \rightarrow ff)$ as a function of the Z′ mass [15]. The $\nu\bar{\nu}$ BR includes both ν_μ and ν_τ.

$$\mathcal{L} = \sum_l \theta g' \bar{l} \gamma^\mu Z'_\mu l,$$

where $\theta = +1$ if $l = \mu, \nu_\mu$, $\theta = -1$ if $l = \tau, \nu_\tau$, and $g' \sim 10^{-6} - 10^{-2}$. Such a Z′ does not couple with e and ν_e.
The equations for the partial widths are

$$\begin{aligned} \Gamma_{Z' \rightarrow l^+ l^-} &= \frac{(g')^2 M_{Z'}}{12\pi} \left(1 + \frac{2m_l^2}{M_{Z'}^2}\right) \sqrt{1 - \frac{4m_l^2}{M_{Z'}^2}} \theta(M_{Z'} - 2M_l) \\ \Gamma_{Z' \rightarrow \nu\bar{\nu}} &= \frac{(g')^2 M_{Z'}}{24\pi} \end{aligned} \tag{1.7}$$

Note that for $M_{Z'} \gg m_l$, the branching ratio (BR) to one neutrino species is half of the branching ratio to one charged lepton flavour[15]. The reason is that the Z' only couples to left-handed neutrino chiralities whereas it couples to both left- and right-handed charged leptons. Figure 1.5 shows the value of the branching ratio $BR(Z' \rightarrow ff)$ into the relevant fermions as a function of the Z′ mass.

The model is known to be ultraviolet-safe: this is due to the fact that the coupling with muonic and tauonic currents occurs through their difference, by the term θ in the lagrangian, which avoids triangle anomalies expected when the number of involved families differs from three.

1.3.2 Motivations for the $Z' \rightarrow \mu\mu$ analysis

In this framework, the Z' mediator, beside predicting the correct observed relic abundance, could also explain some experimental observations that can not be explained by the SM. In the following two paragraphs just a couple of them will be briefly described.

Solution to the anomalous magnetic moment of the muon In models dealing with a dark boson candidate in the mass range of $\mathcal{O}$(MeV)−$\mathcal{O}$(GeV), like the Z' , one of the most important constraint on the coupling of the dark sector with the SM derives from the anomalous magnetic moment of the muon, $a_\mu = (g_\mu - 2)/2$. The gyromagnetic moment of the muon g_μ is one of the best known quantities in physics,

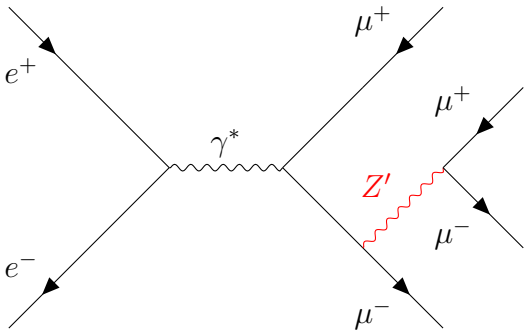

Figure 1.6: Feynman diagram of the process $e^+e^- \to \mu^+\mu^- Z', Z' \to \mu^+\mu^-$.

both experimentally and theoretically, and very sensitive to New Physics through loop corrections. Currently, the experimental results deviates from SM prediction by more than 3σ. The contribution arising from the additional exchange term due to the Z' goes in the right direction to explain the observed deviation [16].

Solution to discrepancy in angular observables in the rare decay $B \to K^*\mu^+\mu^-$ The LHCb collaboration observed a deviation of around 3.7σ from theoretical predictions in angular distributions of the final state particles in the rare decay $B \to K^*\mu^+\mu^-$, which can lead to a viable way to search for New Physics. Therefore, of special interest are the New Physics models that generate the vector coupling to muons. The anomaly-free $L_\mu - L_\tau$ model, which introduces the Z' boson with coupling to only second and third generation of leptons is one of the most promising candidate explanation for the discrepancy observed by the LHCb collaboration [17].

Belle II already searched for an invisible Z' produced in association with a muon pair with the very first data collected in 2018 (corresponding to an integrated luminosity of 0.511 fb^{-1}), in the channel $e^+e^- \to \mu^+\mu^- Z'$, $Z' \to$ invisible [18], where the invisible decay of the Z' can be in neutrinos, $Z' \to \nu\bar{\nu}$, or in light dark matter candidate χ if kinematically accessible.

In this thesis the search of the visible Z'decay in the process $e^+e^- \to \mu^+\mu^-$ Z' , $Z' \to \mu^+\mu^-$, a four-muon final state, is presented. The Feynamn diagram describing this process is shown in Figure 1.6. Figure 1.7 shows instead the cross section of the process $e^+e^- \to \mu^+\mu^- Z', Z' \to \mu^+\mu^-$ for a $g' = 0.01$ as a function of the Z' mass.

The best upper limits on the coupling constant g′ has been set by the *BABAR* experiment through a data set of 514 fb^{-1} [19] (see Figure 1.8). The sensitivity decreasing while increasing Z' mass is mostly due to the cross section fall in the same conditions (see Figure 1.7). The aim of the work presented in this thesis is to improve that result through an aggressive background reduction, in order to discover the particle or to obtain more restrictive limits than *BABAR*, despite the lower Belle II integrated luminosity available now.

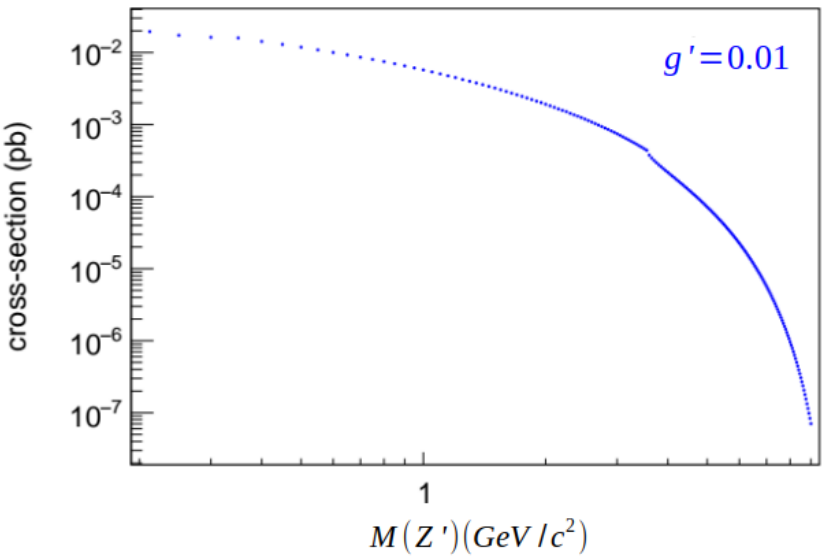

Figure 1.7: Cross section of the process $e^+e^- \to \mu^+\mu^- Z', Z' \to \mu^+\mu^-$ for a fixed $g' = 0.01$, obtained through a **Madgraph** simulation.

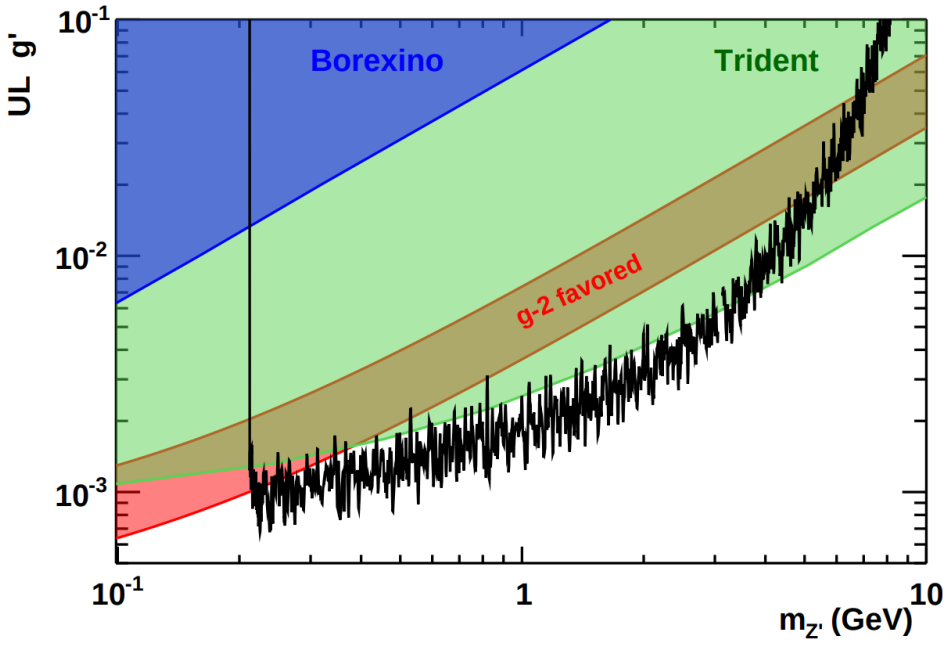

Figure 1.8: 90% CL upper limits on the gauge coupling g′ as a function of the Z′ mass set by the *BABAR* experiment, together with the constraints derived from the neutrino-nucleus scattering processes measured by CCFR [20]. The region consistent with the discrepancy between the calculated and measured anomalous magnetic moment of the muon within 2σ is shaded in red.

Chapter 2

The Belle II experiment

The Belle II experiment at the SuperKEKB e^+e^- collider represents the new generation of B-Factory, the plan of which is to collect an integrated luminosity of 50 ab^{-1} at $\Upsilon(4S)$ resonance, with the goal of refining several measurements in the heavy flavour sector of the SM and searching for New Physics signatures. In this chapter, a detailed description of the SuperKEKB collider and that of the Belle II detector is given.

2.1 SuperKEKB

The new generation of B-Factories is represented by SuperKEKB, the upgraded collider of KEKB, located at the KEK Laboratory in Tsukuba, Japan. The upgrade operations started in 2010. The main motivation for this substantial upgrade is to increase the instantaneous luminosity of the machine from $2.1 \cdot 10^{34}$ $\text{cm}^{-2}\text{s}^{-1}$ (KEKB) to $6.5 \cdot 10^{35}$ $\text{cm}^{-2}\text{s}^{-1}$, to reach the statistic needed for the physics goals of the Belle II experimental program. This luminosity increase is obtained by using a larger beam current and, especially, by a much smaller beam size at the Interaction Point (IP), with the use of the nano-beam scheme, for which is crucial to keep the beam emittance as low as possible [6].

SuperKEKB is an e^+e^- asymmetric circular collider, with an energy of 7 GeV (4 GeV) for the electron (positron) beam. The resulting center-of-mass energy is $\sqrt{s} \approx \sqrt{4E_{e^+}E_{e^-}} = 10.58$ GeV.

The electrons are produced in a pre-injector by a pulsed laser directed on a cold cathode target, then they are accelerated by a linear accelerator (LINAC) to 7 GeV and injected in the High Energy Ring (HER) of SuperKEKB. The positrons are produced by the collision of electrons with a tungsten target and then they are injected in a damping ring to reduce their emittance. When the positrons reach the required emittance they are accelerated to 4 GeV in the LINAC and then injected in the Low Energy Ring (LER).

The two beams collide at the IP with a large crossing angle and with the peculiar nano-beam scheme (described in the following section), one of the major upgrade of SuperKEKB intended to improve the luminosity of the collider. This new colliding scheme required a redesign of the final focus system.

The beam asymmetry produces a Lorentz boost between the frame of the center-of-mass of the colliding leptons and the detector rest frame (i.e. the laboratory frame) equal to $\beta\gamma \approx 0.28$, equivalent to an average flight distance for the B mesons of 130 μm. This distance is sufficient to track the displaced vertex of the B mesons,

but is reduced with respect to KEKB, where $\beta\gamma$ was 0.42. The reason behind is the exponential increase of the power absorption, which sets a limit to the energy of the HER. On the other hand the beam geometry at IP and the bunch shape, that need a strongly reduced dispersion of the bunches, set a lower limit to the LER energy: to obtain the same $\beta\gamma$ of KEKB the energy of the LER should be reduced to 3.5 GeV, but this implies higher beam losses due to Touscheck scattering, that are not sustainable for the luminosity requirement.

The luminosity requirement imposed several other modifications to the accelerator structure: the electron injection and positron target are modified, the damping ring, the radio-frequency system, the optics, the beam pipe and the vacuum system are renewed.

2.1.1 The nano-beam scheme

The nano-beam scheme aims at reducing the beam size at the IP in order to increase the luminosity. The luminosity of a collider is given by:

$$\mathcal{L} = \frac{\gamma_\pm}{2er_e}\left(1+\frac{\sigma_y^*}{\sigma_x^*}\right)\frac{I_\pm \xi_{y\pm}}{\beta_{y\pm}^*}\cdot\frac{R_L}{R_{\xi_y}}\ ,$$

where γ is the relativistic Lorentz factor, e is the absolute value of the electron charge, r_e is the classical radius of the electron, σ_x^* and σ_y^* are the widths of the bunch at the IP on the transvere plane, I is the current of the beam, β_y^* is the vertical betatron function at the IP, ξ_y is the vertical beam-beam parameter, R_L and R_{ξ_y} are the reduction factors of luminosity and the vertical beam-beam parameter due to not-vanishing crossing angle and the $\pm$ sign refers to the charge of the particles in the beam*.

The goal of the nano-beam scheme is to strongly reduce the vertical betatron function with the minimization of the longitudinal size of the beam overlap at the IP (Figure 2.1). The size of the effective overlap region is $d \approx \sigma_y^*/\phi$, where 2ϕ is the crossing angle of the beams. For this reason, the crossing angle has been chosen $2\phi = 83$ mrad (about four times the KEKB crossing angle). In addition σ_y^* is reduced to the size of tens of nm to reach a beam size at the IP of 50 nm (from order of 1 μm of KEKB). In conclusion, with this scheme the betatron function β_y^* is reduced by a factor 20 with respect to KEKB and since $\sigma_y^* \ll \sigma_x^*$, $R_L/R_{\xi_y} \approx 1$ and $\xi_y^{\text{SuperKEKB}} \approx \xi_y^{\text{KEKB}}$, the current of the beams must be doubled to reach the required luminosity.

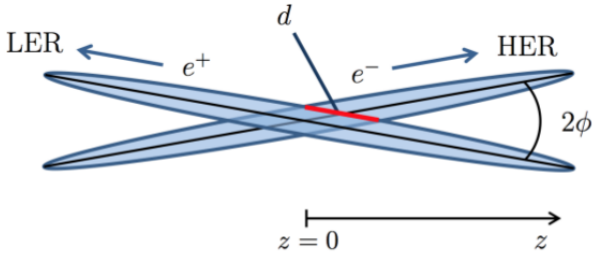

Figure 2.1: The geometry of the IP in the nano-beam scheme. The effective longitudinal overlap size d is highlighted in red.

The main SuperKEKB IP parameters are summarized in Table 2.1.

*It is important to notice that the vertical beam-beam parameter ξ_y is proportional to the ratio $I_\mp/\gamma_\pm$, so the formula for the luminosity given here is not asymmetric if the two signs are swapped.

Table 2.1: SuperKEKB parameters compared to the KEKB parameters.

	KEKB (LER / HER)	SuperKEKB (LER / HER)
E (GeV)	3.5 / 8.0	4.0 / 7.0
2ϕ (mrad)	22	83
ξ_y	0.129 / 0.090	0.090 / 0.088
β_y^* (mm)	5.9 / 5.9	0.27 / 0.41
I (A)	1.64 / 1.19	3.60 / 2.62
σ_x^* (μ m)	1.64 / 1.19	7.75 / 10.2
σ_y^* (nm)	1.64 / 1.19	59 / 59
$\mathcal{L}$ (10^{35} cm^{-2} s^{-1})	0.211	8

2.2 The Belle II detector

Belle II is the detector designed for the SuperKEKB collider, and it is a substantial upgrade of the Belle detector. It is a general purpose experiment, optimized for the reconstruction of $\Upsilon(4S) \to B\bar{B}$ events, with the capability to perform efficient tracking of charged particles, in particular in the low momentum range (down to 50 MeV/c). In addition, a neutral identification system is present, based on precise γ detection, and a multi-detector Particle Identification (PID) system. Anyhow an efficient reconstruction of τ pairs and low multiplicity events is allowed too. Belle II integrates a high efficiency and low bias hardware and software trigger to cope with the high background conditions expected at SuperKEKB. The high-resolution momentum and vertex reconstruction allow precise time-dependent measurements. In addition, the detector hermeticity and the knowledge of the initial state allow to perform missing energy analyses and to use recoil techniques. Because of the low momentum range studied by the experiment a crucial feature of the detector is the material budget, kept as low as possible.

A comprehensive description of the Belle II detector can be found in [21] and [22].

2.2.1 Detector overview

The detector has an approximate cylindrical symmetry around the z-axis (set along the bisector of the angle between the direction of the electron beam and the reverse direction of the positron beam), while it has a significant forward-backward asymmetry to improve the solid angle acceptance in the boost (forward) direction. The general structure of the detector is shown in Figure 2.2.

From the innermost to the outermost sub-detector system Belle II is composed of:

- Pixel Detector (PXD): 2 layers of pixel sensors (DEPleted Field Effect Transistor technology);
- Silicon Vertex Detector (SVD): 4 layers of Double-Sided Silicon Strip sensors; the PXD and the SVD form the Vertex Detector (VXD);
- Central Drift Chamber (CDC): helium-ethane wire drift chamber, composed of 56 layers with stereo and longitudinal geometry;

- Particle Identification System (PID): a Time-Of-Propagation (TOP) counter with a quartz radiator for the barrel region with a Cherenkov quartz radiator, and an Aerogel Ring-Imaging Cherenkov (ARICH) detector, with an areogel radiator for the forward endcap region;
- Electromagnetic Calorimeter (ECL): an homogeneous calorimeter composed of more than 8000 CsI(T) crystals that provide 16.1 radiation lengths X_0;
- Superconducting magnet: a NbTi/Cu magnet that provides a homogeneous magnetic field of 1.5 T parallel to the beam direction in the internal region;
- K_L and Muon Detector (KLM): alternated layers of Resistive Plate Chambers (RPCs) and iron plates in the outermost barrel region and scintillator strips in the innermost barrel region and in both endcaps; it provides about 4 interaction lengths, in order to detect the particles that escape from the internal region; the iron structure of the KLM detector is used as return yoke of the magnetic field.

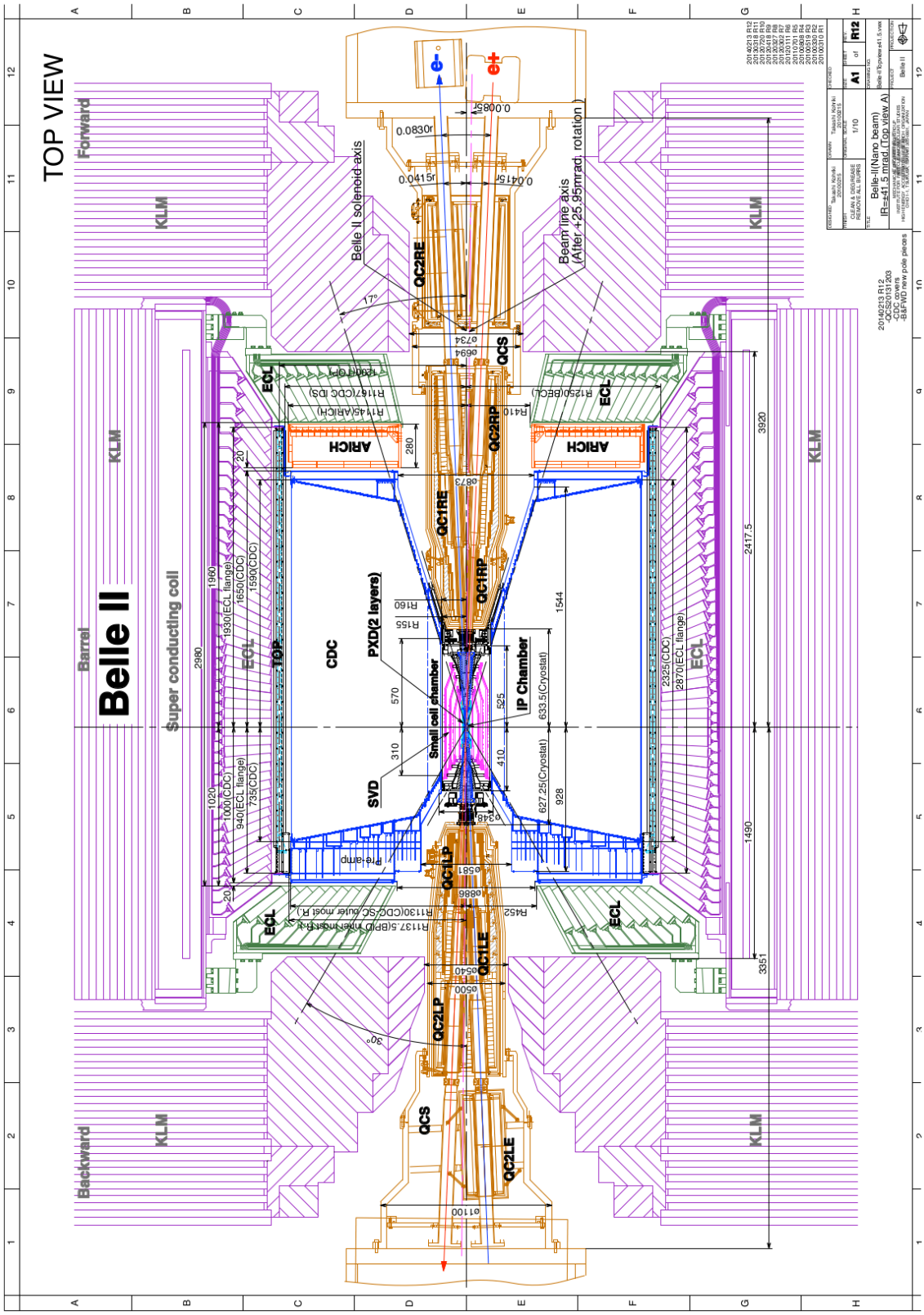

Figure 2.2: Top view of Belle II, with all the subdetctors highlighetd, and the IP region.

2.3 Vertex Detector (VXD)

The VXD is the innermost sub-detector of Belle II. It is composed of two devices, the Pixel Detector (PXD) and the Silicon Vertex Detector (SVD), forming a 6-layer silicon vertex detector. It is a completely new device with respect to the Belle SVD. The PXD and SVD schemes are shown in Figure 2.3.

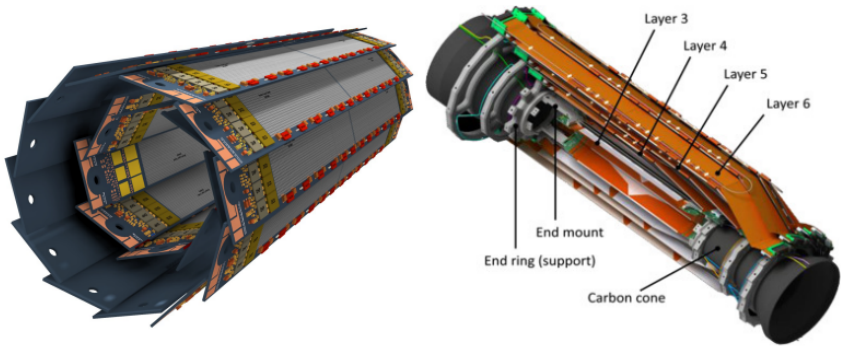

Figure 2.3: Schematic view of the PXD (left) and SVD (right) detectors.

The PXD is composed of two layers of pixelated sensors with DEPFET (DEPleted Field Effect Transistor) technology, to obtain a low material budget of $0.2X_0$ per layer in the detection region. The layers are placed at 14 mm and 22 mm from the IP, while the beam pipe radius is about 10 mm. The pixelated sensors have been chosen to sustain the higher hit rate due to the shorter distance from the IP and the higher luminosity with respect to Belle. This solution allows keeping the occupancy of the detector at about 3% (where the occupancy is defined as the number of activated channels at the same time over the total number of channels). The amount of data provided by the PXD in a single event is nonetheless higher than the accepted Data Acquisition (DAQ) rate, therefore the charged tracks are reconstructed online using the SVD and CDC information and then extrapolated onto the PXD sensors during the High Level Trigger process. This extrapolation determines some Regions Of Interest (ROI) from which the PXD hits are selected for readout, allowing the system to remain within the DAQ bandwidth.

The SVD is composed of four layers of Double-Sided Silicon Strip Detector, placed at 38 mm, 80 mm, 115 mm, and 140 mm from IP. SVD uses several types of sensors, each with different shapes and strip pitch. An original feature of the SVD is the Origami chip-on-sensor concept, an innovative solution that uses a flexible fan-out to put all the readout chips on the same side of the modules in the detection region to reduce the connections and simplify the cooling system.

2.4 Central Drift Chamber (CDC)

The CDC is a wire drift chamber with three main functions in Belle II: first it is the main tracking device to precisely measure momenta, second it provides PID information by measuring the energy losses in the gas volume, third it is used in hardware and software trigger.

The chamber is composed of 8 superlayers formed by 6 layers of wires each, and an innermost superlayer formed by 8 layers of wires. The chamber is filled with a mixture of helium and ethane (50% He, 50% C_2H_6), and the entire CDC is closed by

two carbon cylinder and 2 aluminium endplates. Two classes of wires are present: the field wires producing the accelerating electric field, and the sense wires collecting the released charge. The field wires are composed of aluminium and are thicker (126 μm of diameter) than the sense wires, which are made of gold-plated tungsten and have a diameter of 30 μm. The radial cell size is 10 mm for the innermost superlayer and 18.2 mm for the other superlayers. When a charged particle crosses the CDC ionize the gas mixture of the chamber producing electrons. The electrons are accelerated by the electric field and produce a charge avalanche that induces a signal on the sense wires, from which is possible to reconstruct the drift time and thus the initial particle position.

The front-end electronics is located near the backward endplate, and it uses an ASIC chip to amplify, shape and discriminate the signal. A TDC is used to measure the drift time and a FADC to measure the signal charge.

To obtain the z position information from the CDC, half of the superlayers have a stereo wire configuration. It means that the wires are not strictly parallel to the z-axis, but present a small angle on the r-ϕ plane. With the use of different inclinations it is possible to reconstruct the 3D position. There are 3 classes of classes of superlayer, one axial ("A") and two stereo ("U", "V"). The configuration of the 9 superlayers is "AUAVAUAVA", chosen to optimize the trigger z resolution.

The innermost radius of CDC is 160 mm, larger than the Belle one (77 mm), because the higher expected background rates would make the chamber unusable at smaller radius. A complex endplate geometry is employed to ensure good angular coverage while limiting occupancy, especially from Bhabha scattering in the forward direction. The outermost radius is 1130 mm, larger than the Belle one (880 mm) because the PID barrel device of Belle II is more compact than in Belle. The angular acceptance is the same of VXD ($\theta \in [17°, 150°]$) to be able to merge all the tracks of two sub-detectors. The position resolution of CDC is about 100 μm, while the dE/dx resolution is about 12% for particles with $\theta \approx \frac{\pi}{2}$.

2.5 Particle Identification (PID)

The main devices for PID in Belle II located outside the CDC are the TOP in the barrel region and the ARICH in the forward endcap region. Both systems detect Cherenkov light, but the operating principles are substantially different, thus they are described separately. The idea of Cherenkov detectors is to measure the θ_C angle of photons emitted by relativistic charged particles crossing a radiator material, obtaining β of the particle with the relation $\cos\theta_C = 1/n\beta$, where n is the refractive index of the material. In Belle II, using the independent momentum measurement in the tracking system and the measurement of β combined to the energy loss measured in the CDC the mass of the particles is determined. A PID likelihood is defined with the use of the measured momentum of the track, and various charged particle hypotheses are tested with a "PID selector" that compares the likelihood ratio between various mass hypothesis. The tested particles are pions, kaons, electrons, muons, protons and deuterons.

2.5.1 Time-Of-Propagation counter (TOP)

The structure of the TOP is shown in Figure 2.4: a single TOP module is made of a quartz bar with a focusing mirror in the forward region and an array of photomultipliers

(PMT) in the backward region.

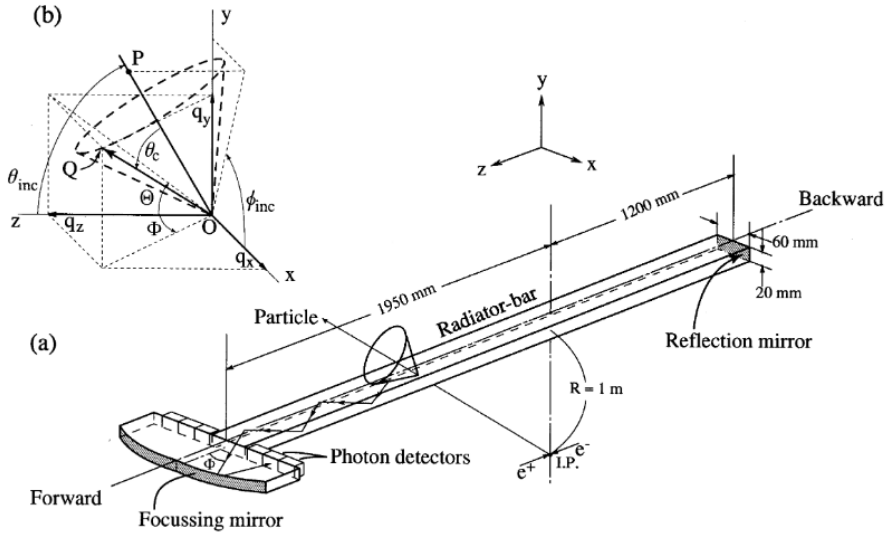

Figure 2.4: Scheme of a single module of the TOP detector. Note that the values in the figure refer to a prototype version of a TOP module and slightly differ to the actual ones.

The operating principle of the TOP detector is to obtain θ_C from the measurement of the time of arrival of the Cherenkov photons from the emission point as a function of the angle of the Cherenkov cone Φ on the plane of the bar. From the combined information of the arrival time t_{TOP}, Φ and position and direction of the main particle provided by tracking, it is possible to extract the θ_C information. The complete discussion is omitted here, for details see [4].

In the TOP detector the emitted photons are reflected internally in the quartz bar and reach the focusing mirror in the forward region. The mirror is built to conserve the Φ angle information and to reflect the photons to a specific PMT channel that measure the t_{TOP}. Thus the Φ angle is evaluated depending on the PMT activated channel. The photons emitted in the backward directions are first reflected by a mirror at the end of the quartz bar and directed to the focusing mirror.

The entire TOP detector is made of 16 modules set around the CDC at 1.2 meter of radius from IP, with an angular acceptance of $\theta \in [31°, 128°]$. The bar quartz dimension is 0.45 m $\times$ 2 cm $\times$ 2.75 m. The TOP has a single photon time resolution of about 100 ps, achieved with 16 channel micro-channel plate PMTs. Instead the production time of the main particle is known with the precision of about 50 ps.

2.5.2 Aerogel Ring-Imaging Cherenkov detector (ARICH)

The ARICH is a proximity focusing Ring-Imaging detector, which uses as radiator two layers of aerogel. An expansion volume of 20 cm divides the radiator from a ring of hybrid avalanche photon detector (HAPD), and allows the Cherenkov photons to enlarge into rings.

The performance of RICH detectors depends on the number of detected photons N_γ and the single photon resolution on the Cherenkov angle σ_{θ_C}. N_γ increases with the thickness of the radiator and the resolution per track improves as $\sigma_{\theta_C}/\sqrt{N_\gamma}$, but σ_{θ_C} degrades due to the uncertainty of the emission point. In the Belle II ARICH a peculiar solution is adopted to optimize the performance: two layers of aerogel with

different refractive indexes ($n = 1.045$ upstream and $n = 1.055$ downstream) and 2 cm thickness are used, so that the two produced rings are overlapped on the detection surface, giving the N_γ equivalent to a double radiator thickness.

The reached resolution is $\sigma_{\theta_C} \approx 13$ mrad, optimized for charged tracks with momentum larger than 3.5 GeV/c, but the σ_{θ_C} doesn't show significant degradation also for lower momentum tracks. With $N_\gamma \approx 10$ per ring, the resolution of a single track is about $\sigma_{\theta_C} \approx 3$ mrad. The angular acceptance is $\theta \in [14°, 30°]$.

2.6 Electromagnetic Calorimeter (ECL)

The ECL has several central roles in Belle II. First, it detects photons with high efficiency and measures their energy and angle. Secondly, it identifies electrons and contributes to the K_L detection with the KLM sub-detector. Third, it generates a hardware and software photon trigger. In addition, the ECL is used to monitor online and offline the luminosity of SuperKEKB.

The Belle II ECL uses the same crystals of Belle's calorimeter, but a complete upgrade of the readout electronics was needed to cope with the SuperKEKB increased luminosity. The calorimeter is subdivided into three regions, the barrel region, the forward and the backward region, and they collectively cover 90% of the solid angle in the center-of-mass system (with an angular acceptance of $\theta = [12.4°, 155.1°]$). The barrel region is extended for 3 meters and has an inner radius of 1.25 m. The annular endcap regions have the internal base at z = 1.96 m (forward) and z = -1.02 m (backward) from IP. There are two gaps of 1° between the barrel and the endcaps regions to allow the passage of the cables of internal sub-detectors.

The ECL is a homogeneous highly segmented calorimeter, composed by 8736 crystals of CSI(Tl) (caesium iodide thallium-doped). The crystals have a shape of a truncated pyramid with a length of 30 cm and a 6×6 cm^2 base, equivalent to 16.1 X_0. The crystals are assembled in 8 cells separated by 0.5 mm thick aluminium septum walls and closed by two cylinders. Each cell provides the optimal operating environment for the crystals in term of humidity and temperature by a dry air flushing and a water cooling system.

At the external bases of the crystals 10×20 mm^2 photodiodes are glued with a 1-mm plexiglass plate collecting light from the scintillating material. Each photodiode has a LED to inject light pulses into the crystal volume to monitor the optical stability. The relatively long decay time of scintillations in CsI(T) (1 μs), in the in presence of elevated background level expected in Belle II, produces a not negligible overlapping of pulses from neighbouring background events. Therefore the new readout electronics samples the photodiodes' signals in 16 points and then fits the signal shape with a predefined proper function.

The energy resolution of ECL, from a prototype test, is given by:

$$\frac{\sigma_E}{E} = \sqrt{\left(\frac{0.066\%}{E}\right)^2 + \left(\frac{0.81\%}{\sqrt[4]{E}}\right)^2 + (1.34\%)^2}\ ,$$

where E is the energy in GeV For instance it means $\sigma_E/E \approx 2\%$ at 100 MeV and $\sigma_E/E \approx 1.4\%$ at 4 GeV. In Belle the angular resolution of ECL is $\sigma_\theta \approx 13$ mrad at low energy and $\sigma_\theta \approx 3$ mrad at high energies, while the π^0 mass resolution is 4.5 MeV/c^2. Despite the higher background level, because of the new electronics, the performance are expected to be similar in Belle II.

2.7 Superconducting magnet

A superconducting coil produces a 1.5 T homogeneous magnetic field B parallel to the beam direction. The coil is made of NbTi/Cu, and the internal volume is a cylinder of a diameter of 3.4 m and a length of 4.4 m. It operates with a 4400 A current and a liquid helium cryogenic system. The iron structure of the KLM provides the return yoke of the magnetic field, therefore in the region of KLM outside the coil the direction of B (i.e. the curvature of the tracks) is inverted.

The magnetic field has been mapped with commercial Hall sensors with a precision of 0.1%. The inhomogeneities of the field are due mainly to edge effects and to the presence of final focus system magnets of SuperKEKB.

2.8 K_L and Muon Detector (KLM)

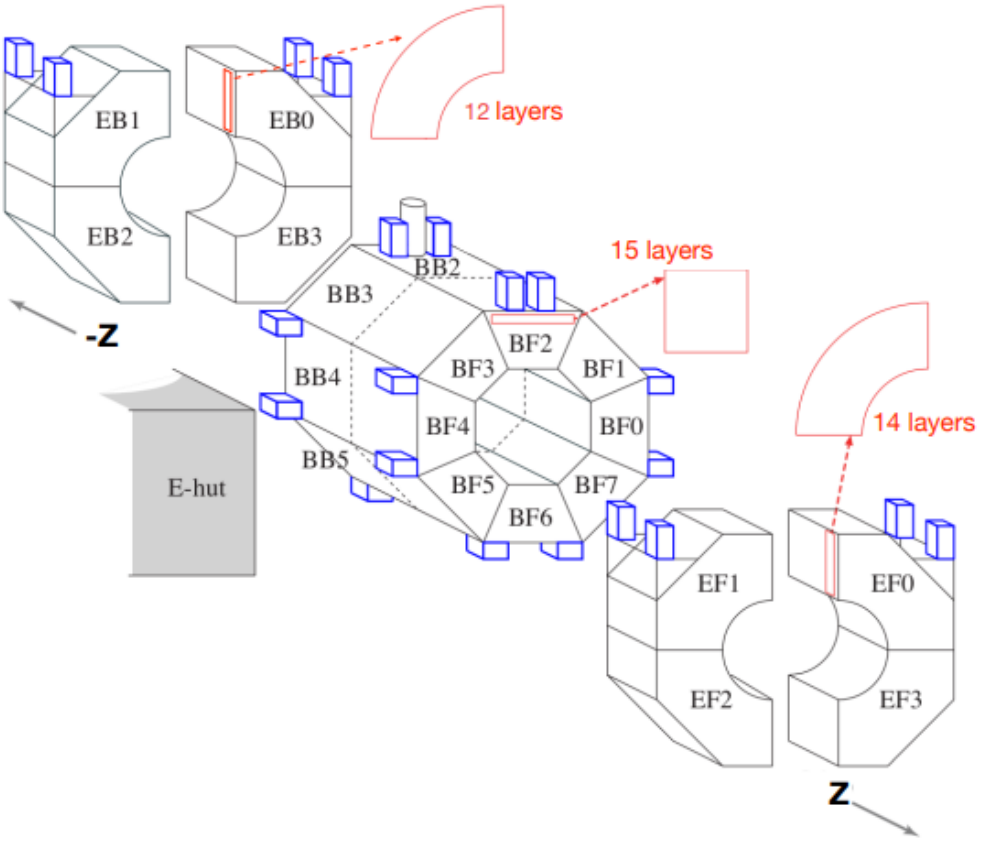

Figure 2.5: KLM scheme.

A schematic view of the KLM is shown in Figure 2.5. The KLM is located outside the superconducting coil, and it is composed of alternating iron plates and active material detectors. The barrel region covers the polar angle range from $\theta = 45°$ to $\theta = 125°$, and the endcaps extend the range from $\theta = 20°$ to $\theta = 155°$. In the barrel region there are 15 detector layers and iron plates, while in the forward endcap are present 14 detector layers and iron plates and in the backward endcap there are 12 detector layers and iron plates.

The iron plates are 4.7 cm thick each and serve as the magnetic flux return for the superconducting solenoid and providing 3.9 interaction lengths λ_0 in addition to the $0.8\lambda_0$ of the ECL, in which K_L can shower hadronically.

The task of the KLM detector is to identify the muon tracks by measuring their penetration depth in the iron and to reconstruct neutral long-lived kaons with the use of the combined information of ECL and the hadronic KLM showers.

The outermost barrel detector layers of KLM are Resistive Plate Chambers (RPC): a proportional gas chamber used in streamer mode with a dielectric plate between the electrodes to prevent the propagation of sparks and so increase the spatial resolution. The signal is read by metallic strips on one side of the chamber. Each KLM module is made of two coupled RPC, with independent power supply and orthogonal strips configuration.

Because the RPCs have a too long dead time to sustain the background rate expected is some regions of the detector, in the endcaps region and in the two innermost barrel layers of the KLM, the RPCs have been substituted with two orthogonal layers of scintillator strips coupled with silicon photomultiplier (SiPM).

The K_L detection efficiency rises linearly from 0 at 0 GeV/c to a 80% plateau at 3 GeV/c. The angular resolution is about 3° for KLM-only candidates. The scintillator strips coupled to the SiPMs offer an excellent time resolution of $\sigma_t \approx 0.7$ ns, that allows to measure also the time of flight of K_L.

2.8.1 Muon identification

The total Particle Identification (PID) is based on detector quantities coming from the Belle II sub-detectors. The algorithms are implemented in different ways and their outcomes are quantified in log-Likelihood values assigned to six particle hypotheses independently: e, μ, π, K, P, d (deuteron). These values are combined together as a sum, in order to have a unique likelihood per particle. The combination of the log-likelihoods is performed considering the same weights for each sub-detector. Assuming we need to determine the likelihood for a muon (μ):

$$log\mathcal{L}_\mu = log\mathcal{L}_\mu^{SVD} + log\mathcal{L}_x^{CDC} + log\mathcal{L}_\mu^{TOP} + log\mathcal{L}_\mu^{ARICH} + log\mathcal{L}_\mu^{ECL} + log\mathcal{L}_\mu^{KLM}. \quad (2.1)$$

The final PID variable used in physics analyses is then normalised to every particle hypothesis:

$$\mu ID \;=\; \frac{\mathcal{L}_\mu}{\mathcal{L}_e + \mathcal{L}_\mu + \mathcal{L}_\pi + \mathcal{L}_K + \mathcal{L}_p + \mathcal{L}_d}. \quad (2.2)$$

The muon identification (μID) rely mostly on ECL, TOP and KLM detectors information. The ECL provides the separation between muons and electrons, protons and deuterons via the calorimetric energy deposition. Since they are mostly produced in *BelleII* as Minimum Ionizing Particles, muons loose a smaller amount of energy in the ECL crystals. Fake rates from kaons are handled mainly by the TOP detector, exploiting information by the Time of Flight and the time propagation of the Cherenkov light. Pions behave very similarly to muons and the only powerful way to discriminate between the two is to rely on the KLM.

Muon identification in the KLM

The working principle of the algorithm used to compute the μID exploiting the KLM information is based on two major steps: **track extrapolation** process towards the KLM and **likelihood extraction** for each particle hypothesis: electron, muon, pion, kaon, proton and deuteron.

Track extrapolation. The track extrapolation is provided by Geant4 toolkit [23]. The extrapolation towards KLM of the tracks reconstructed by the tracking detectors, always assumes the muon hypothesis and starts at the outermost CDC layer that detected a hit. The extrapolation makes use of a Kalman-filter algorithm that exploits the presence of matching 2D hits in the KLM layers to adjust the trajectory by changing the parameters and the covariance matrix of the tracks. A 2D hit is considered matched when it is less than 3.5σ away from the extrapolated position, where σ is the sum in quadrature of the hit detection uncertainty and the extrapolation related error.

Likelihood determination. The likelihood value assigned to the tracks is the product of two terms: one based on the differences in the penetration depth (**longitudinal probability**, P_n^l) and the other based on the transverse shower dimension in the KLM (**transverse probability**, P_n^t). Both, the longitudinal and the transverse probabilities are computed assigning a probability to each KLM layer, also keeping into account the layer efficiency ε_n.

As a last step, for each track, the algorithm provides likelihoods $\mathcal{L}$ for all the particle hypotheses, as the product of the longitudinal and transverse probability values. The final μID variable based on KLM is evaluated using the Equation 2.2

2.9 Trigger

The bunch crossing frequency of SuperKEKB is about 250 MHz[†]. Since the bunch crossing time is much faster than the detectors signal decay time for all practical purposes the beam can be considered continuous. Anyway, at full luminosity, the expected event rate is about 50 kHz, and over than 90% of these events are Bhabha scattering or $e^+e^- \to \gamma\gamma$.

A trigger system is therefore required to select events from beam background and identify interesting ones. Despite $B\bar{B}$ events are characterized by a higher charged track multiplicity with respect to others events, this variable can not be used in the trigger because τ and low multiplicity events would be discarded too. The required trigger must have instead an efficiency of about 100% for $B\bar{B}$ events and a high efficiency for τ and low multiplicity events too. Some efficiency degradations are allowed to suppress the Bhabha and $\gamma\gamma$ events. The trigger rate must stay below 30 kHz, the maximum acquisition frequency of DAQ, and the trigger must provide time information with a precision under 10 ns to exploit the potential of the Belle II subdetectors. To cope with the high background and to the several physics scenarios the trigger system must be robust and flexible.

[†]The SuperKEKB radio-frequency is about 500 MHz, but currently one every two bunch is not filled, resulting in an effective bunch crossing time of 4 ns

The Belle II trigger is subdivided in two main stages: a hardware or Level 1 trigger (L1) and a software or High Level Trigger (HLT). The first one removes most of the background events with the use of raw information from the faster sub-detectors, the second trigger refines the selection with a more exhaustive analysis.

2.9.1 Level 1 trigger (L1)

The L1 trigger scans signals from detectors with a FPGA structure that provides a configurable system (programmable devices). The L1 trigger uses various signals from sub-detectors at low resolution and implements multiple trigger lines. The main sub-detectors that contribute to L1 trigger are CDC and ECL, although TOP and KLM are also used. A Global Reconstruction Logic combines the information of various sub-detector to obtain the total trigger logic.

The CDC provides two-dimensional and three-dimensional tracking information. The z-position of the main vertex of the events is a strong discriminant for background events (with vertices far away from the IP). The FPGA takes about 1 μs to reconstruct the z position of the vertex. The ECL provides a trigger signals mainly based on the total energy released in the calorimeter and on the number of the isolated showers that use the 3D clustering techniques. With this methods the L1 trigger is able to reject most of Bahbha and $\gamma\gamma$ backgrounds without a significant degradation of the efficiency for low multiplicity events. The L1 trigger is also able to identify Bhabha and $\gamma\gamma$ events to monitor online the luminosity of SuperKEKB.

The latency of the trigger is about 5 μs and the maximum trigger rate is 30 kHz as required, with an efficiency over 99.9% for $B\bar{B}$ and continuum events.

2.9.2 High Level Trigger (HLT)

The goal of the HLT is to reduce the 30 kHz event rate from the L1 trigger to a maximum storable rate of 10 kHz.

The HLT uses the full information of all sub-detectors except the PXD and performs a fast reconstruction: the events are completely reconstructed with the same software used in the offline analysis (except the PXD information). Then the trigger applies physics requirement to the reconstructed events and reduces to 10 kHz the event rate. It is important to note that during the Phase 2 run, the HLT was not turned on and no data reduction was thus applied.

After the HLT reduction, the tracks reconstructed with the SVD and the CDC in the fast reconstruction are extrapolated to the PXD layers and the ROI are evaluated, then the pixels inside the defined regions are read. In conclusion, the full events are build combining the fast reconstruction events with the PXD data before the definitive storage. Before the fast reconstruction and the ROI extrapolation, the full PXD data are stored inside a pipeline, which receives in input the PXD data from the events selected by L1 trigger. The length of this pipeline defines the latency constraint of HLT. The current latency of the HLT is some seconds, under the pipeline constraints.

Chapter 3

$Z' \to \mu\mu$ analysis

In this chapter the detailed procedures used for the $Z' \to \mu^+\mu^-$ search will be described. The first sections will introduce the adopted strategy and the tools used to implement it in practice. The goal is to obtain more restrictive upper limits on the coupling constant g′ than *BABAR* and Belle, using much less luminosity. In order to achieve this a different approach has been applied, which consists of an aggressive background suppression.

The event selection is described in section 3.3 and is the central part of this thesis. In particular, the construction of discriminating variables and their usage in a neural network MLP selection (see subsection 3.3.5) represents a major difference between the approach used in this work and the previous searches.

An other important step of this analysis is represented by the ee$\mu\mu$ control sample studies. The ee$\mu\mu$ sample has been used to check all the analysis performances, in particular the MLP and the trigger efficiencies, and to evaluate the systematic uncertainties affecting this search. An extensive work was done, mainly using the control sample, to get rid of some issues present in the MC simulation, that potentially spoil the data-MC agreement and the analysis success (see, for example, subsection 3.3.3). All the details about control sample studies are in section 3.5.

In section 3.4 the evaluation of the trigger efficiency is shown.

The signal modeling and the fit procedure are described in sections 3.7 and 3.8.

Systematic uncertainties are discussed in section 3.9.

I directly worked on the full analysis method, on the event selections, on the ee$\mu\mu$ control sample studies, on the trigger efficiency evaluation and on the estimate of the systematic uncertainties. A Belle II colleague took care of the signal modeling and the fit procedure parts, of which I only made use.

As anticipated, the analysis did not get the collaboration approval yet. A 10% data unveiling has been requested with respect to the target luminosity on which the analysis is based (54 fb^{-1}), with the only goal to show results in this thesis and nowhere else. Finally, the permission to look at 5.4 fb^{-1} was granted, and results are shown in chapter 4.

3.1 Software and data sample

Signal samples have been generated using **MadGraph@5-NLO** [24] with the model **Lmu_minus_Ltau_UFO.release-04-00-03** has been for generation and **release-05-01-12** for reconstruction purposes. For the analysis **root v6-21** with **TMVA**,

Table 3.1: MC13a samples used for background studies with the equivalent integrated luminosity $\int$Ldt

Process	$\int Ldt$ [fb^{-1}]	MC generator
$e^+e^- \to \mu^+\mu^-\mu^+\mu^-$	5000	AAFH [27]
$e^+e^- \to \mu^+\mu^-(\gamma)$	200	KKMC [28]
$e^+e^- \to \tau^+\tau^-$	200	TAUOLA [29]
$e^+e^- \to e^+e^-\mu^+\mu^-$	200	AAFH [27]
$e^+e^- \to u\bar{u}$	200	KKMC [30]+PYTHIA+EvtGen
$e^+e^- \to d\bar{d}$	200	KKMC [30]+PYTHIA+EvtGen
$e^+e^- \to c\bar{c}$	200	KKMC [30]+PYTHIA+EvtGen
$e^+e^- \to s\bar{s}$	200	KKMC [30]+PYTHIA+EvtGen
$e^+e^- \to B^0\bar{B}^0$	200	EvtGen
$e^+e^- \to B^+B^-$	200	EvtGen
$e^+e^- \to \pi^+\pi^-(\gamma)$	60	PHOKARA [30]

RooFit [25] and **RooStats** packages have been employed. For MC background samples has been used the official run independent **MC13a** samples. In Table 3.1 all information about background MC samples used and their luminosities are given.

Signal simulation. 20000 signal events for different Z' masses at steps of 25 MeV/c^2 from 0.25 GeV/c^2 to 10 GeV/c^2 have been produced, with a fixed width of 10^{-6} GeV/c^2 (well below the detector resolution) and a coupling constant g$'$ = 1, using the MadGraph5 generator, which provides the framework for simulating SM and Beyond the Standard Model (BSM) processes and computing their cross section [26]. This generator includes, through an external plugin, Initial State Radiation (ISR) effects, with the exception of the radiation of hard photons at large angles, typically in acceptance.

Background samples. The official run independent **MC13a** samples were used. In particular:

- For preliminary background and discriminant variables studies were used 5000 fb^{-1} of $\mu^+\mu^-\mu^+\mu^-$ events;
- For the neural network MLP training and test were used 5000 fb^{-1} of $\mu^+\mu^-\mu^+\mu^-$ events and 100 fb^{-1} of $\mu^+\mu^-(\gamma)$ events, in the fraction of 50% for training and 50% for test;
- For data-MC comparison the $e^+e^-\mu^+\mu^-$ control sample was used, the integrated luminosities and the generator used are shown in Table 3.1.

Data The targeted integrated luminosity is $\int$Ldt$\sim$ 54 fb^{-1} of data collected during the 2020a and 2020b runs. The luminosity collected during the run 2020c is not included in this study due to a technical problem (it would require a different version of the reconstruction software).

- For the $ee\mu\mu$ control sample have been used $\int$Ldt $\sim$ 54 fb^{-1} bucket9, 10, 11, 13, 14 and 15 collected on Υ(4S) resonance;
- For trigger studies (see section 3.4):
  - buckets from 9 to 15 (54 fb^{-1}) were used for CDC fff* trigger case;
  - buckets from 10 to 15 (51 fb^{-1}) were used for CDCKLM† and CDCKLM OR fff trigger case, since CDCKLM trigger was not available in bucket9.

3.2 Analysis strategy

The studied process is the $e^+e^- \to \mu^+\mu^- Z', Z' \to \mu^+\mu^-$ decay. The signal signature is the presence of a peak in the dimuon mass distribution in events with four muons having an invariant mass compatible with $\sqrt{s}$ and nothing else in the final state. The existence of Initial State Radiation (ISR) partially spoils this picture, allowing the presence of radiated photons and moving the four-muon invariant mass away from the collision energy. The first selection consists in requiring events with exactly four tracks, where at least three are identified as muons. It is also required that the total four-track invariant mass, M(4-tracks), is restricted between 10 and 11 GeV/c^2.

For this search, two trigger lines in logical OR are used: the CDC trigger line fff and the OR of the CDCKLM lines. Data events with the corresponding bits set are selected and the measured efficiencies are used as MC event weights, to properly scale the simulation, while comparing data with MC. The trigger simulation is not employed at all, as this is proved to be unreliable for these lines, at least in the present release (MC13).

A selection is applied in order to remove events with photons, as they are not expected to be present in signal events at first order. This is a very important feature of the analysis, as the ISR contribution (see subsection 3.3.3) is simulated in the signal, but not in some of the most important background sources (SM four lepton processes).

The main expected background component is the Standard Model $\mu\mu\mu\mu$ final state. One of the main parts of the analysis is devoted to the background suppression. Distributions of kinematic variables for both background and signal events are studied, and their differences exploited. A Multivariate Analysis (MVA) technique is implemented to reject as much background as possible, while keeping an acceptable signal efficiency. This is a very important difference with respect to the searches performed by *BABAR* and Belle experiments, which did not use any background suppression.

A kinematical fit procedure is applied to events that pass all the selections, imposing the 4-track invariant mass to coincide, within the experimental resolution, with the collision energy $\sqrt{s}$. This is done solely to improve the dimuon mass resolution.

The signal yield extraction is performed through a fit of the dimuon mass distribution. The same fit procedure allows an estimate of the background directly from data. For this reason, I do not have the need to rely on absolute background predictions: this is of great help, as the lack of the ISR contributions in the main background process would make such a prediction extremely unreliable.

*The CDC fff trigger requires the presence of at least 3 tracks with polar angles approximately in the barrel

†The CDCKLM trigger requires n CDC tracks matched with barrel KLM clusters, with 8 layers fired as minimum

The ee$\mu\mu$ control sample is used to check the analysis procedure, the effectiveness of the background suppression and for data/MC comparisons, from which the most important systematic uncertainties are estimated.

3.3 Event selection

3.3.1 Signal and background definitions

Events selected are required to be with exactly four tracks coming from the interaction region, with impact parameters with respect to the collision point in the longitudinal and transverse direction within $|dr| < 0.5$ cm and $|dz| < 2$ cm, respectively. The sum of the four charges is required to be zero.
For each event, there are four possible pairs of oppositely charged tracks. At this level of the analysis, there is no a priori attempt to distinguish one of these pairs as more likely coming from a Z' decay. Each event will therefore contribute with four possible 4-tracks different candidates, each with a different candidate Z' invariant mass, causing unavoidably some combinatorial background. In fact, in all the distributions in the plots presented at this level of the selection, we found four entries per event, corresponding to the four possible candidate $\mu^+\mu^-$ pair.
A 4-tracks candidate has a pair of tracks, named "candidate tracks" that, in case of signal, are the decay products of the Z' , and two more tracks, named "recoil tracks". Signal is defined as the only 4-tracks candidate (out of four) with both candidate tracks coming from the Z' decay: this condition is checked by requiring that the PDG code of the candidate track pair mother is 26, the code of the Z' . The candidate mass is the invariant mass of the candidate track pair: it coincides with the Z' mass, within the experimental resolution, in case of proper signal. "Candidate" tracks and "recoil" tracks exist for background too, but in this case none of them comes from a Z' decay.

At least three tracks are required to be identified as muons (see subsection 3.3.2): two cases have been taken into consideration, with μID > 0.5 and μID > 0.9. The choice of requiring three muons is the result of an optimization and marks a difference with respect to the selections used by *BABAR* and Belle, because they both required the presence of two identified same-charge muons. The total four-track invariant mass, M(4-track), is restricted between 10 and 11 GeV/c^2.

Characterization of background events

The requirement on the 4-track invariant mass has deep effects on the background, suppressing the processes that have important missing energy signatures. The main background processes contributing to the analysis final state are: $e^+e^- \to \mu^+\mu^-\mu^+\mu^-$, $e^+e^- \to \mu^+\mu^-(\gamma)$, $e^+e^- \to \tau\tau$, $e^+e^- \to q\bar{q}$ $(q = u, d, s, c)$, $e^+e^- \to \pi^+\pi^- J/\psi(J/\psi \to \mu^+\mu^-)$. The $e^+e^- \to b\bar{b}$ process turns out to be negligible, due to its high charged track multiplicity. There is no generator in Belle II for the $e^+e^- \to \pi^+\pi^- J/\psi(J/\psi \to \mu^+\mu^-)$ process, which is expected to contribute, according to the *BABAR* experience, at $\sim$1% level. Other processes with Υ resonances, $e^+e^- \to \pi^+\pi^-\Upsilon(\Upsilon \to \mu^+\mu^-)$ are found to be negligible. Processes with light hadron resonances (ρ, ω, ...) are also expected to contribute for low dimuon masses, mainly through mis-identification of pions in muons. They are not included in the used generators.

The largely dominant background is the SM four muons final state, followed by the $e^+e^- \to \mu^+\mu^-(\gamma)$ for the low Z' masses only. The $e^+e^- \to \mu^+\mu^-\mu^+\mu^-$ process proceeds mainly with the two diagrams represented in Figure 3.1. They are actually the same diagram, where one is the 90° rotation of the other, but nevertheless identify very different regimes:

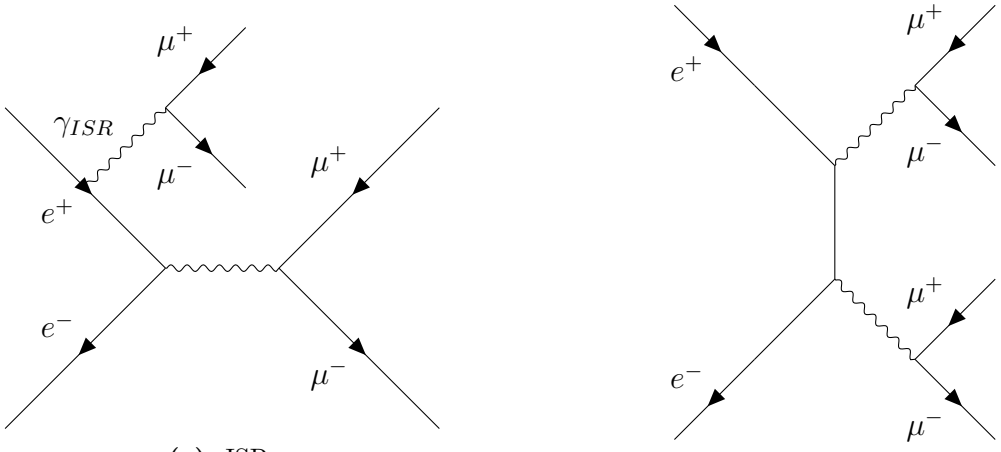

(a) ISR.

(b) Double photon conversion.

Figure 3.1: Feynman diagrams of the two main contributions to the four muon SM background.

- **ISR**, produces a muon pair through the conversion of an offshell ISR photon. Due to this feature, it typically gives rise to low mass muon pairs in the forward direction recoiling against a high mass muon pair, and is suppressed by the requirement that tracks have to be within the CDC acceptance;
- **Double-photon conversion**, is the dominant background, with the exception of the low mass region.

The dimuon mass spectrum expected for the $\mu\mu\mu\mu$ process is shown in Figure 3.2. The different contributions from the ISR diagram in the low mass region and from the double conversion diagram above 1 GeV/c^2 are clearly discernible.

The double-photon conversion diagram typically gives rise to two muon pairs from offshell photons. For a specific Z' mass hypothesis (scanning technique), one of the two pairs will be constrained to be on the mass of the searched for Z' candidate M(Z') while the other pair will be preferentially emitted at the lowest possible value, $2m_\mu$. This feature identifies a *quasi-two body* process with a particle of mass M(Z') recoiling against a *"zero"* (actually $2m_\mu$) mass object. In the center-of-mass (CMS) system, the kinematics of such a process is closed, with a momentum P_0 of the two quasi particles,

$$P_0 = \frac{\sqrt{(s + M(Z')^2 - (2m_\mu)^2)^2 - 4sM(Z')^2}}{2\sqrt{s}}, \tag{3.1}$$

where M(Z') is the candidate mass, $2m_\mu = 0.210\ GeV/c^2$ is the dimuon mass and s=10.58^2 GeV$^2/c^4$ is the total invariant squared mass.
In 4μ background events, the dimuon CMS momentum $p_{\mu\mu}$ is expected to be strongly peaked around P_0, differently from the signal case, at least for two out of the four 4-track candidates. Therefore $p_{\mu\mu}$ is expected to be a very discriminating variable: this is actually shown in Figure 3.3, where the dimuon momentum is plotted for a 3 GeV/c^2 signal and background. The visible peak in the background distribution is the sign of this quasi two-body process. The quantity P_0 sets a feature for the 4μ background process and can be proficiently used to scale momentum-dependent variables of the event to reduce their mass dependence.

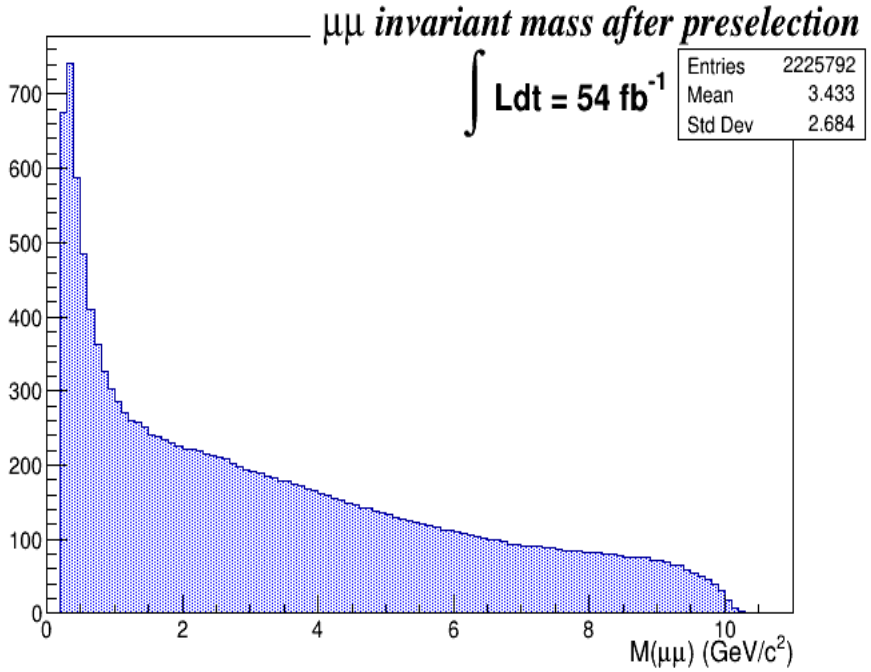

Figure 3.2: Dimuon mass $M(\mu\mu)$ shape produced by the SM four muon background. At this level of the analysis, we have four entries per event.

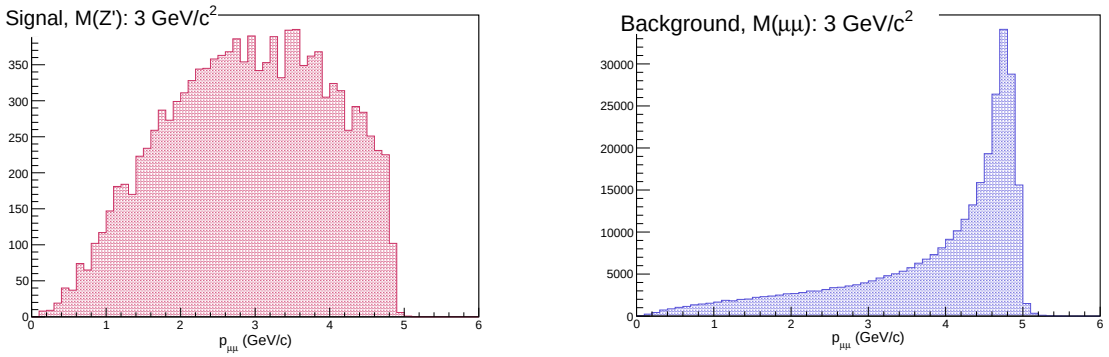

(a) Signal. **(b)** Background.

Figure 3.3: Candidate dimuon momentum $p_{\mu\mu}$ for a 3 GeV/c^2 signal (Figure 3.3a) and for the 4μ background, for a dimuon mass of 3 ± 0.25 GeV/c^2 (Figure 3.3b).

3.3.2 Muon identification

This analysis aim at selecting four muons final states. In order to have a good background reduction of processes with final state particles other than muons and to keep a reasonable signal efficiency, several combinations have been tested by requiring the number of tracks identified as muons and the μID threshold. An optimization is needed because, on one hand, being tight on muon identification reduces the background from sources with particles other than muons (typically pions in hadronic processes); on the other hand the dominant background is the SM four-muon process, for which this selection is almost transparent and the immediate consequence is a reduction of the signal efficiency.

The tested combinations are:

- at least 2 same-charge tracks identified as muons (the *BABAR* and Belle choice) with:
  - μID > 0.5;
  - μID > 0.9;
- at least 3 tracks identified as muons with:
  - μID > 0.5;
  - μID > 0.9;
  - μID > 0.9 for the tracks with same charge and μID > 0.5 for the spare muon;
- 4 tracks identified as muons with:
  - μID > 0.5;
  - μID > 0.9;

In order to select the best case among the ones proposed, the Punzi figure of merit (FOM) [31] (see section 3.3.5) has been evaluated. This is a frequentist definition of sensitivity, particularly suitable for optimization, being independent of a-priori expectations about the presence of a signal. In Figure 3.4 the Punzi FOM is shown before the final MVA selection (see subsection 3.3.5). The best result comes requiring at least three tracks identified as muons with μID > 0.9. Finally a μID greater than 0.9 for at least three out of four tracks in the event is requested. This selection is one of the major differences with respect to the previous analyses performed by Belle and *BABAR*, which only asked for tracks identified as muons.

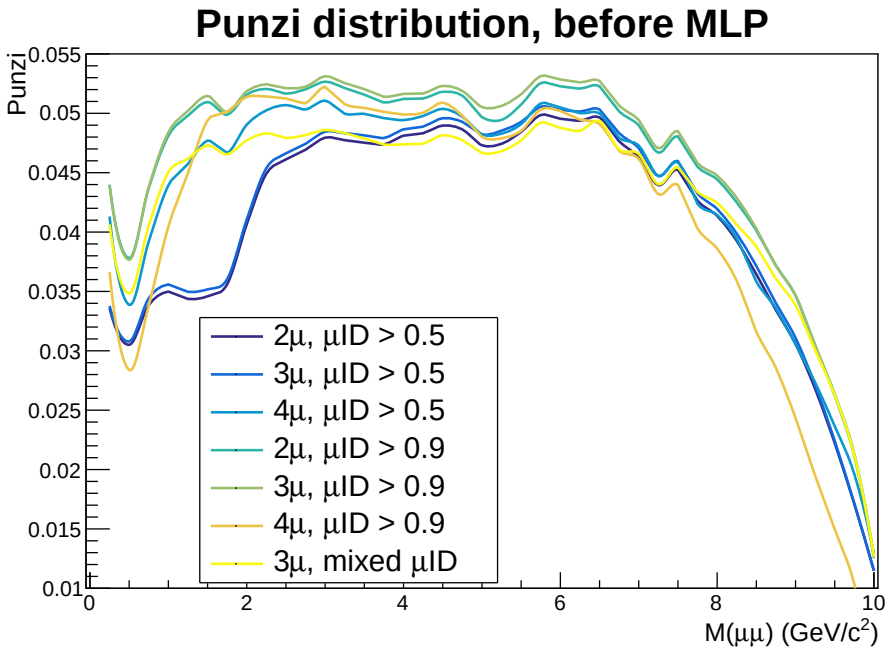

Figure 3.4: Punzi distributions as a function of the candidate mass for all combinations of the required number of identified muons and for different μID thresholds, after preselection, before MLP.

3.3.3 "ISR" cuts

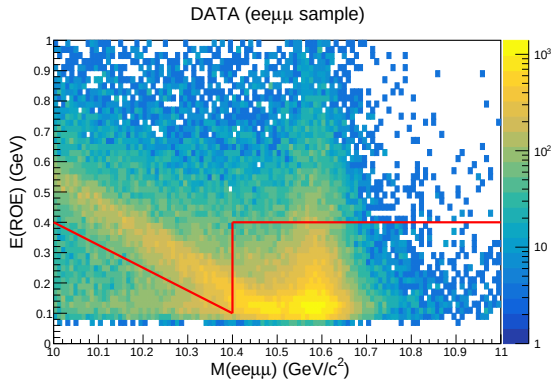

(a) ROE photon total energy as a function of the 4-track invariant mass.

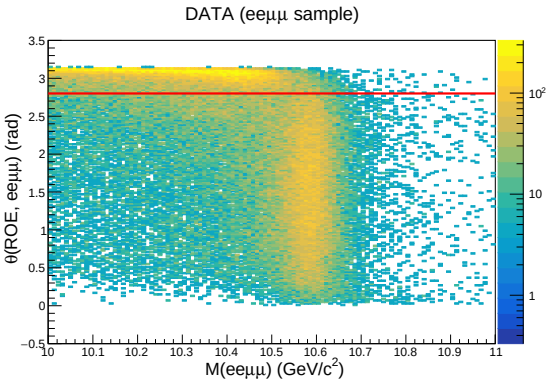

(b) three-dimensional angle between the ROE and the 4-track system direction as a function of the 4-track invariant mass.

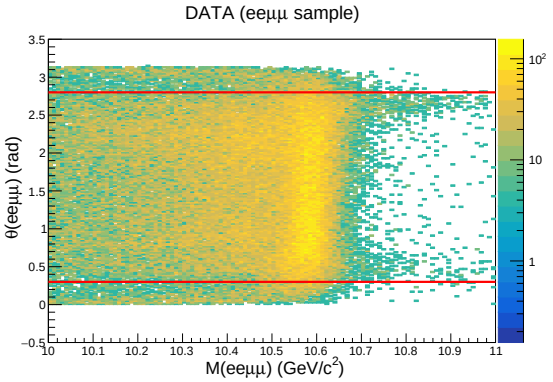

(c) polar angle θ direction of the 4-track system momentum as a function of the 4-track invariant mass.

Figure 3.5: Two-dimensional variables used to construct the "ISR" cuts. Red lines are superimposed in order to represent the ISR cuts studied.

The target of this study is to select events with four charged tracks, identified as muons, and no neutral depositions, in particular those due to photons. Requiring the absence of photons reduces drastically the possible background sources. ISR effects and beam backgrounds can cause signal events to contain photons too, so some price in terms of efficiency must be paid. As these effects happen on the background too, and the background is expected to be orders of magnitude above any reasonable signal, the signal-to-background ratio arising from this requirement is anyway very favourable to the selection.

Studies performed in Belle II showed that a reasonable requirement to suppress events with photons is to set an upper cut equal to 0.4 GeV on the total energy of the ECL clusters identified as photons. This requirement comes mostly from the beam background energy spectrum. The *Rest Of the Event* (ROE) is here defined as the system composed of all the detected photons. Then, it is always required that $E(\gamma_{ROE}) < 0.4$ GeV and considered the possibility of tightening the selection in special conditions, *i.e.* those related to the presence of ISR and, to a smaller extent, of Final State Radiation (FSR).

There are two kinds of ISR (and partly FSR) events expected:

1. **ISR/FSR with a hard photon emitted in acceptance** and detected by the ECL: in this case, for a single emission, the ISR/FSR photon is back to back with respect to the four reconstructed tracks and its energy is in a well defined kinematic relation with the invariant mass of the four reconstructed tracks;

2. **ISR with undetected photon**, emitted at low angle. This case is characterized by the presence of missing energy when the total momentum of the four reconstructed tracks points in the very forward or very backward direction.

Various technical problems in the ISR study needed to be considered: the SM 4μ dominant background is generated without ISR and FSR. A 4μ sample, selected on data, is not available for this analysis at this stage, because this is the signal region where one wants to unveil data, and cannot be unveiled before an official approval. Therefore a control sample is used, whose definition is postponed later in this thesis, the ee$\mu\mu$ control sample, with two identified electrons replacing two identified muons. The SM process ee$\mu\mu$ is generated without ISR and FSR as well, but in this case the data sample can be studied. Due to the presence of the two electrons, one expects also a strong FSR contribution in ee$\mu\mu$ events.

The most suitable ROE variables are shown in Figure 3.5

Figure 3.5a shows the total energy of the ROE photons as a function of the total 4-track invariant mass. Based on this two-dimensional distribution, the following cut was set:

$$E(\gamma_{ROE}) < E^*, \tag{3.2}$$

where:

$$E^* = \begin{cases} -0.75 \cdot M(ee\mu\mu) + 7.9 \text{ GeV} & \text{if } M(ee\mu\mu) < 10.4 \ GeV/c^2, \\ 0.4 \text{ GeV} & \text{if } M(ee\mu\mu) \geq 10.4 \ GeV/c^2. \end{cases} \tag{3.3}$$

The first cut removes the diagonal stripe visible in Figure 3.5a, due to the kinematic relation of the energy of the ISR (or FSR) photon with the 4-track invariant mass.

Figure 3.5b shows the two-dimensional distribution of the 3-dimensional angle θ between the ROE and the four-track system momentum directions, as a function of the four-track invariant mass M(ee$\mu\mu$). The horizontal band in the upper part of the distributions corresponds to the case in which a photon is emitted back-to-back with respect to the momentum direction of the 4-track system.

Therefore, the following further cut was applied:

$$\theta(\gamma_{ROE}, ee\mu\mu) < 2.8. \tag{3.4}$$

These selections are trivially generalized to 4-track final states different from ee$\mu\mu$, for example those of primary interest, $\mu\mu\mu\mu$. As far as the signal is concerned, the **MadGraph@5-NLO** [24] generator used includes ISR effects of point 2, but not those of point 1. The selections listed in this section will have therefore some impact on the signal efficiency, to be evaluated later in this thesis.

The selection described up to now is named and later referenced as "ISRB".

A further selection can be defined, to deal with case 2 (small angle ISR emission), not to be applied as an analysis cut, but intended to be used for specific checks. This selection rejects events where the CMS energy of the 4-track system is smaller than 10.4 GeV, an indication that some energy was carried away from the 4 tracks, and the total momentum polar angle direction points very forward or very backward (see Figure 3.5c). A selection "ISRC" is therefore defined, so that it includes ISRB and requires in addition that either E(ee$\mu\mu$) > 10.4 GeV or:

$$0.3 < \theta(ee\mu\mu) < 2.8 \qquad AND \qquad E(ee\mu\mu) < 10.4\ GeV.$$

3.3.4 Summary of event selection

In the following, the list of event selections applied is summarized, before entering into discussion about the final background suppression. Events selected must have:

1. exactly four reconstructed charged tracks with a total charge of zero;
2. invariant mass of the four-track system restricted between 10 and 11 GeV/c^2;
3. at least three identified muons (see section 3.3.2);
4. minimal activity in ECL. This is formalized through the ISRB requirement (see subsection 3.3.3), which sets an upper threshold to the total photon energy;

All these requirements are set at event level. An event that passes these selections produces four candidates, corresponding to the four possible neutral pairs eligible to be a Z' candidate.

3.3.5 Final background suppression

This is the central part of the analysis method and represents a major difference and improvement with respect to the approaches adopted by *BABAR* and Belle. The core idea is to find a set of variables which discriminate between signal and background and then combine them with an MVA technique, such that the background suppression overcompensates the unavoidable loss of efficiency and the final sensitivity overall improves. A useful fast quality indicator can be quantified with the variable $\frac{\varepsilon_S}{\sqrt{\varepsilon_B}}$, where ε_S and ε_B are the relative signal and background efficiencies resulting from the application of the MVA selection only. More precisely, ε_S and ε_B are the fraction of events surviving the MVA selection. The quantity $\frac{\varepsilon_S}{\sqrt{\varepsilon_B}}$ can be read as a rough measure of the increase in sensitivity following the MVA selection: when $\frac{\varepsilon_S}{\sqrt{\varepsilon_B}} > 1$, it is profitable.

Discriminant variables

it is important to recall here that, at this level of the analysis, each event provides four different 4-track candidates, corresponding to the four different neutral track pairs. Within each 4-track candidate, it will be indicated as "candidate tracks" the two tracks candidate to come from a Z' decay, and "recoil tracks", the other two tracks in the event. A signal is defined as the 4-track candidate in which both candidate tracks comes from the Z' decay, according to the MC truth. Each event therefore contributes

with a single 4-track candidate in case of signal and with four 4-track candidates for the background. When referring to mass, this is intended as the invariant mass of the candidate track pair, which is the Z' mass, within the experimental resolution, in the signal case.

These tracks are always muons in the case of signal and of the largely dominant background, the SM 4μ process. For this reason, they will be called "muons" in the following of this section, even if they are not always identified as such (as also events with 3 identified muons too are accepted, see subsection 3.3.2).

After a long and detailed study, the considered discriminant variables are the following (all in the center-of-mass frame):

- $p_{\mu\mu}$: candidate **muon pair momentum**;
- p_{μ_0} and p_{μ_1}: **candidate single muon momenta**;
- pt_{μ_0} and pt_{μ_1}: **candidate single muon transverse momenta**;
- $p^{rec}_{\mu_0}$ and $p^{rec}_{\mu_1}$: **recoil single muon momenta**;
- $pt^{rec}_{\mu_0}$ and $pt^{rec}_{\mu_1}$: **recoil single muon transverse momenta**;
- $P^T(p^{rec}_{\mu\mu}, p_{min})$ and $P^T(p^{rec}_{\mu\mu}, p_{max})$: **transverse projection of the recoil dimuon momentum** on minimum and maximum candidate muon momentum direction;
- $P^T(p_{max}, p^{rec}_{min})$ and $P^T(p_{max}, p^{rec}_{max})$: **transverse projection of maximum candidate muon momentum** on minimum and maximum recoil momentum;
- $P^T(p_{min}, p^{rec}_{min})$ and $P^T(p_{min}, p^{rec}_{max})$: **transverse projection of minimum candidate muon momentum** on maximum and minimum recoil momentum;

All the variables listed above, but the first, have been studied and combined based on their two-dimensional relations. These variables underwent a careful processing before the actual usage in an MVA algorithm: this step played an important role in making the inputs more homogeneous, so to drastically reduce the dependence on the Z' mass. Examples are shown in Figure 3.6 and Figure 3.7, where two pairs out of all the variables used as inputs for the MVA are compared in 2D plots before and after the processing, for different Z' masses, in ranges of ± 0.25 GeV/c^2. The dependence on the Z' mass is drastically reduced after handling the variables.

In the following, these variables are shown for signal (top) and background (bottom), in a mass interval of 3 ± 0.25 GeV/c^2, before (left) and after (right) the processing.

The very first example was actually in Figure 3.3, where the candidate dimuon momentum is shown. In Figure 3.8 the same variable is shown before and after being scaled by the characteristic quasi-two-body momentum P_0, defined in Equation 3.1, through the relation $p_{\mu\mu}/(P_0 - 1)$.

In Figure 3.9 the two-dimensional distribution of the single candidate muon momenta is shown. Here the difference between signal and background is such that the former populates a middle-bottom region of the distribution, while the latter concentrates in the extreme upper edges. The linear upper border of the distribution (left plots) is determined by the relation $p_{\mu_0} + p_{\mu_1}{=}P_0$, which holds for a two-body final state. In the background case, events stay preferentially along the line (being quasi-two-body) with one of the two muons that tends to carry the full available momentum.

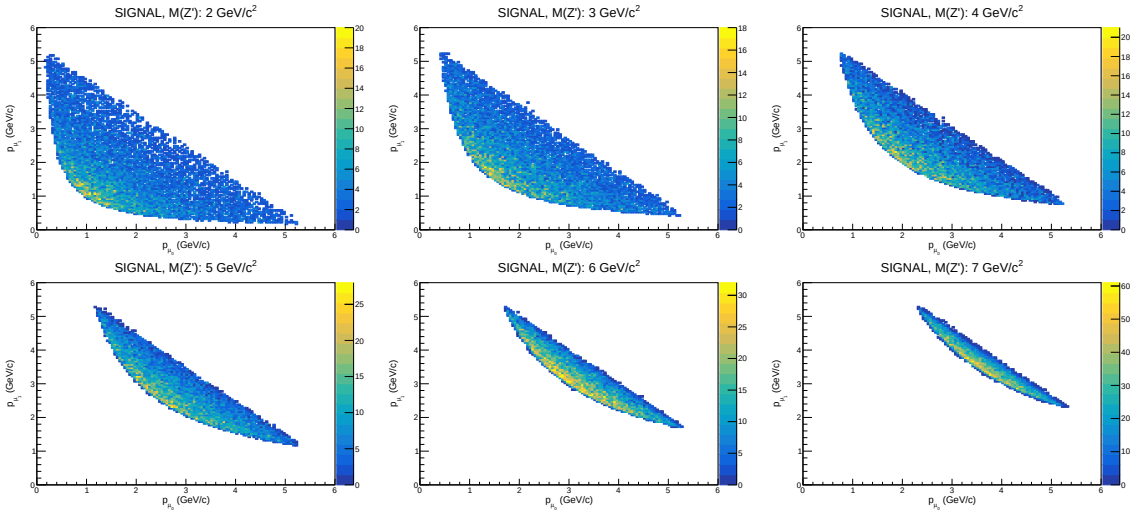

(a) before the processing.

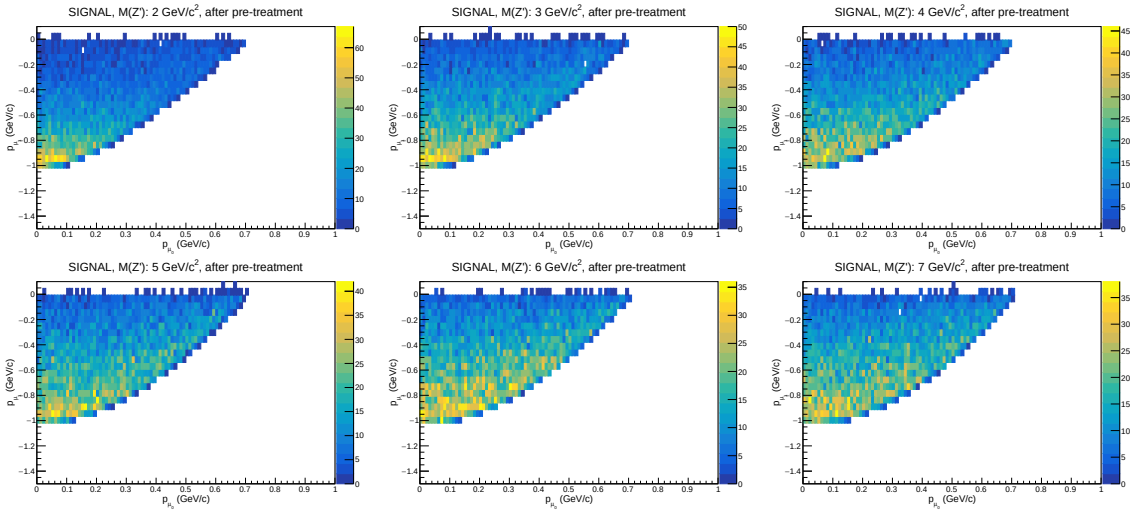

(b) after the processing.

Figure 3.6: $p_{\mu 1}$ vs. $p_{\mu 0}$ for some signal Z' masses, before (a) and after (b) the processing.

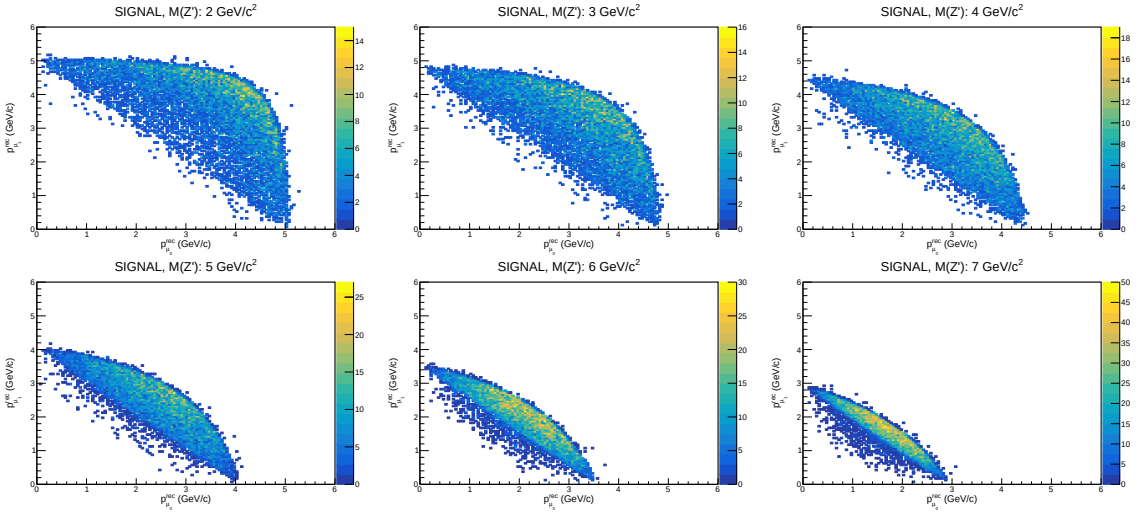

(a) before the processing.

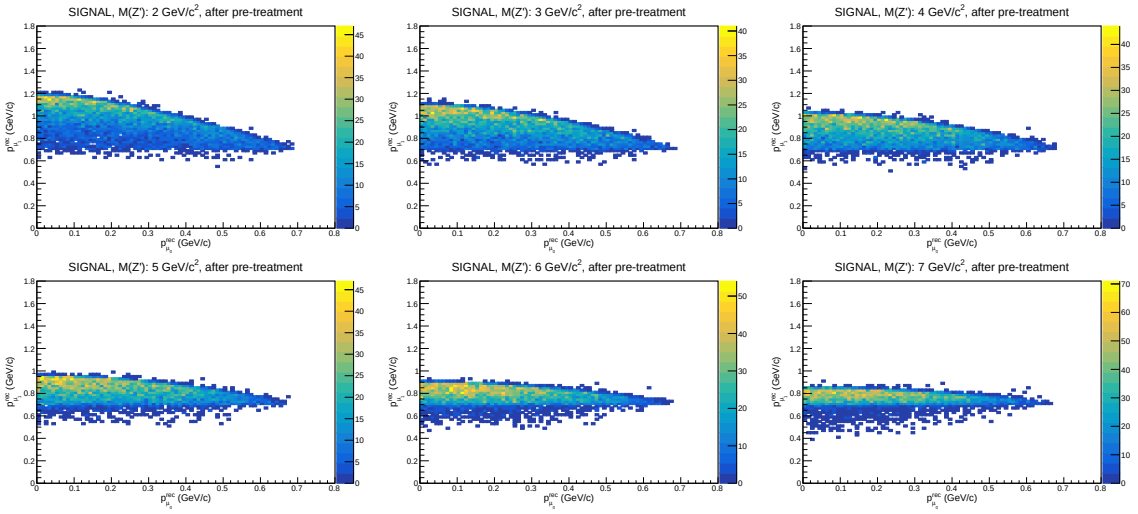

(b) after the processing.

Figure 3.7: $p^{rec}_{\mu_1}$ vs. $p^{rec}_{\mu_1}$ for some signal Z' masses, before (a) and after (b) the processing.

In the signal case, events accumulate far from the upper border, because they are not quasi-two-body-like, and the two muons share more democratically the available momentum, as they come from a resonance decay. The variable pair (p_{μ_0}, p_{μ_1}) has been 90° rotated in the plane of the two momenta and scaled by P_0: results are shown in the right plots.

A very similar processing has been performed on the variable pair ($p^{rec}_{\mu_0}$, $p^{rec}_{\mu_1}$) and ($pt^{rec}_{\mu_0}$, $pt^{rec}_{\mu_1}$), which are shown in Figure 3.12 and in Figure 3.13. In this case, the muon pair is opposite to the Z' candidate one and the distribution is limited by the same straight line as before, but in the bottom part (rather than in the upper part).

A different processing has been applied to the distribution of the transverse momenta of the candidate muons. They are shown one versus the other in Figure 3.10. Candidates, both for the signal and the background, cluster around an hyperbolic shape. This is the kinematical consequence of the fact that the two muons have a well defined invariant mass, either because they come from a resonance (signal) or because they are forced to have that mass due to the scanning procedure (background). The ultimate reason for the hyperbolic relation is that the invariant mass squared is proportional to $p_0 \times p_1 \times (1 - cos\theta)$. Defining the variables in Figure 3.10 as x and y, the hyperbole is expressed with a simple equation of the type $y = \frac{k}{x}$, where k can be computed from kinematics and turns out to be $k = \frac{\sqrt{s}}{2} \times (\frac{\sqrt{s}}{2} - P_0)$. Signal and background, on the other hand, differ because the former populates preferentially the central part of the hyperbole and the latter the two extremes. In order to make use of this feature, the generic point of the plane along the hyperbole is projected, so one can define a new variable sensitive to its position: this is illustrated in Figure 3.11. By projection it is meant here the intersection of the hyperbole with the line passing through the generic point and orthogonal to the hyperbole. A generic point of coordinates (x_0, y_0) has a projection on the hyperbole of equation $y = \frac{k}{x}$ whose coordinates (x_1, y_1) are defined by the equations:

$$ {x_1}^4 - x_0 {x_1}^3 + k y_0 x_1 - k^2, \tag{3.5} $$

and:

$$ y_1 = \frac{k}{x_1}. \tag{3.6} $$

The first variable constructed is the asymmetry:

$$ A(pt_{\mu_0}, pt_{\mu_1}) = \frac{I_1 - I_2}{I_1 + I_2}, \tag{3.7} $$

where I_1 and I_2 are curvilinear coordinates along the hyperbole defined by the projection (see Figure 3.11) and measure quantitatively how much a point is placed in a central or in an endpoint position. The second variable, much less discriminating, is the signed distance between the points (x_0, y_0) and (x_1, y_1), so how much a point is far from the hyperbole:

$$ D(pt_{\mu_0}, pt_{\mu_1}) = \sqrt{(x_1 - x_0)^2 + (y_1 - y_0)^2}. \tag{3.8} $$

The plot of $D(pt_{\mu_0}, pt_{\mu_1})$ versus $A(pt_{\mu_0}, pt_{\mu_1})$ is shown in Figure 3.10, right plots.

Regarding the variables that contains projections, not shown here, they underwent a polar coordinate transformation in the plane in which they are expressed one versus the other.

Finally, a list of all the variables after the processing, ranked in order of separation as result of the training, can be found in Table 3.2.

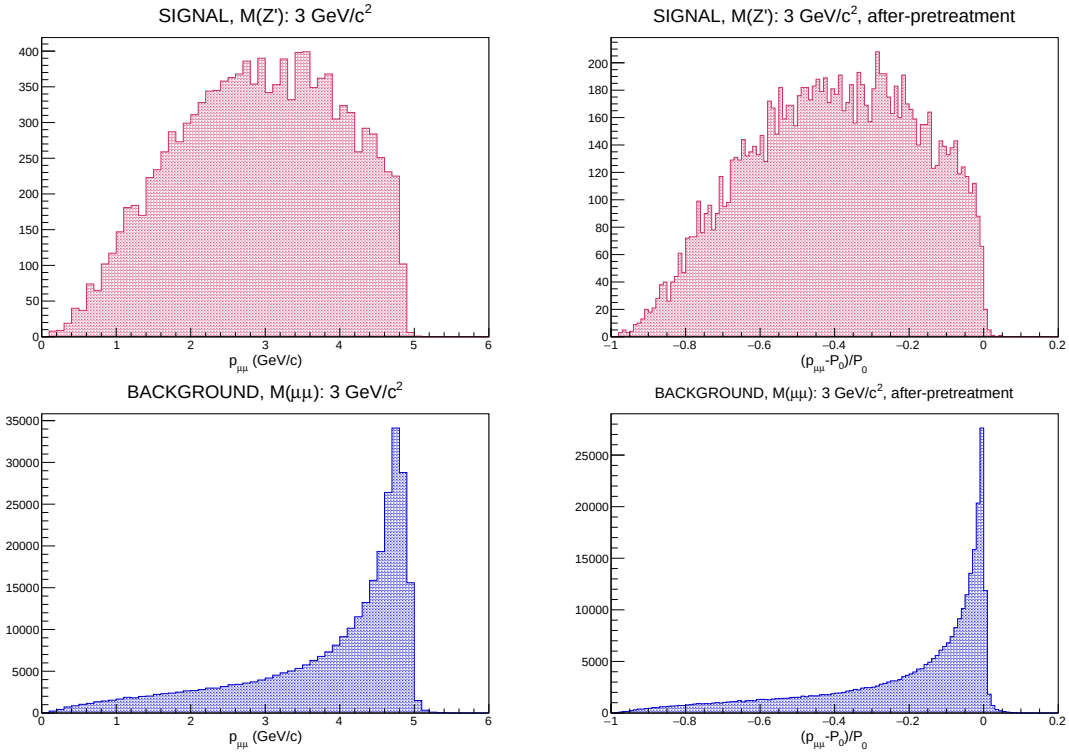

Figure 3.8: Candidate dimuon momentum distribution, for a 3 GeV/c^2 signal (top) and 3 $\pm$ 0.25 GeV/c^2 background (bottom), before (left) and after (right) the processing.

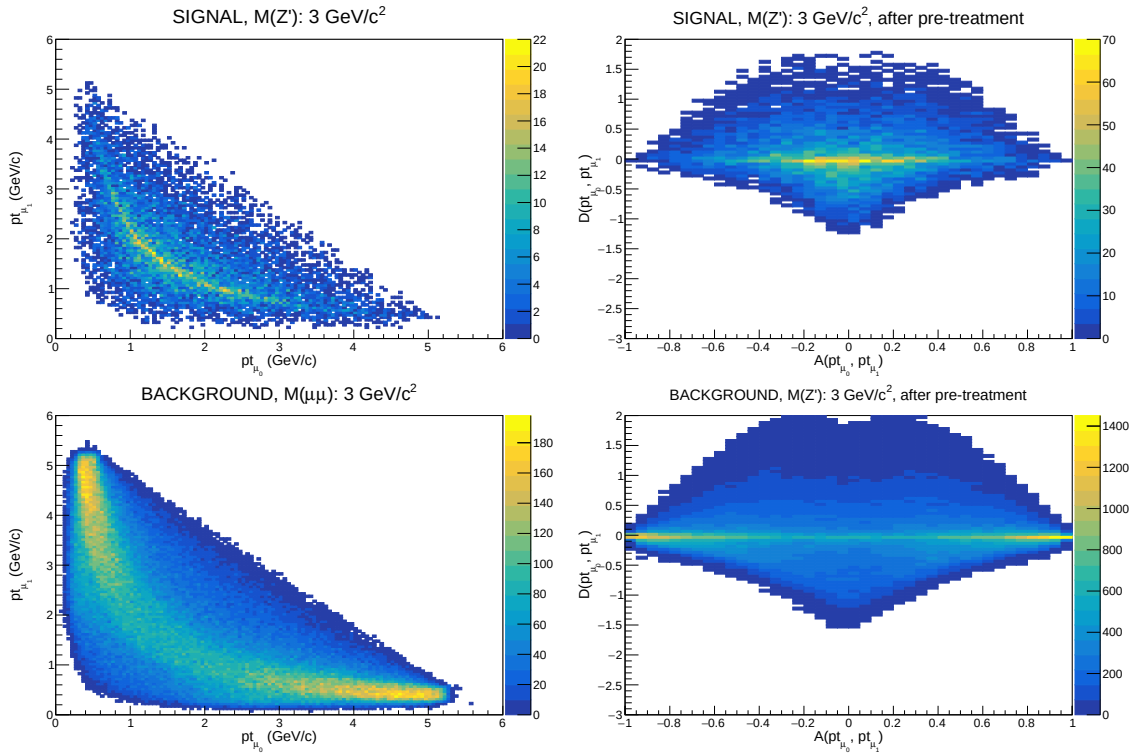

Figure 3.10: Candidate muon transverse momentum 2D distribution, for 3 GeV/c^2 signal (top) and 3 ± 0.25 GeV/c^2 background (bottom), before (left) and after (right) the processing for 3 a GeV candidate mass.

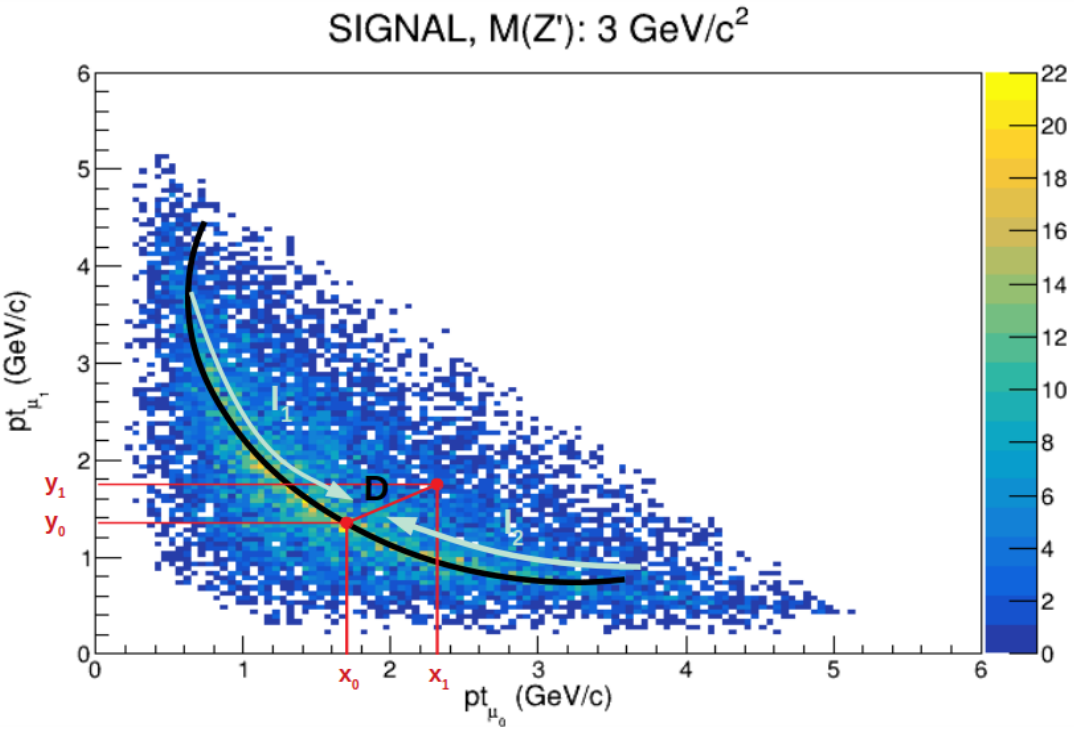

Figure 3.11: Construction of two discriminant variables starting from candidate single muon transverse momenta.

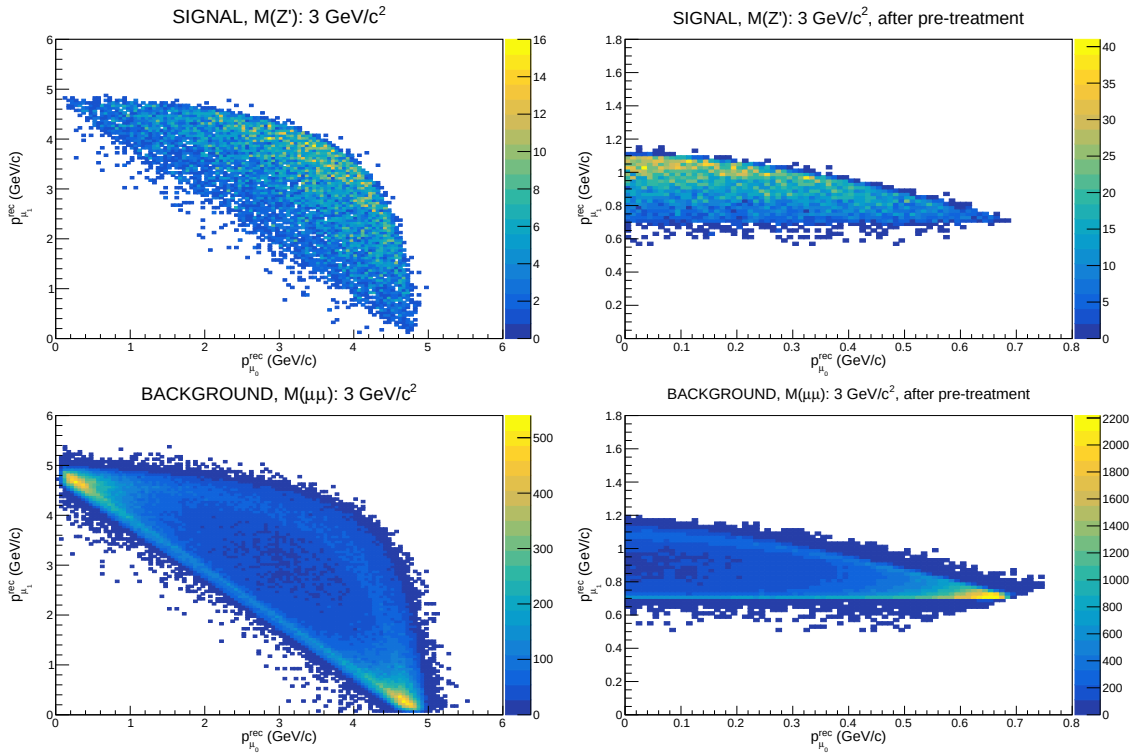

Figure 3.12: Recoil muon momentum 2D distribution, for 3 GeV/c^2 signal (top) and 3 $\pm$ 0.25 GeV/c^2 background (bottom), before (left) and after (right) the processing.

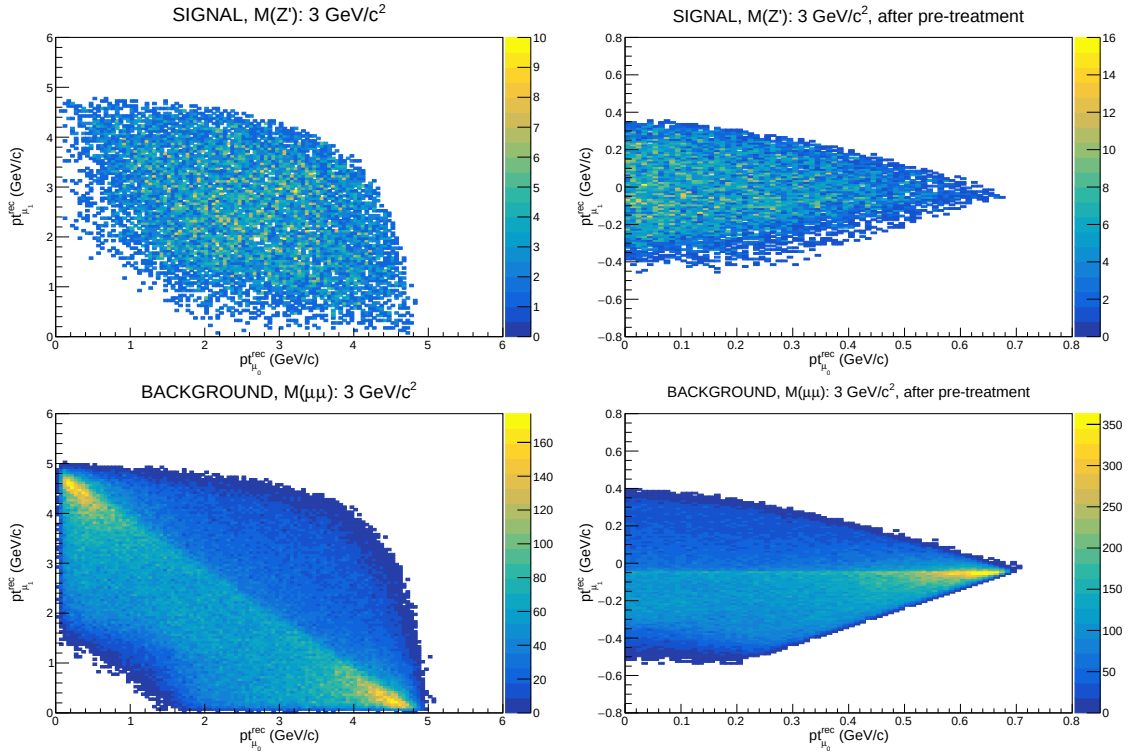

Figure 3.13: Recoil muon transverse momentum 2D distribution, for a 3 GeV/c^2 signal (top) and a 3 $\pm$ 0.25 GeV/c^2 background (bottom), before (left) and after (right) processing.

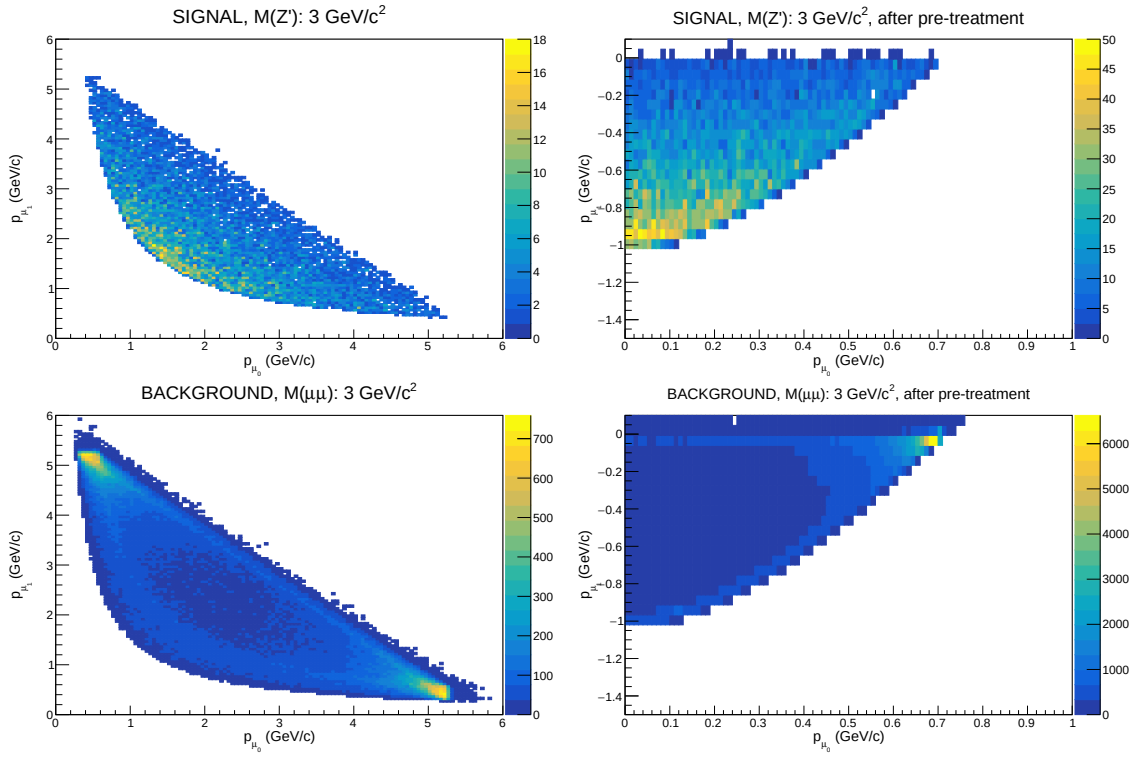

Figure 3.9: Z' muon momentum 2D distribution, for a 3 GeV/c^2 signal (top) and 3 $\pm$ 0.25 GeV/c^2 background (bottom), before (left), and after (right) the processing for 3 GeV candidate mass.

Multi Variate Analysis

After a careful comparison between different MVA algorithms the *Multi Layer Perceptron* (MLP) Neural Network algorithm turned out to be the most suitable for this analysis porpuses. An MLP structure is composed of: *input neurons*, some *hidden layers* and one or more *output neurons*. The network here described is made of 15 input variables, 1 hidden layer of 20 neurons, 1 output neuron. Several attempts were made to optimize the size of the hidden layer: using less than 20 neurons degraded the final performances, while using more than 20 neurons gave marginal improvements at the expense of computing time dilations and probability of incurring in overtraining issues.

Any possible effort was employed to avoid the MLP to learn patterns specific of some mass hypothesis. The processing of the input variables explained in the previous section was aimed at that goal. Another handle was the usage of very "dense" signal samples in the training, that is sets of signals generated at many masses in small steps, so to approximate a continuous mass distribution. Specifically, for the MLP training and test two independent, dense signal samples are used, with generated mass from 220 MeV/c^2 to 10 GeV/c^2at 5 MeV/c^2 steps (5000 events for each mass), a four-muon background sample corresponding to 5 ab^{-1} integrated luminosity, and a $\mu\mu(\gamma)$ sample corresponding to 100 fb^{-1} luminosity. After long and detailed studies, a configuration of four different mass intervals was set, each with its MLP. Therefore 4 different nets have been trained, splitting the mass spectrum in 4 mass regions (also named "MLP ranges" in the following) in order to keep into account the variability of the background shape: 0.0-0.5 GeV/c^2, 0.5-1.0 GeV/c^2, 1.0-7.0 GeV/c^2 and 7.0-10.0 GeV/c^2.

The effect of the trigger was taken into account using the measured efficiencies as event weights (see section 3.4). The contributions of the different background processes were weighted by their respective simulated luminosities. All the event selections (see subsection 3.3.4) were applied.

For each mass range the output of the MLP algorithm returns:

- the variable separation ranking, shown in Table 3.2;
- the ROC curves, shown in Figure 3.14. They represent the background rejection as a function of the signal efficiency. The nearer to 1 is the area of this curve the better is the net performance;
- the output neuron of the net, shown in Figure 3.15 for signal and background. The best separation happens to be in the third and the fourth mass ranges. The low mass region is, not surprisingly, more difficult, because the background is higher and the 4μ ISR diagram contributes heavily.

The following figure of merit can be defined (see previous section (3.3.4)):

$$f.o.m. = \frac{\epsilon_S}{\sqrt{\epsilon_B}}, , \tag{3.9}$$

that can be interpreted as the increase of sensitivity due to the usage of the MVA selection and can be found in Figure 3.16 as a function of the MLP output and in Figure 3.17 as a function of the signal efficiency. When $\frac{\varepsilon_S}{\sqrt{\varepsilon_B}} > 1$ the application of the net is convenient.

Table 3.2: Ranking of the input processing variables for the four MLP mass ranges.

Rank	0-0.5 GeV/c^2	0.5-1 GeV/c^2	1-7 GeV/c^2	7-10 GeV/c^2
1.	$p^{rec}_{\mu_1}$	$p^{rec}_{\mu_1}$	$p^{rec}_{\mu_1}$	$p_{\mu\mu}$
2.	$p_{\mu\mu}$	$p_{\mu\mu}$	$p_{\mu\mu}$	p_{μ_1}
3.	p_{μ_1}	$p^{rec}_{\mu_1}$	$P^T(p_{min}, p^{rec}_{max,min})_\rho$	$P^T(p_{max}, p^{rec}_{max,min})_\rho$
4.	$pt^{rec}_{\mu_1}$	$pt^{rec}_{\mu_1}$	p_{μ_0}	$P^T(p_{min}, p^{rec}_{max,min})_\rho$
5.	$A(pt_{\mu_0}, pt_{\mu_0})$	$A(pt_{\mu_0}, pt_{\mu_0})$	$P^T(p^{rec}_{\mu\mu}, p_{max,min})_\theta$	$p^{rec}_{\mu_1}$
6.	p_{μ_0}	p_{μ_0}	$P^T(p_{max}, p^{rec}_{max,min})_\rho$	p_{μ_0}
7.	$D(pt_{\mu_0}, pt_{\mu_1})$	$P^T(p_{max}, p^{rec}_{max,min})_\theta$	$p^{rec}_{\mu_1}$	$P^T(p^{rec}_{\mu\mu}, p_{max,min})_\rho$
8.	$P^T(p_{max}, p^{rec}_{max,min})_\theta$	$p^{rec}_{\mu_0}$	$p^{rec}_{\mu_0}$	$P^T(p^{rec}_{\mu\mu}, p_{max,min})_\theta$
9.	$P^T(p_{min}, p^{rec}_{max,min})_\theta$	$P^T(p_{min}, p^{rec}_{max,min})_\theta$	$P^T(p_{max}, p^{rec}_{max,min})_\theta$	$A(pt_{\mu_0}, pt_{\mu_1})$
10.	$P^T(p_{max}, p^{rec}_{max,min})_\rho$	$pt^{rec}_{\mu_0}$	$A(pt_{\mu_0}, pt_{\mu_1})$	$p^{rec}_{\mu_0}$
11.	$P^T(p^{rec}_{\mu\mu}, p_{max,min})_\rho$	$D(pt_{\mu_0}, pt_{\mu_1})$	$pt^{rec}_{\mu_0}$	$pt^{rec}_{\mu_1}$
12.	$P^T(p_{min}, p^{rec}_{max,min})_\rho$	$P^T(p^{rec}_{\mu\mu}, p_{max,min})_\theta$	$P^T(p_{min}, p^{rec}_{max,min})_\theta$	$D(pt_{\mu_0}, pt_{\mu_1})$
13.	$p^{rec}_{\mu_0}$	$P^T(p_{max}, p^{rec}_{max,min})_\rho$	$pt^{rec}_{\mu_1}$	$P^T(p_{min}, p^{rec}_{max,min})_\theta$
14.	$pt^{rec}_{\mu_0}$	$P^T(p^{rec}_{\mu\mu}, p_{max,min})_\rho$	$P^T(p^{rec}_{\mu\mu}, p_{max,min})_\rho$	$P^T(p_{max}, p^{rec}_{max,min})_\theta$
15.	$P^T(p^{rec}_{\mu\mu}, p_{max,min})_\theta$	$P^T(p_{min}, p^{rec}_{max,min})_\rho$	$D(pt_{\mu_0}, pt_{\mu_1})$	$pt^{rec}_{\mu_0}$

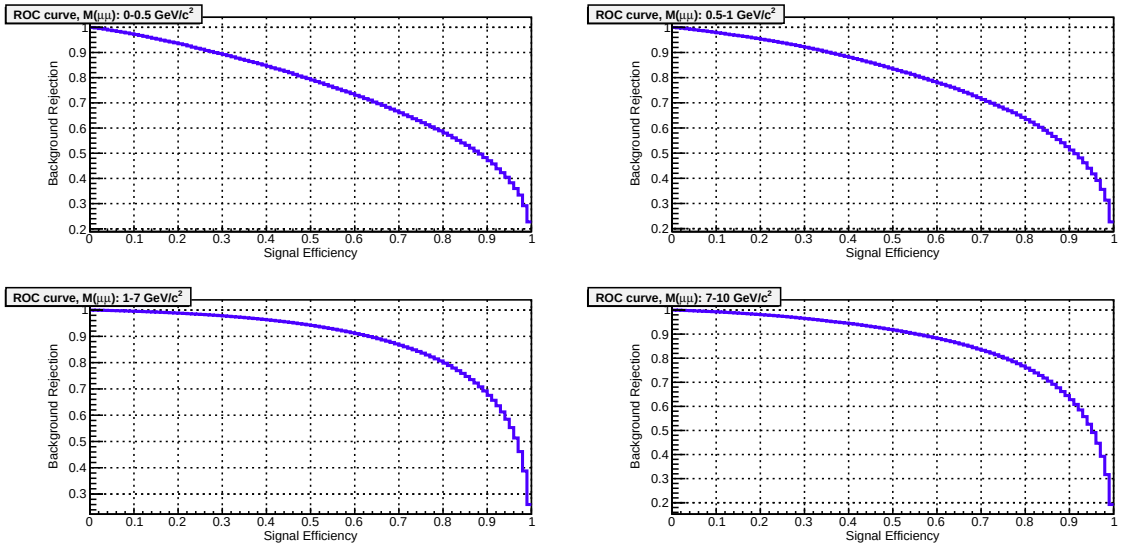

Figure 3.14: ROC curves for the four MLP mass ranges. A ROC curve is the background rejection as a function of the signal efficiency.

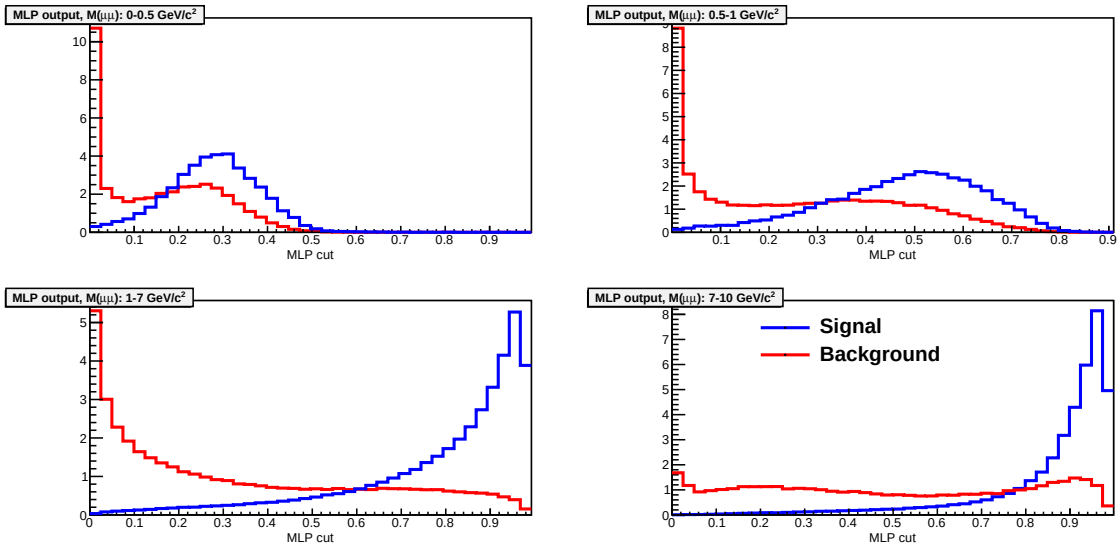

Figure 3.15: MLP output neurons for the four MLP mass ranges. Red is the background, blue is the signal. According to these distributions one can evaluate the most suitable cut for the best signal and background separation.

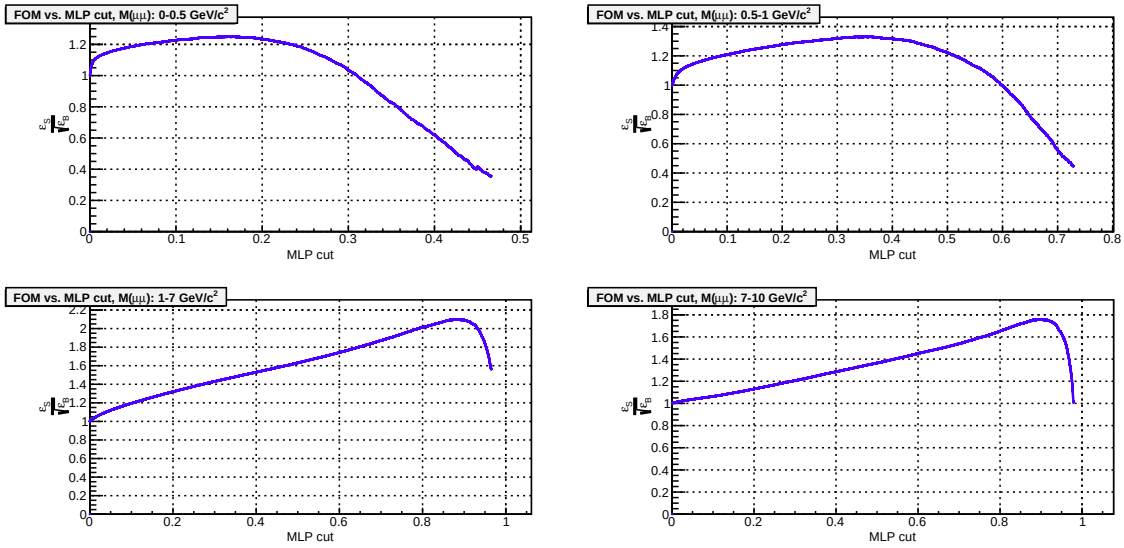

Figure 3.16: Figure of merit defined in Equation 3.9 as a function of the network output, for the four MLP mass ranges.

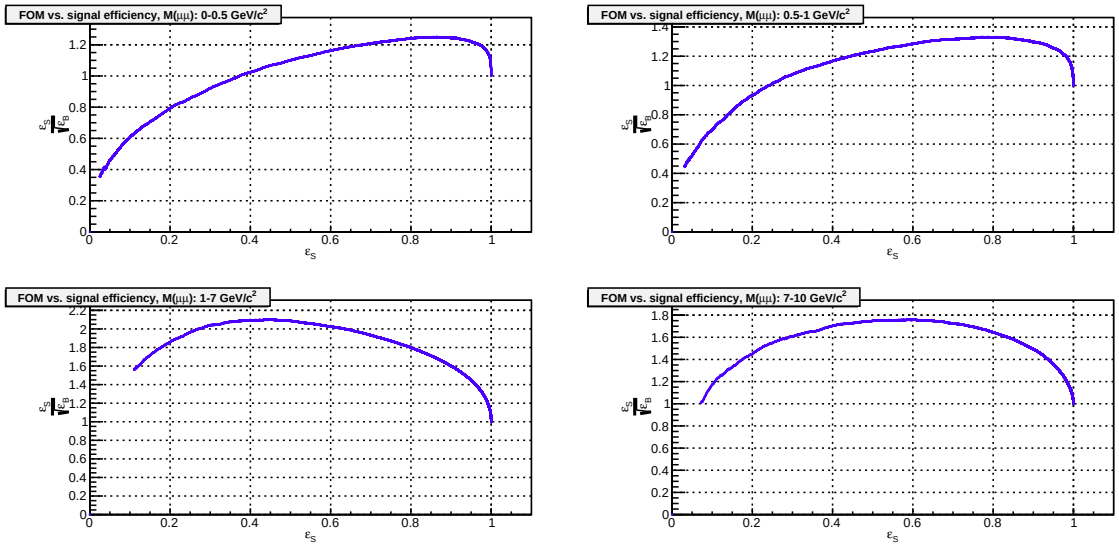

Figure 3.17: Figure of merit defined in Equation 3.9 as a function of the relative signal efficiency for the four MLP mass ranges.

Optimization of the MLP selection: "analytical cut"

The figure of merit presented in the previous section was very useful for a fast evaluation of the net performances during the studies dedicated to the choice of the set of input variables, number of hidden layers, training and test sample, definition of signal and background events, etc.... For the usage in the analysis as the final background suppressing selection, the cut to be applied on the net output was optimized using a **Punzi** figure of merit [31], defined by the equation:

$$P(t) = \frac{\varepsilon(t)}{a/2 + \sqrt{B(t)}}, \tag{3.10}$$

where $\varepsilon(t)$ is the absolute signal efficiency after all the analysis selections at a given cut t, a is the number of σ corresponding to the chosen significance level, in this case a=1.64 (corresponding to one-sided 3σ significance), and *B(t)* is the number of background events left after the cut t.

In order to have the best possible performances, the cut on the neuron output was optimized as a function of the mass, through a set of 20 signal masses above 1 GeV/c^2 and 20 additional masses from 0.212 GeV/c^2 to 1 GeV/c^2. A distribution of the Punzi figure of merit has been performed as a function of the cut t for each mass point, the value of t that maximizes the *P(t)* is the most suitable cut for that mass hypothesis. This value as a function of the candidate dimuon mass was fitted in 3 regions:

- **region 1**: $0.210 \leq M(\mu\mu) < 1$ GeV/c^2 (2^{nd} order polynomial);
- **region 2**: $1 \leq M(\mu\mu) < 7$ GeV/c^2 (4^{th} order polynomial);
- **region 3**: $7 \leq M(\mu\mu) < 10$ GeV/c^2 (4^{th} order polynomial).

Finally, the cut is "analytical" and it is a function of the mass, allowing to interpolate the best value also for masses between one generated point and another: in the following it will be called "analytical cut".

In Figure 3.18 an example of the Punzi distribution and the quantities used to construct it are shown, for a Z$'$ mass equal to 5 GeV/c^2. The maximum of the Punzi distributions as a function of the candidate dimuon mass, is shown in Figure 3.19.

Finally, the signal efficiency after the application of the optimized analytical cut obtained by this study as a function of the M(Z') is shown in Figure 3.20, while the number of background events left from the selection as a function of M($\mu\mu$), compared with the distribution before the MLP application are shown in Figure 3.21.

As the MLP selection is applied separately for each of the four 4-track candidates coming from an event, the combinatorial background is considerably reduced: the condition under what one event always provides four Z' candidates is no longer verified.

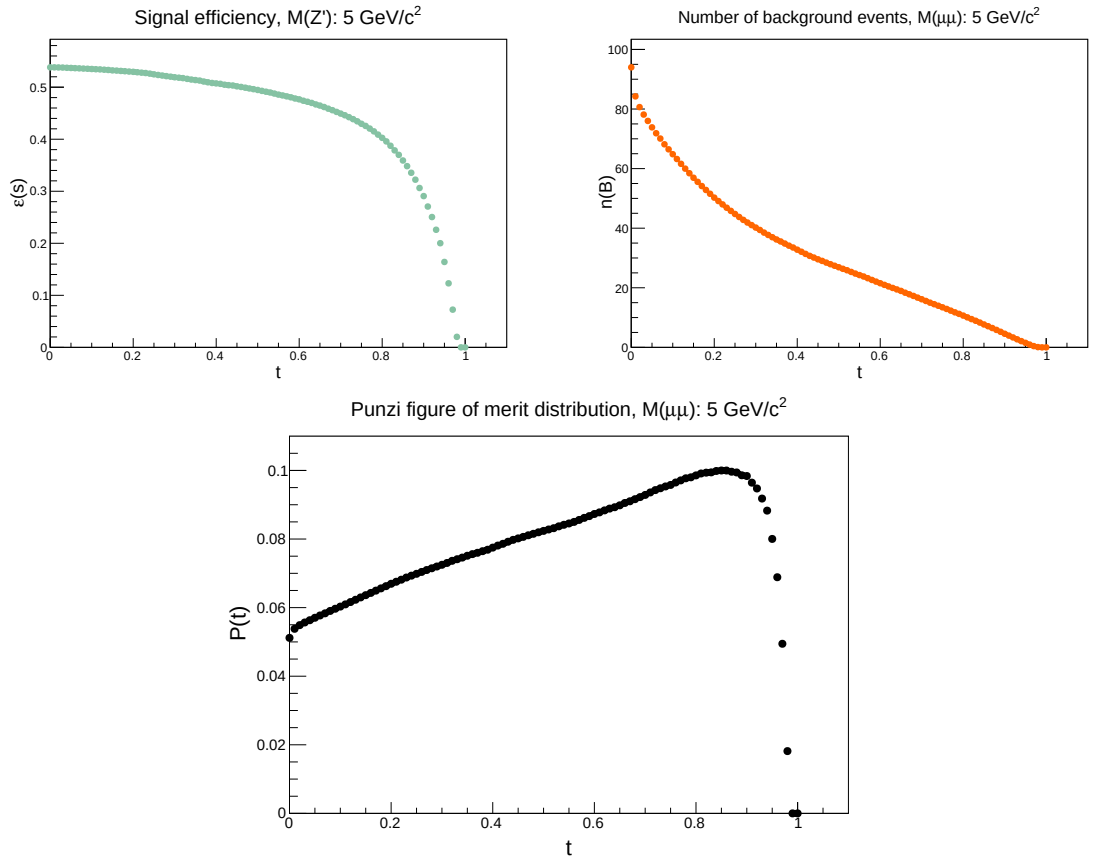

Figure 3.18: **Top-left**: Signal efficiency as a function of the cut t on the MLP output. **Top-right**: Number of background events left as a function of the cut t on the MLP output. **Bottom**: Punzi FOM distribution computed using Equation 3.10 as a function of the cut t on the MLP output.

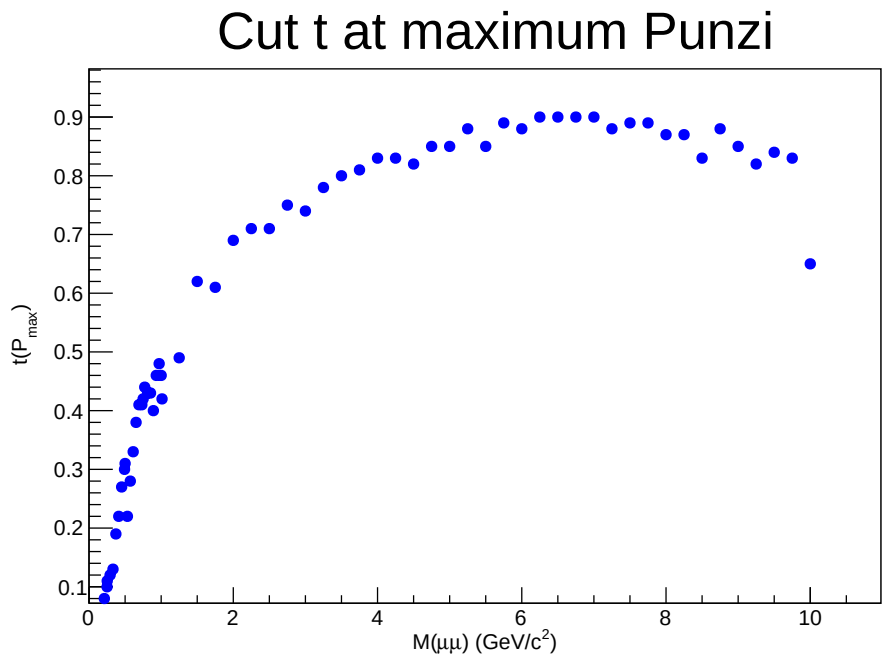

Figure 3.19: Value of the cut that maximizes the Punzi FOM distribution $P(t)$ as a function of the mass.

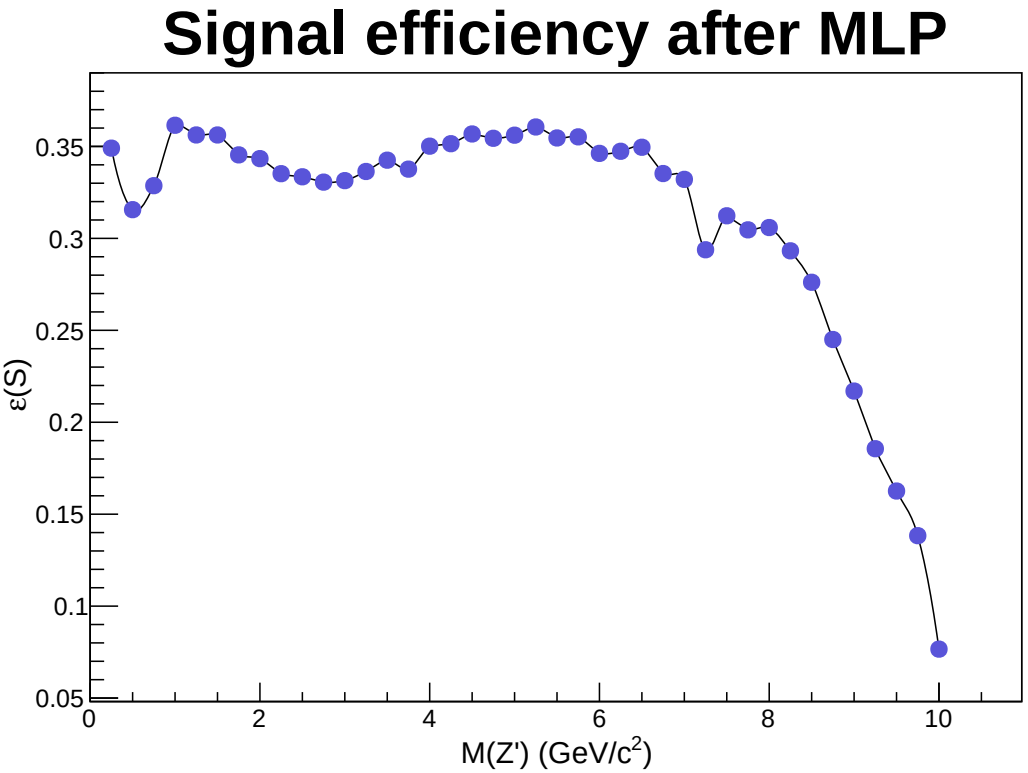

Figure 3.20: Signal efficiency after the optimized cut application on the MLP output as a function of the Z' mass.

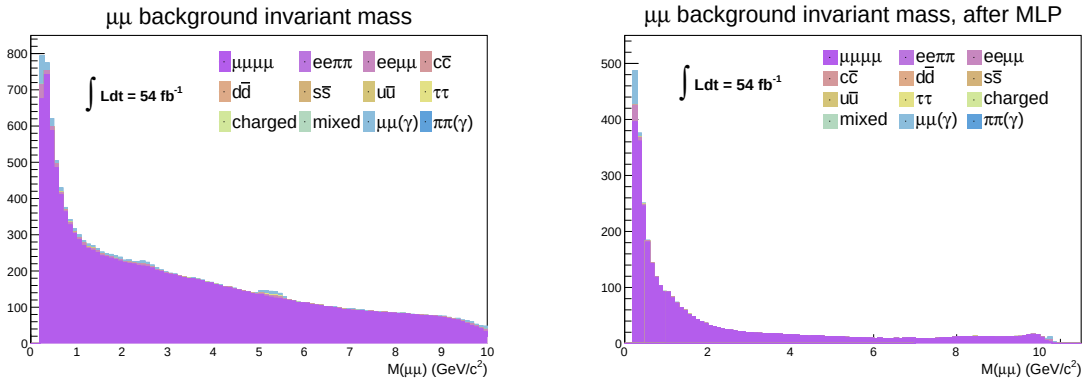

(a) before MLP. **(b)** after MLP.

Figure 3.21: dimuon candidate invariant mass background distribution before (3.21a) and after (3.21b) MLP application. The main contributions come from $\mu^+\mu^-\mu^+\mu^-$ and $\mu^+\mu^-(\gamma)$ processes.

3.4 Trigger

This measurement makes use of two trigger lines in logical OR: the CDC fff and the CDCKLM. The CDC fff trigger requires the presence of at least 3 tracks with polar angles approximately in the barrel. The CDCKLM is the logical OR of the four CDCKLMn exclusive trigger lines, which require n CDC tracks matched with barrel KLM clusters, with 8 layers fired as minimum. The CDCKLM single muon trigger efficiency has been studied in an internal Belle II study, from which Table 3.22

id	θ [°]	p [GeV/c]	Efficiency	Systematic Uncertainty				
				θ-p	ϕ	nCDCHits	run	Total**
100	51 - 117	>1.2	0.888±0.001	0.058	0.000	0.006	0.007	0.059
0	43 - 51	0.75 - 2.0	0.346±0.004	0.263	0.049	0.009	0.010	0.264
1	43 - 51	2.0 - 6.0	0.554±0.003	0.275	0.040	0.002	0.008	0.275
2	51 - 78	0.75 - 1.4	0.521±0.003	0.053	0.032	0.005	0.016	0.056
3	51 - 78	1.4 - 5.5	0.932±0.001	0.013	0.019	0.002	0.004	0.014
4	78 - 84	0.75 - 1.4	0.442±0.006	0.060	0.062	0.004	0.019	0.063
5	78 - 84	1.4 - 5.0	0.807±0.003	0.068	0.038	0.008	0.019	0.071
6	84 - 117	0.75 - 1.4	0.567±0.003	0.031	0.050	0.009	0.020	0.038
7	84 - 117	1.4 - 5.0	0.865±0.001	0.024	0.027	0.007	0.007	0.026
8	117 - 125	0.75 - 2.0	0.381±0.006	0.299	0.088	0.008	0.023	0.300
9	117 - 125	2.0 - 4.5	0.568±0.007	0.287	0.057	0.011	0.026	0.289
c	112 - 125	0.75 - 1.2	0.175±0.011	0.110	0.076	0.012	0.014	0.112
c	112 - 125	1.2 - 4.5	0.351±0.007	0.079	0.140	0.016	0.023	0.084

Figure 3.22: single muon trigger efficiencies in different momentum and polar angle intervals, for μID > 0.5. The last two lines, marked with $*$, refer to the chimney region. The error in the efficiency column is statistical only. Also shown are the estimated systematic uncertainties. The region marked with id=100 corresponds to a wider angular and momentum selection. $**$ Contributions due to the azimuthal angle ϕ shown, but not included in the total.

is taken. Based on this table, a CDCKLM event trigger probability is computed, building the logical OR of the single muon efficiencies, depending on the number of identified muons in the event and on their momentum and polar angle direction. This trigger is very effective for signal events, as they contain four muons. The CDCKLM trigger efficiency is shown in Figure 3.23 as a function of the Z' mass.

As there were no public available results for the fff trigger efficiency suitable for this analysis, it was evaluated from scratch. The first attempt was the one making use of the $e^+e^-\mu^+\mu^-$ control sample. Bucket9, bucket10, bucket11, bucket13, bucket14, bucket15 were reconstructed ($\sim$ 54 fb^{-1} of data, the same target data sample of the analysis), and events with exactly four tracks are selected, two of them identified as muons with μID$>$ 0.5 and two of them identified as electrons with eID$>$0.5. The efficiency is measured using an external and orthogonal reference trigger: the choice was the ECL trigger line *hie*, which is fired when the total energy deposition in the barrel and part of the forward ECL calorimeter exceeds 1 GeV. The presence of two electrons in the final state make this condition easily fulfilled. Being N the number of events, the efficiency is calculated as:

$$\varepsilon(fff) = \frac{N_{fff} \quad \& \quad N_{hie}}{N_{hie}} \tag{3.11}$$

where the only underlying hypothesis is that fff and *hie* are not instrumentally correlated. The fff efficiency was studied as a function of the two lowest track momenta (third and fourth in decreasing order of p_T), in order to reduce the dependence on the process used for the study.

Nevertheless, comparing with similar evaluations performed on alternative final states, it turned out that the dependence on the process was not totally removed. Therefore, the fff signal efficiency evaluation has been based on another analysis result ($e^+e^- \to \mu^+\mu^- Z'$, $Z' \to \tau^+\tau^-$), which uses a more exhaustive method. Different topologies are taken into account, depending on the number of tracks in the barrel CDC:

- number of tracks in the barrel > 3 (4 in this case);
- number of tracks in the barrel $= 3$;
- number of tracks in the barrel $= 2$;
- number of tracks in the barrel < 2
  (the case with a number of tracks in the barrel $= 0$ is negligible),

where a track is considered in the barrel if its polar angle θ is $51° < \theta < 117°$. In each of these cases, the efficiency is computed as a function of the two smallest transverse momenta among the 4 tracks. Various final states are used: $\mu\mu$ee, $\mu\mu eX$, $\pi\pi$ee, $\pi\pi$eX, where X is any particle. The average efficiency over these final states was assumed. The fff trigger efficiency is shown in Figure 3.23 as a function of the Z' mass.

Finally, on event by event basis, the fff trigger efficiency was combined with the CDCKLM one with a logical OR. This number is interpreted as a probability and used as an event weight for MC. In data, it is simply required the OR of the CDC fff trigger bit with the CDCKLM lines. The signal efficiencies of the CDCKLM trigger, fff trigger and the logic OR between them is shown in Figure 3.23, as a function of the Z' mass, after the MLP selection. While combining the trigger efficiencies event by event, the small correlation between these two triggers have been neglected, due to the fact that they are both based on tracks. It is shown elsewhere that, for 2-track events, this correlation does not play any significant role.
Using both triggers gives the system a better efficiency and a high redundancy, which in turn minimizes the systematic uncertainties due to this source.

The drop of the trigger efficiency for high masses is explained with considerations based on kinematics: the heavier the Z' the slower will be in CMS. In the extreme condition in which the Z' is at rest in CMS, it will be produced in the laboratory frame along the boost, in the z direction. The muons from the Z' decay will be preferentially emitted in the forward/backward direction and the remaining two muons will be very soft. Both CDCKLM and fff triggers are based on tracks in the barrel and are quite inefficient at low transverse momenta.

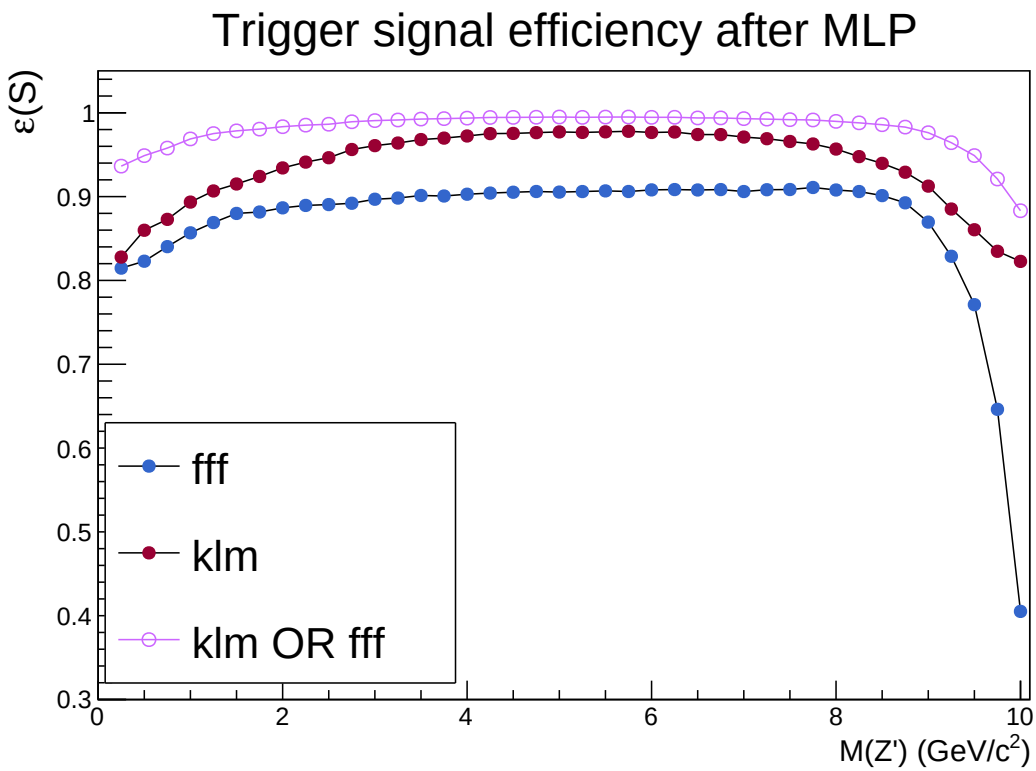

Figure 3.23: fff, CDCKLM and CDCKLM OR fff signal trigger efficiency as a function of the Z' mass, after MLP selection.

3.5 Control sample study

3.5.1 Control sample selection

A control sample was used to validate the analysis selections and to test the performances of the MLP in suppressing the background, while keeping the signal region fully inaccessible. The final choice was to use the ee$\mu\mu$ final states. A first usage of this control sample was already described in the fff trigger efficiency measurement (see section 3.4).

The same selections as for the main analysis were set on the control sample (see subsection 3.3.4), with the only difference in particle ID requirement: it was required the presence of two identified muons, with μID>0.5 or μID>0.9, and two electrons with eID>0.5. Again, one has four possible track pairs with zero net charge, but in this case they are not perfectly equivalent: $\mu\mu$, ee, eμ+μe .

Two main physics processes contribute to ee$\mu\mu$ final states: they are the SM ee$\mu\mu$ process and the $\mu\mu(\gamma)$ process, mainly through photon conversions. Many other processes also contribute: they are all indicated in the figures of this section. Contributions are also expected from processes that are not included here, particularly those with hadronic resonances, especially in the low mass region, not simulated in the generators used. Other processes, as $\pi\pi\mu\mu$, are fully absent from this study, because no generator is available in Belle II.

The SM ee$\mu\mu$ process is generated with `AAFH`, which does not contain ISR and FSR: therefore severe discrepancies are expected between data and MC due to this reason, even larger than in the 4μ case, because the presence of electrons implies important FSR contributions. These effects reduce the effective center-of-mass energy of the collision and, when studying the 4-track ee$\mu\mu$ invariant mass distribution, take events away from $\sqrt{s}$, decreasing the contribution under the peak and increasing below the peak. Comparison of data and MC event rates will suffer from these effects. Nevertheless, specifically for studies focused on the MLP effects, discrepancies are expected to be reduced when comparing relative selection efficiencies. The most important results obtained from this control sample study is about the MLP relative efficiency, the ratio of events before and after the MLP selection.

3.5.2 Data MC comparison

Invariant mass distributions before and after the MLP selection and at MLP relative efficiencies have been investigated. In order to get information as complete as possible, the agreement was cheched not only in the ee$\mu\mu$ invariant mass distribution, but also in all the possible track pairs with zero net charge, namely: $\mu\mu$, ee, eμ+μe, and for the total of any possible pair combination ee+$\mu\mu$+eμ+μe. Results have been produced in two cases, corresponding to the two muon identification criteria μID>0.5 and μID>0.9, although only the latter is presented here, since it gives slightly better results in terms of overall sensitivity (see subsection 3.3.2). The trigger efficiency is always applied to correctly weight the MC predictions, while trigger bits are selected for data.

To make a reliable comparison between data and MC it is preferable to look at them in conditions where they are actually comparable. To achieve that, two further cuts to the basic selections have been applied.

The first cut is on the dimuon invariant mass:

$$M(\mu\mu) > 500 \text{ MeV}/c^2.$$

This is applied due to to a technical simulation problem: a cut $M(\mu\mu) > 500$ MeV/c^2 is applied at `AAFH` generator level for the SM ee$\mu\mu$ process. In the low mass region, anyway, hadronic contributions are expected from final states $ee\rho \to ee\pi\pi$ with π mis-identification into μ, not included in the generator of the ee$\pi\pi$ process. To check this hypothesis, an alternative control sample has been prepared, selecting ee$\pi\pi$ events with the same selections as for the ee$\mu\mu$ control sample, but replacing identified muons with identified pions, with πID> 0.5. The invariant mass of the $\pi\pi$ pair in the ee$\pi\pi$ sample is shown in Figure 3.24. Here the ρ contribution in the data is easily visible (around $M(\pi\pi)\sim 0.77$ GeV/c^2), while this is missing in the MC sample.

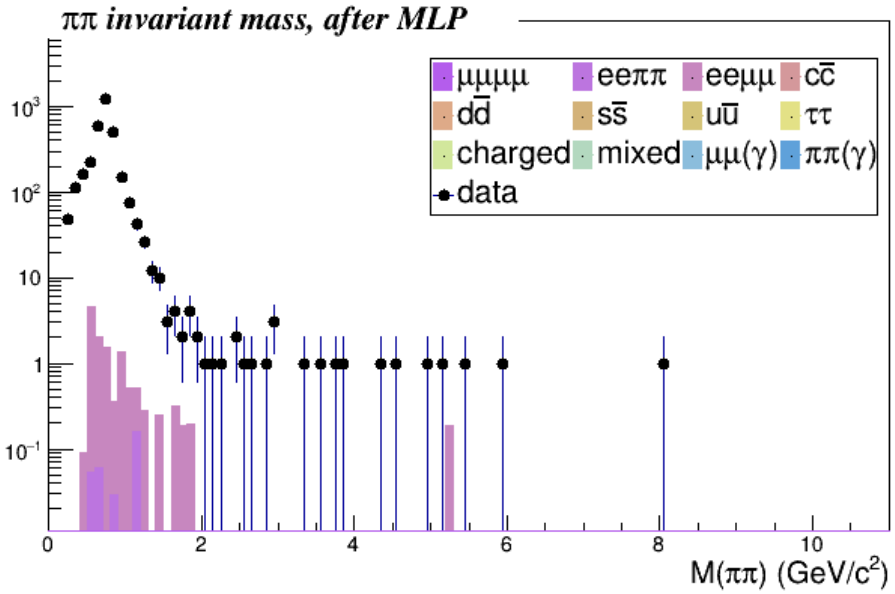

Figure 3.24: $\pi^+\pi^-$ invariant mass distribution for the ee$\pi\pi$ control sample. The lack of the ρ contribution in the MC simulation ($M(\pi^+\pi^-)$ around 0.77 GeV/c^2) is overwhelming.

The second cut is on the mass of the electron pair:

$$M(ee) > 2 \text{ GeV}/c^2,$$

and was applied to get rid of low mass discrepancies specifically due to the presence of electrons and therefore uninteresting in view of an interpretation of these results targeted on 4μ final states.

The ee$\mu\mu$ invariant mass distribution before the MLP selection is shown in Figure 3.25. The histogram on the top is the invariant mass distribution for data and MC, containing all the processes concurring to the ee$\mu\mu$ final state. After the selection actually only the SM ee$\mu\mu$ process contributes. In this figure and in the following, the plot on the bottom is the bin-by-bin ratio between data and MC yields. A constant fit has been performed on this ratio to quantify the agreement. The observed discrepancy is in agreement with the model expectation, with data above MC for invariant masses below the collision energy, and data well below MC otherwise, due to the lack of ISR and FSR processes in the generator.

In Figure 3.26 the same distributions are shown after the MLP selection. Here, the 4-track invariant mass is represented for those events in which at least one of the

four possible 2-track candidates pass the MLP selection. Results for the four mass intervals, corresponding to the four different MLP ranges of application, are presented separately. The discrepancies are similar to the previous case, for the same reasons. The strong excess of MC events in the extreme right tail of the distributions, where data are almost absent, can be also interpreted as due to the lack ISR and FSR in the generator, with the additional feature that MLPs are not trained to fully manage that situation. As anticipated, a better agreement is expected in the MLP relative efficiencies These are shown in Figure 3.27 as a function of the ee$\mu\mu$ invariant mass for the different MLP ranges. The fitted p_0 values actually confirm the expectations. It is also noticeable from the plots of Figure 3.27 that data and MC agreement is consistently better in a restricted region around the $\Upsilon(4S)$, where M(ee$\mu\mu$) = 10.58 GeV/c^2. This is easily understood by the fact that there is much less space available for ISR and FSR in that region and the kinematic features of data and MC are much closer. With the only goal of checking the discrepancies in conditions where data and MC are more comparable, the following cut was set: 10.54 GeV/c^2 $< M(ee\mu\mu) <$ 10.62 GeV/c^2. The MLP relative efficiency distributions for data and MC after this last cut is applied are shown in Figure 3.28. A sensible improvement is achieved, with discrepancies below 10 %.

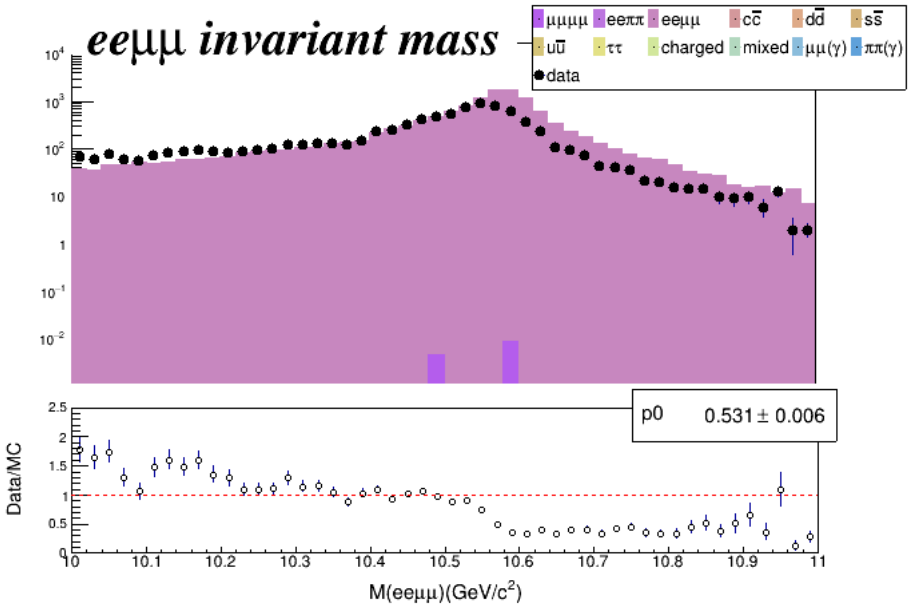

Figure 3.25: ee$\mu\mu$ invariant mass distribution and data/MC ratio, before MLP.

Object of these studies are also data/MC and MLP efficiency ratios as a function of the invariant mass of all the possible track pair combinations. Distributions before the MLP selections are shown in Figure 3.29a (all the possible combinations) and Figures 3.29b, 3.29c and 3.29d for the single pairs. Distributions after the MLP selections are shown in Figure 3.30.

Finally, here the data/MC MLP relative efficiency ratios are presented, for all the possible the track pair combinations in ee$\mu\mu$ in Figures 3.31, 3.32, 3.33 and 3.34, where

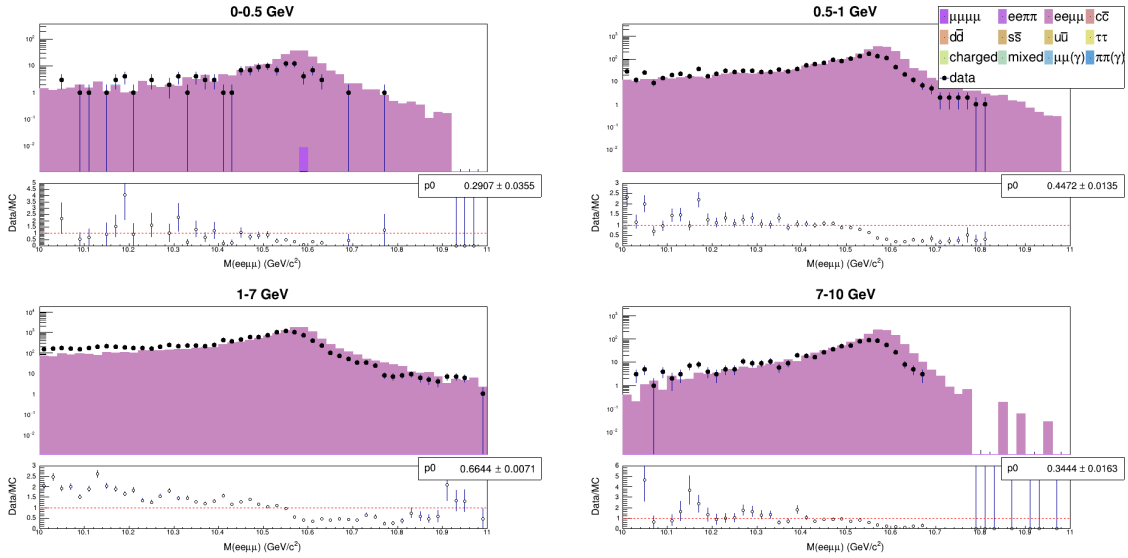

Figure 3.26: ee$\mu\mu$ invariant mass distribution and data/MC ratio, after MLP application in the four MLP mass ranges.

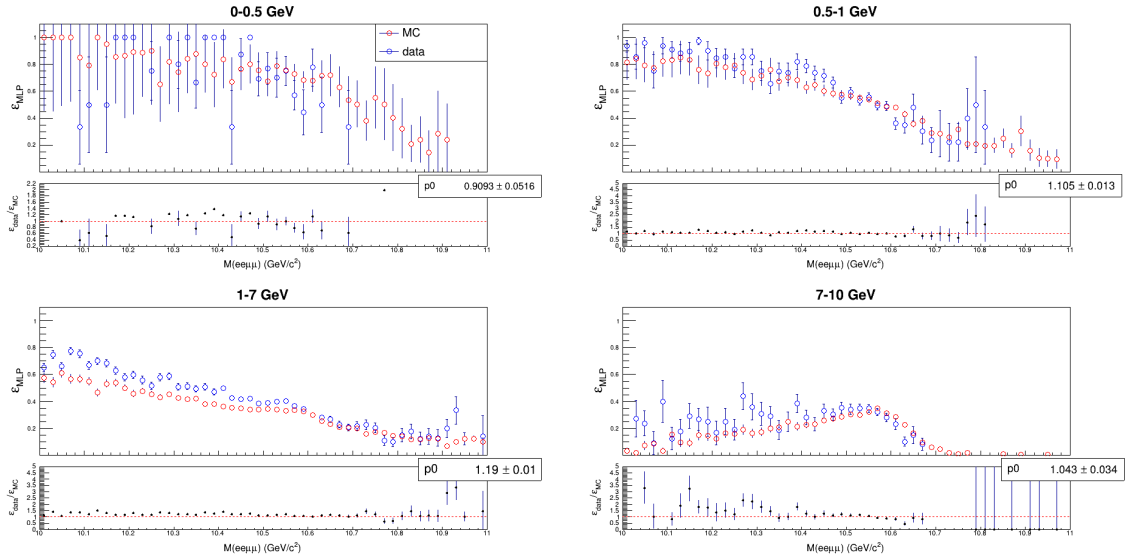

Figure 3.27: Data and MC MLP relative efficiencies and data/MC MLP relative efficiency ratios as functions of the ee$\mu\mu$ invariant mass in the four MLP mass ranges.

the ee$\mu\mu$ invariant mass was restricted to be around the $\Upsilon(4S)$ mass, between 10.54 GeV/c^2 and 10.62 GeV/c^2.

These last plots are very important and demonstrate that the effect of the MLP selection on the background is well reproduced in MC, at the level of 10%, in conditions in which data and simulation are comparable. Although the background evaluated for the $Z' \to \mu\mu$ search is measured and fitted directly on data, these checks are highly beneficial for the study of the systematics due to the MLP selection affecting the signal, as, in that case, the ISR process is taken into account at generator level.

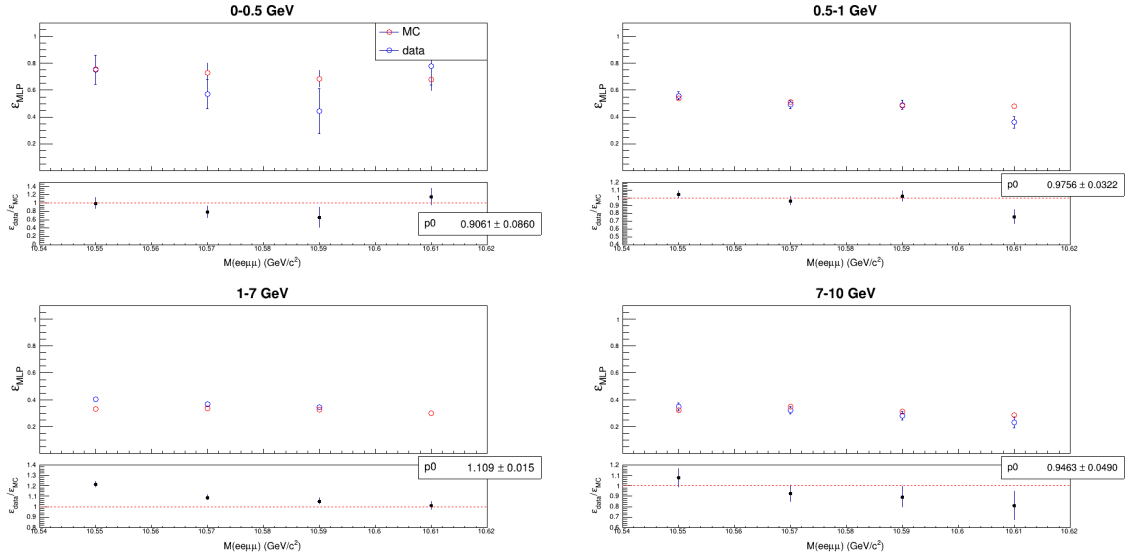

Figure 3.28: Data and MC MLP relative efficiencies and data/MC MLP relative efficiency ratios as a functions of the ee$\mu\mu$ invariant mass in the four MLP mass ranges.

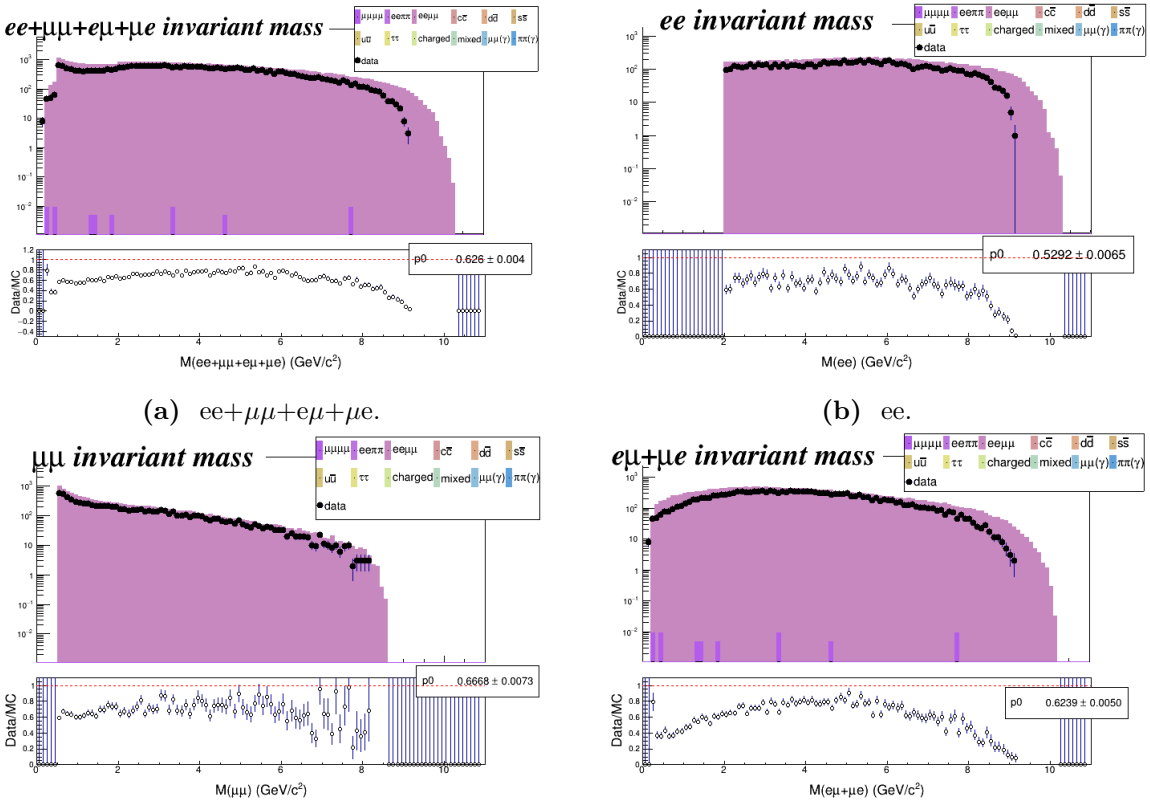

(a) ee+$\mu\mu$+eμ+μe. **(b)** ee.

(c) $\mu\mu$. **(d)** eμ+μe.

Figure 3.29: Invariant mass distributions of the total of all possible pair combinations (3.29a) and all the possible single pairs (3.29b, 3.29c and 3.29d).

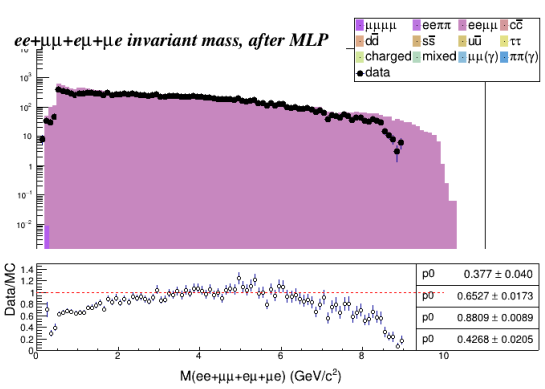

(a) ee+$\mu\mu$+eμ+μe.

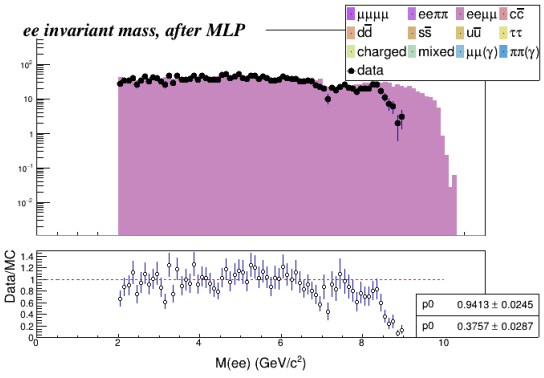

(b) ee.

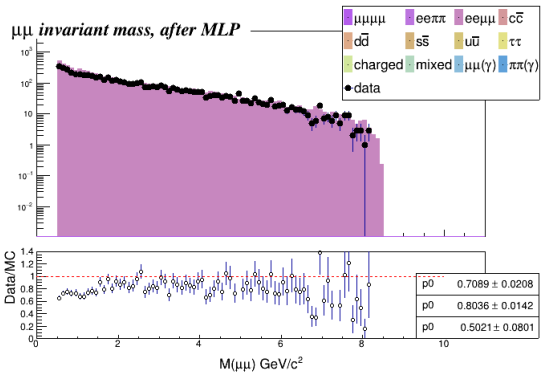

(c) $\mu\mu$

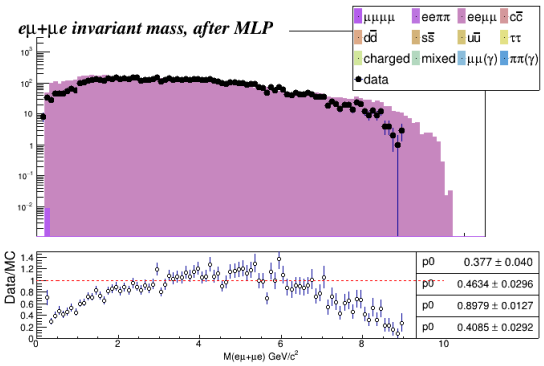

(d) eμ+μe

Figure 3.30: Invariant mass distribution of the total of all possible pair combinations (3.30a) and all the possible single pairs (3.30b, 3.30c and 3.30d), after the MLP application

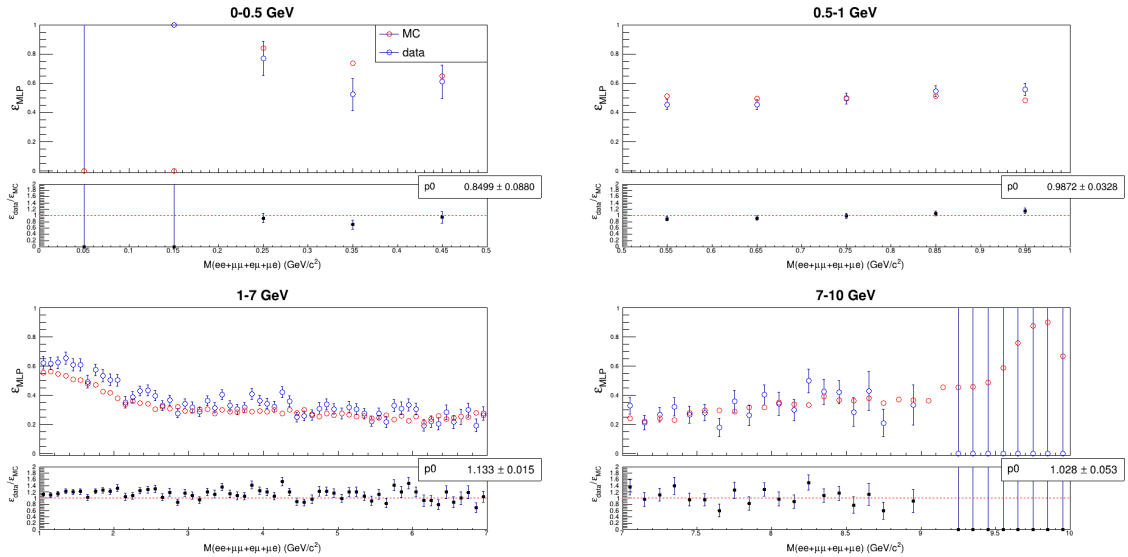

Figure 3.31: Data and MC MLP relative efficiencies and the relative efficiency ratios in the four MLP mass ranges, as a function of the invariant mass of the sum of all the possible combination pairs in ee$\mu\mu$ control sample, M(ee+$\mu\mu$+μe+eμ), for 10.54 GeV/c^2 < M(ee$\mu\mu$) < 10.62 GeV/c^2.

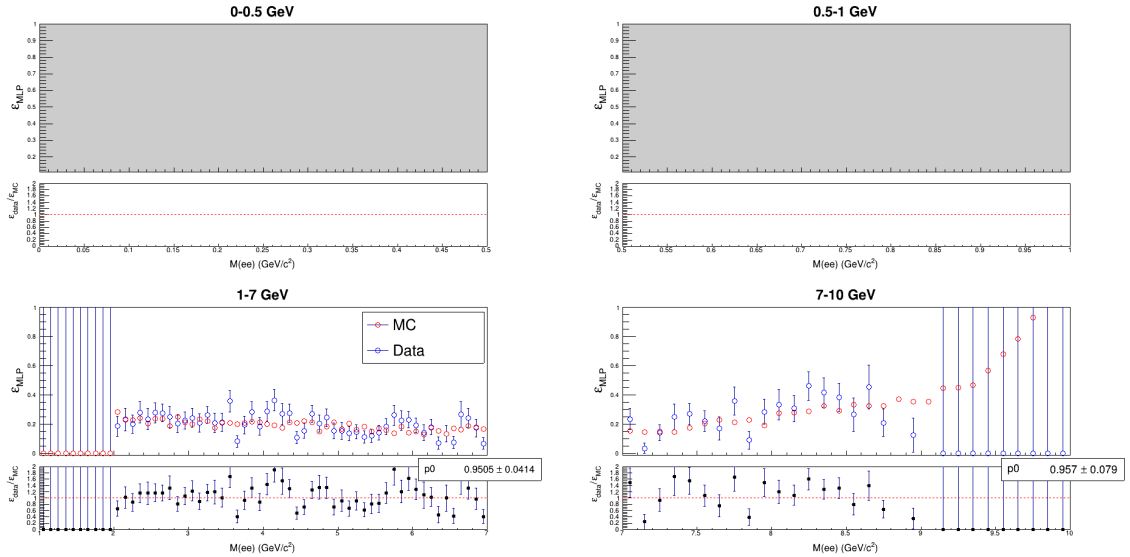

Figure 3.32: Data and MC MLP relative efficiencies and the relative efficiency ratios in the four MLP mass ranges, as a function of the ee invariant mass, M(ee), for 10.54 GeV/c^2 < M(ee$\mu\mu$) < 10.62 GeV/c^2.

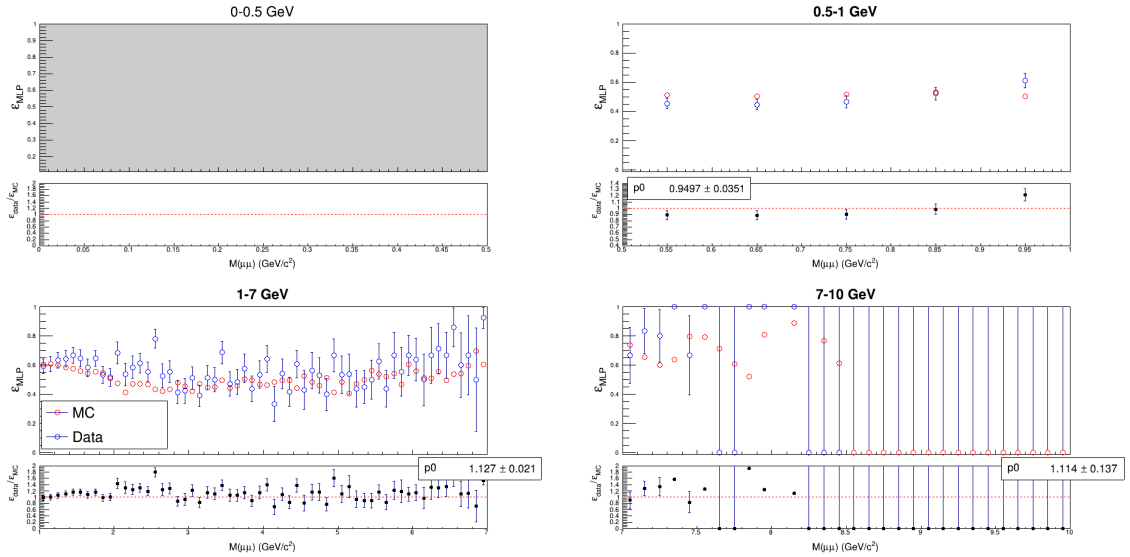

Figure 3.33: Data and MC MLP relative efficiencies and the relative efficiency ratios in the four MLP mass ranges, as a function of the $\mu\mu$ invariant mass, M($\mu\mu$), for 10.54 GeV/c^2 < M(ee$\mu\mu$) < GeV/c^2 10.62.

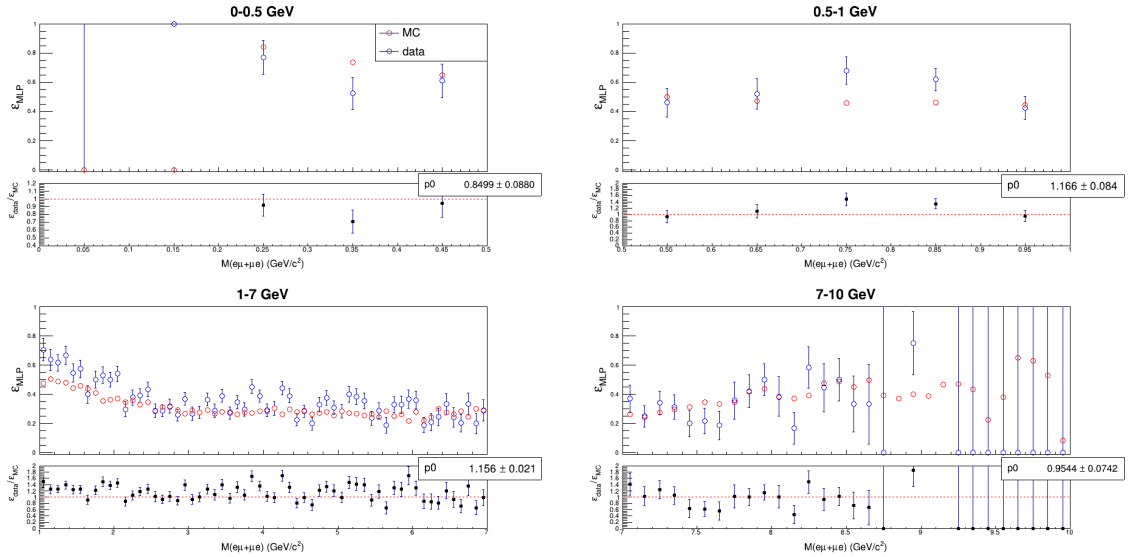

Figure 3.34: Data and MC MLP relative efficiencies and the relative efficiency ratios in the four MLP mass ranges, as a function of M(eμ), for 10.54 GeV/c^2 < M(ee$\mu\mu$) < 10.62 GeV/c^2.

3.6 Kinematic "4C" fit

Events that passed all the selections, including MLP, were subject to a kinematic fit procedure, with the goal of improving the dimuon mass resolution, which is the key parameter to improve, in turn, the analysis sensitivity.

Kinematic fitting is a technique that uses an event hypothesis, formulated in terms of kinematic constraints, to improve the measured objects of the event or to predict unmeasured ones. In addition to this, the procedure usually provides a χ^2 of the fit that can be used to test the event hypothesis on quantitative bases.

In this analysis, the so-called "4C" hard momentum constraint fit was performed, imposing that the four-momentum of the system made of the four charged tracks coincides with the initial state four-momentum, determined by the beam. This is implemented in `OrcaKinFit` [32] via the set of equations:

$$\sum_i E_i - E_{\text{beam}} = 0 \ ,$$
$$\sum_i (p_x)_i - (p_x)_{\text{beam}} = 0 \ ,$$
$$\sum_i (p_y)_i - (p_y)_{\text{beam}} = 0 \ ,$$
$$\sum_i (p_z)_i - (p_z)_{\text{beam}} = 0 \ .$$

where the index i runs over the four charged tracks. The beam four-momentum values are automatically taken by `basf2` [33] from the conditions database.

The usage of the 4C kinematic fitting is found to improve the dimuon mass resolution (see section 3.7).

3.7 Signal modeling

The signal shapes have been studied by looking at the reduced dimuon invariant mass distributions $M_{\mu\mu}$ after the 4C kinematical fit (see section 3.6). The reduced mass is defined as follows:

$$M_{\mu\mu}^{\text{reduced}} = \sqrt{M_{\mu^+\mu^-}^2 - 4m_\mu^2}. \tag{3.12}$$

The advantage of considering the reduced mass over the invariant mass is that the reduced mass distribution is smoother than the invariant mass one in the low mass region. The reduced dimuon mass distribution is fitted using the sum of two Crystal Ball (CB) functions sharing the same mean values μ. The CB function is given by:

$$f(x, \alpha, n, \mu, \sigma) = N \cdot \begin{cases} \exp(-\frac{(x-\mu)^2}{2\sigma^2}), & \text{for } \frac{x-\mu}{\sigma} > -\alpha \\ A \cdot (B - \frac{x-\mu}{\sigma})^{-n}, & \text{for } \frac{x-\mu}{\sigma} \leqslant -\alpha \end{cases} \tag{3.13}$$

where,

$$A = \left(\frac{n}{|\alpha|}\right)^n \cdot \exp\left(-\frac{|\alpha|^2}{2}\right), \tag{3.14}$$

$$B = \frac{n}{|\alpha|} - |\alpha|\,, \tag{3.15}$$

$$N = \frac{1}{\sigma(C+D)}, \tag{3.16}$$

$$C = \frac{n}{|\alpha|} \cdot \frac{1}{n-1} \cdot \exp\left(-\frac{|\alpha|^2}{2}\right), \tag{3.17}$$

$$D = \sqrt{\frac{\pi}{2}}\left(1 + \text{erf}\left(\frac{|\alpha|}{\sqrt{2}}\right)\right). \tag{3.18}$$

N is a normalization factor, while α, n, μ and σ are parameters which are fitted with the data, and erf is the error function. The signal model is therefore given by

$$f = N_1 \cdot f_1(x, \alpha_1, n_1, \mu, \sigma_1) + N_2 \cdot f_2(x, \alpha_2, n_2, \mu, \sigma_2). \tag{3.19}$$

where f_1 and f_2 are two CB functions.

An extended 1D unbinned maximum likelihood (1DUML) fit was performed for each mass hypothesis in the range of reduced mass ± 0.05 GeV/c^2 for masses below 1 GeV/c^2 (due to low mass resolution) and reduced mass ± 0.2 GeV/c^2 for masses above 1 GeV/c^2. This corresponds roughly to ranges 10-100 mass resolution wide, depending on the mass. The weighted mass resolution σ_w is given by

$$\sigma_w = \sqrt{f_{CB1} \cdot \sigma_1^2 + f_{CB2} \cdot \sigma_2^2} \tag{3.20}$$

and

$$f_{CB1} = \frac{N_1}{N_1 + N_2}, f_{CB2} = \frac{N_2}{N_1 + N_2}. \tag{3.21}$$

(see also Figure 3.35, where fits of some reduced mass distributions are shown). Trigger weights (CDCKLM OR fff) and the Belle II recommended μID corrections are applied.

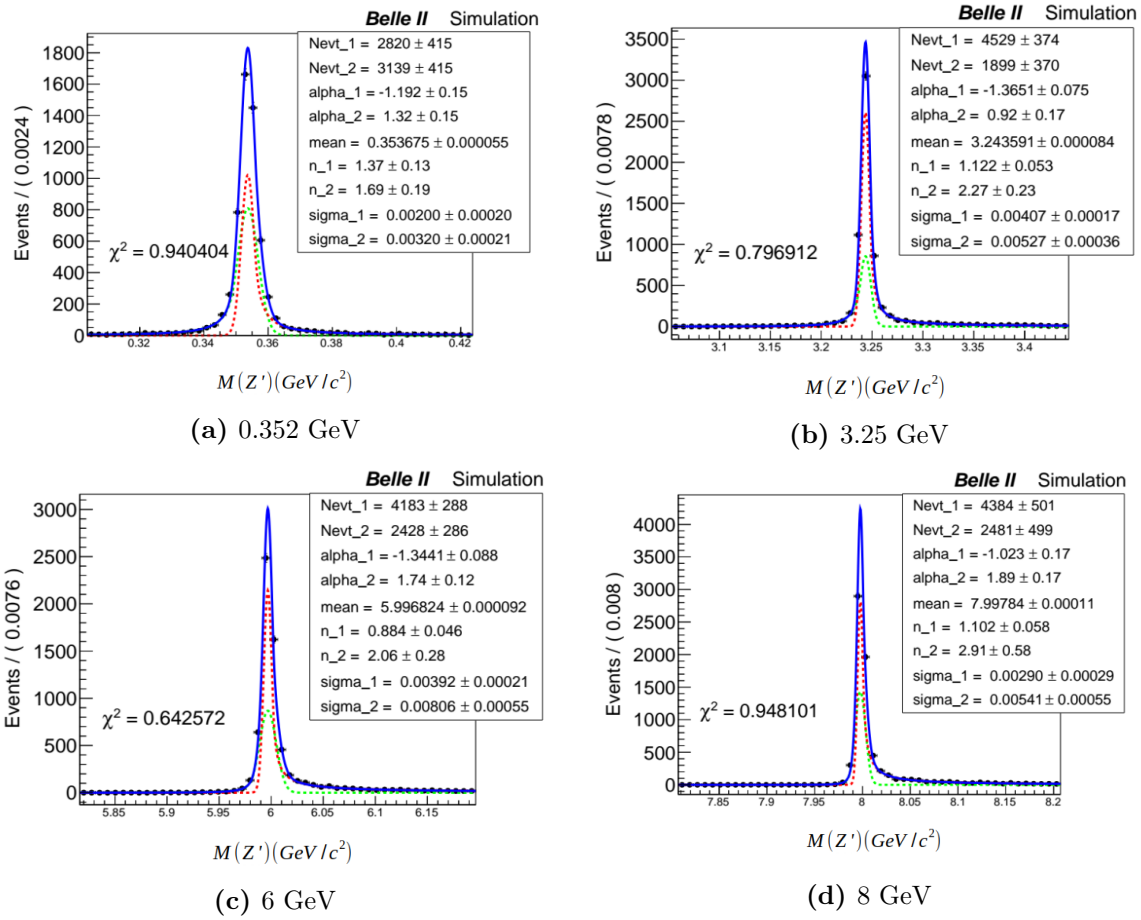

(a) 0.352 GeV **(b)** 3.25 GeV

(c) 6 GeV **(d)** 8 GeV

Figure 3.35: Examples of double Crystal fits for for 0.352 GeV/c^2 (Figure 3.35a), 3.25 GeV/c^2 (Figure 3.35b), 6.0 GeV/c^2 (Figure 3.35c) and 8.0 GeV/c^2 (Figure 3.35d) masses, respectively.

3.7.1 Signal shaping through fit to parameters

The signal shape at a specific mass is identified by seven parameters: f_{CB1}, σ_1, α_1, n_1, σ_2, α_2, n_2. In this Z' search, it was planned to use thousands of signal hypotheses: in principle it is feasible, though uncomfortable and unpractical, to perform fits for each of those hypotheses and store the parameters for later use. This procedure finally was not used, and it was opted for using analytical functions for each of the CB parameters to model their dependence as a function of the Z' mass. We fit all the CB parameters separately, in three different reduced mass regions: 0.212 GeV/c^2 - 1 GeV/c^2, 1 GeV/c^2 - 7 GeV/c^2 and 7 GeV/c^2 - 9 GeV/c^2.

Figure 3.36, Figure 3.37, Figure 3.38 show the modeling of the CB parameters for the three different mass ranges, respectively. The mass resolution, one of the most important parameters with direct consequences on the sensitivity of the Z' search, ranges approximately between 2 and 5.5 MeV/c^2. Figure 3.39 shows the distribution of the reduced mass as a function of the Z' mass.

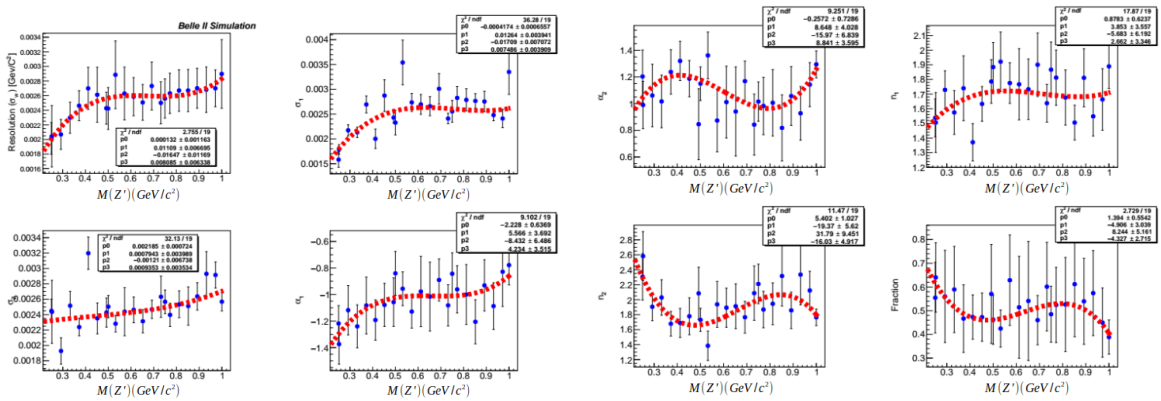

Figure 3.36: Modeling of double CB parameters for 0.212 GeV/c^2 - 1 GeV/c^2 mass interval.

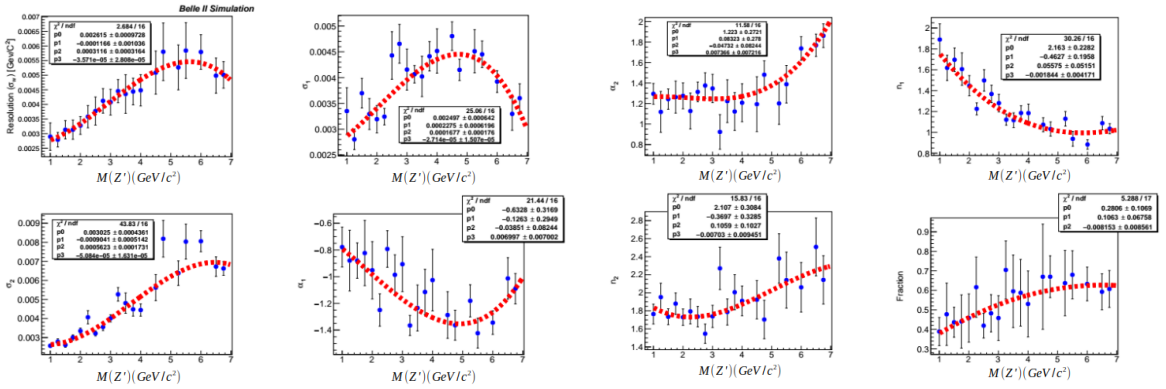

Figure 3.37: Modeling of double CB parameters for 1 GeV/c^2 - 7 GeV/c^2 mass interval.

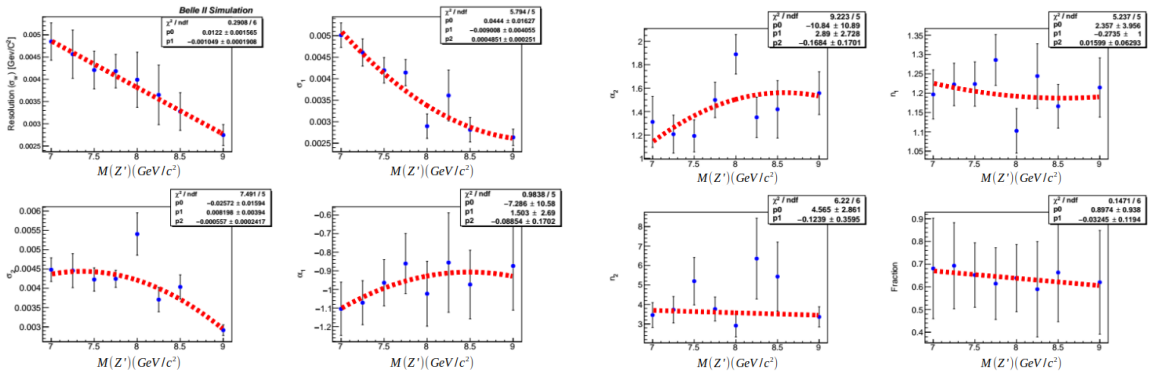

Figure 3.38: Modeling of CB parameters for 7 GeV/c^2 - 9 GeV/c^2 mass interval.

Table 3.3 collects the information about the continuous analytic functions found for the different mass ranges.

The signal efficiency is defined as the ratio of the fitted number of events after all analysis selections are applied divided by the number of total generated events, which is 20000 for all the mass points. The trigger condition CDCKLM OR fff is always included. Figure 3.40 shows the signal efficiency for μID$>$ 0.5, compared to the case in which only the $\pm 3\sigma$ range around the nominal mass is considered.

We also cross-checked the reliability of the analytical functions we got, by comparing the resolution σ_w in the polynomial modeling with the corresponding values

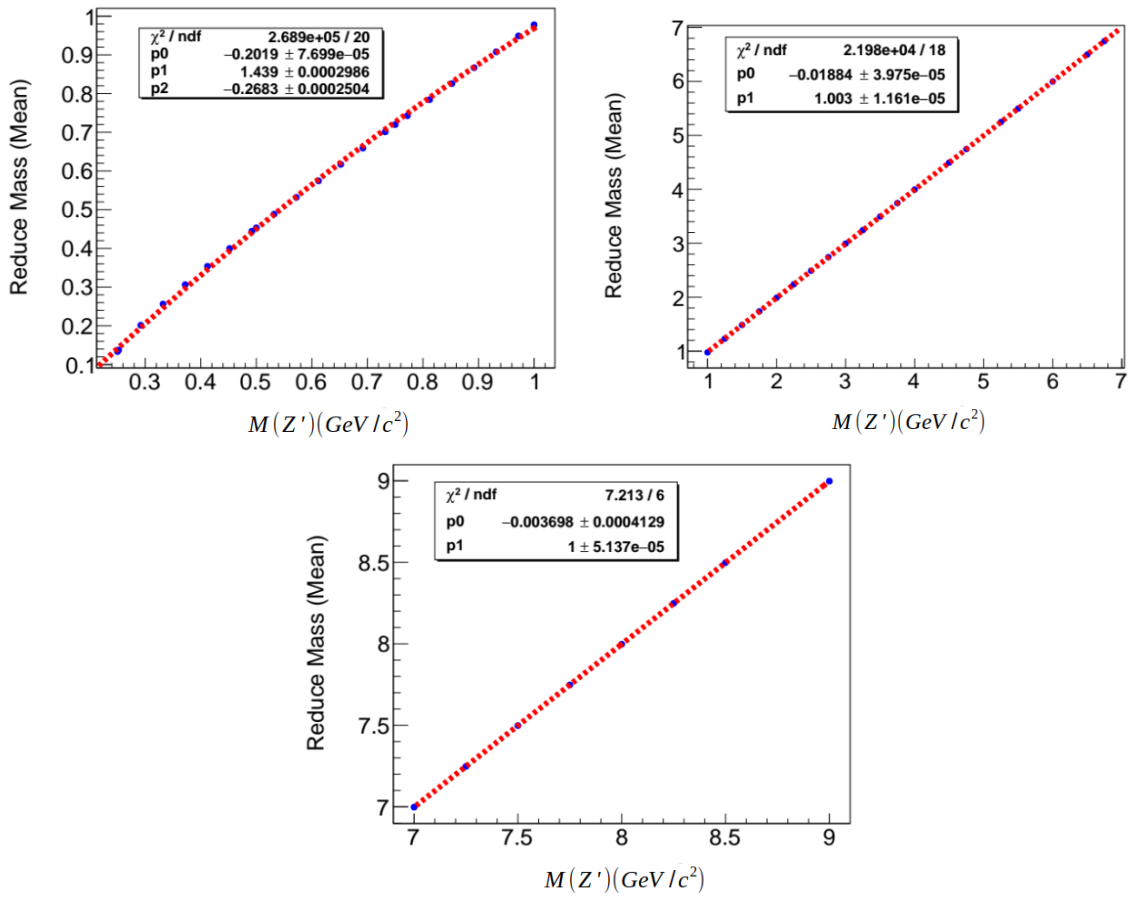

Figure 3.39: Variation of reduced mass as a function of the Z′ mass.

obtained from the double CB fits mass by mass: Figure 3.41 shows on the left side the comparison of these 3 cases and on the right side the comparison of the expected χ^2 value while fixing all the parameters to their values modeled by a polynomial function, with the value coming directly from the double CB fit with all the parameters left floating.

Table 3.3

Mass range (GeV/c^2)	polynomial
0-1	σ_w = 0.000132 + 0.01109x - 0.01647x^2 + 0.008085x^3 σ_1 = -0.0004174 + 0.01264x - 0.01709x^2 + 0.007486x^3 σ_2 = 0.002185 + 0.0007943x -0.00121x^2 + 0.0009353x^3 α_1 = -2.228 + 5.566x - 8.432x^2 + 4.234x^3 α_2 = -0.2572 + 8.648x -15.97x^2 + 8.841x^3 n_1 = 0.8783 + 3.853x - 5.683x^2 + 2.662x^3 n_2 = 5.402 - 19.37x + 31.79x^2 -16.03x^3 f$_{CB1}$ = 1.394 -4.906x + 8.244x^2 -4.327x^3 m$_{reduce}$ = -0.2019 +1.439x -0.2683x^2 efficiency = 0.4142 -0.4107x +0.3221x^2
1-7	σ_w = 0.002615 -0.0001166x +0.0003116x^2 -3.571e-05x^3 σ_1 = 0.002497 + 0.0002275x + 0.0001677x^2 -2.714e-05x^3 σ_2 = 0.003025 -0.0009041x +0.0005623x^2 -5.084e-05x^3 α_1 = -0.6328 -0.1263x -0.03851x^2 + 0.006997x^3 α_2 = 1.223 + 0.08323x -0.04732x^2 + 0.007366x^3 n_1 = 2.163 -0.4627x - 0.05575x^2 -0.001844x^3 n_2 = 2.107 -0.3697x + 0.1059x^2 -0.00703x^3 f$_{CB1}$ = 0.2806 + 0.1063x -0.008153x^2 m$_{reduce}$ = -0.01884 +1.003x efficiency = 0.3163 -0.001884x +0.0008341x^2
7-9	σ_w = 0.0122 -0.001049x σ_1 = 0.0444 -0.009008x + 0.0004851x^2 -2.714e-05x^3 σ_2 = -0.02572 +0.008198x -0.000557x^2 -5.084e-05x^3 α_1 = -7.286 +1.503x -0.08854x^2 α_2 = -10.84 + 2.89x -0.1684x^2 n_1 = 2.357 -0.2735x + 0.01599x^2 n_2 = 4.565 -0.1239x f$_{CB1}$ = 0.8974 -0.03245x m$_{reduce}$ = -0.003698 + x efficiency = 0.3809 -0.004745x

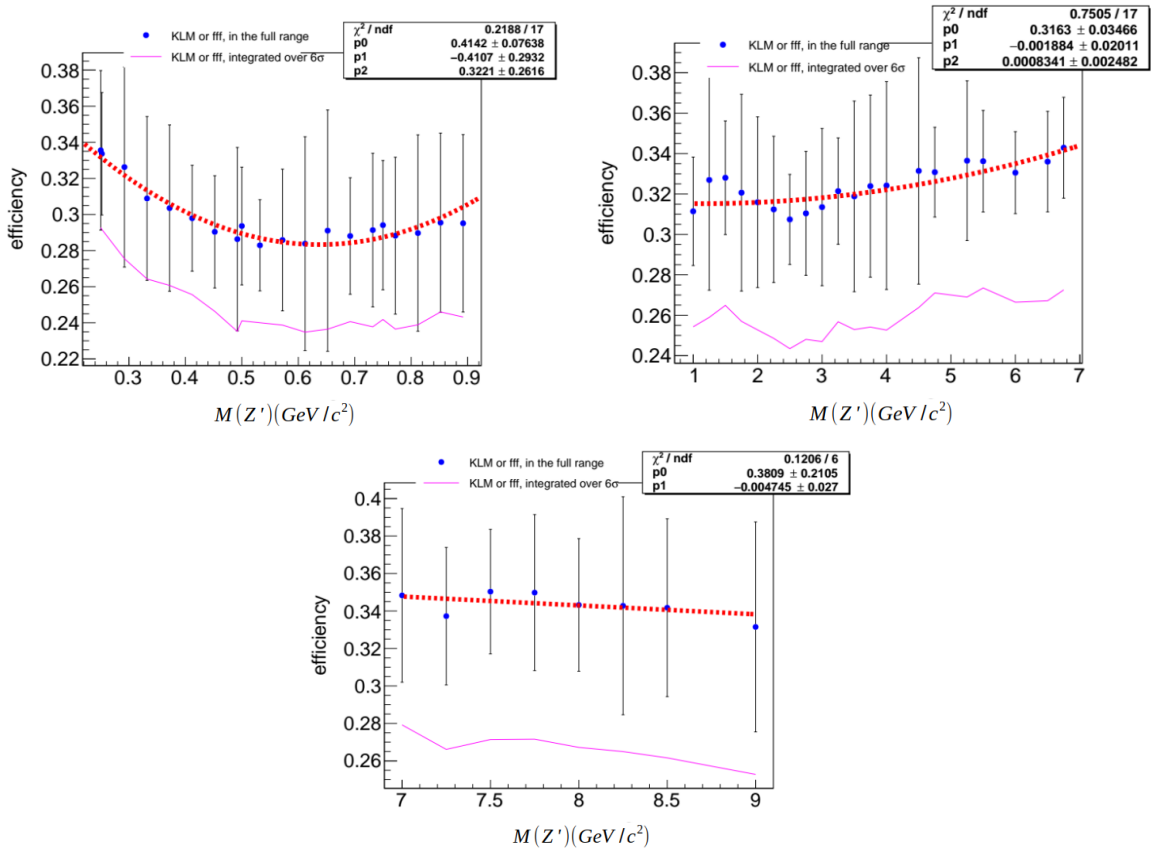

Figure 3.40: Total signal efficiency for μID$>$ 0.5. The fitted analytic function is given in Table 3.3.

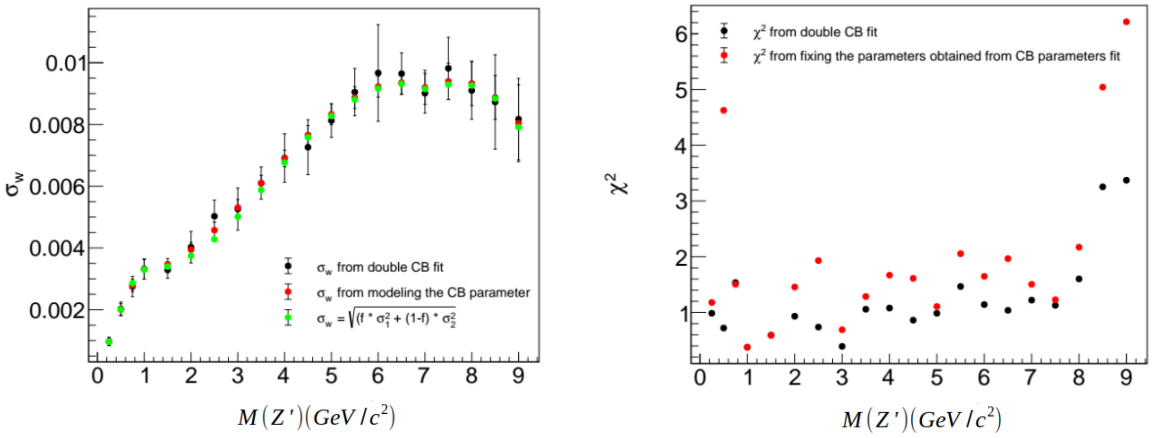

Figure 3.41: Comparison of σ_w (left) and χ^2 (right)

3.8 Fit procedure

Two target integrated luminosities are considered: $\int$ L dt = 54 fb^{-1}, on which all the studies in this work are based, and $\int$ L dt = 200 fb^{-1}, corresponding to a realistic update of the search, more competitive with the established results of *BABAR* and Belle. The background sources contributing to our Z' search are shown in figure 3.42 for $\int$ L dt = 54 fb^{-1} and 200 fb^{-1}.

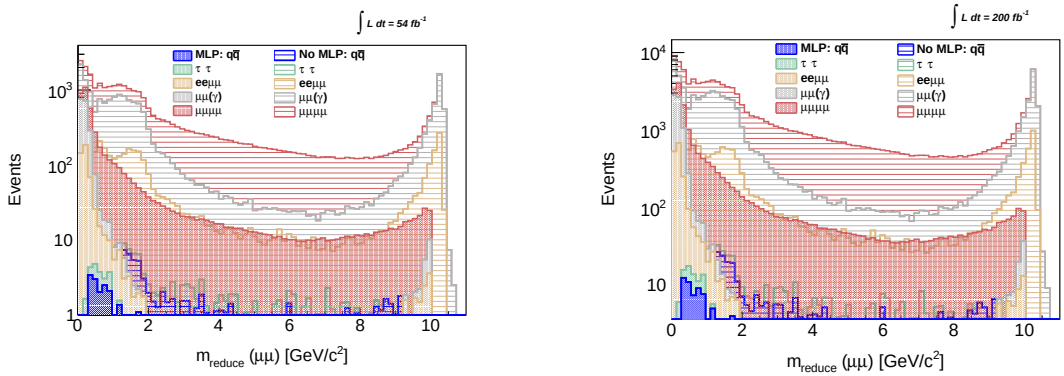

(a) 54 fb^{-1} **(b)** 200 fb^{-1}

Figure 3.42: Background events as a function of the dimuon reduced mass before MLP (dashed lines) and after MLP selection (solid lines), $\int$ L dt = 54 fb^{-1} (Figure 3.42a) and 200 fb^{-1} (Figure 3.42b)

RooFit package included in **root v6-21** was employed.
The fitting procedure is organized as follows:

- intervals of $\pm 30\sigma_w$ are selected;
- a parametrization of the background is performed employing first order Chebychev polynomials. Using a low order polynomial turns out to provide an accurate description through the full mass range, because the mass resolution σ_w is small and so are the fit intervals. Attempts to use lower or higher order polynomials resulted in final degraded sensitivities;
- the signal shapes is parametrized using the double CB functions with parameters taken from the analytical modeling and kept fixed to those values;
- the MC background distributions are fitted with a 1D Unbinned Maximum Likelihood technique, using two hypotheses: a) background-only hypothesis; b) signal + background hypothesis.

For the background-only hypothesis, the model is

$$f^{bkg}(M) = N_{bkg} \cdot (1 + a_1 \cdot M) \tag{3.22}$$

while, for the signal + background hypothesis

$$f^{sig+bkg}(M) = N_{sig} \cdot (CB_1 + CB_2) + N_{bkg} \cdot (1 + a_1 \cdot M), \tag{3.23}$$

is used, being M the reduced dimuon mass. The fit returns as interesting results the number of background events N_{bkg} in the background-only hypothesis, the number of signal events N_{sig} and the number of background events N_{bkg} in the signal + background hypothesis. In this latter case, negative values for N_{sig} are allowed, because this is shown to improve slightly the final sensitivity.

Figure 3.43 shows examples of the fitting procedures for mass points at 2.65 GeV/c^2, 3.65 GeV/c^2, 4.35 GeV/c^2, 5.25 GeV/c^2 and 6.15 GeV/c^2. Both hypotheses are checked.

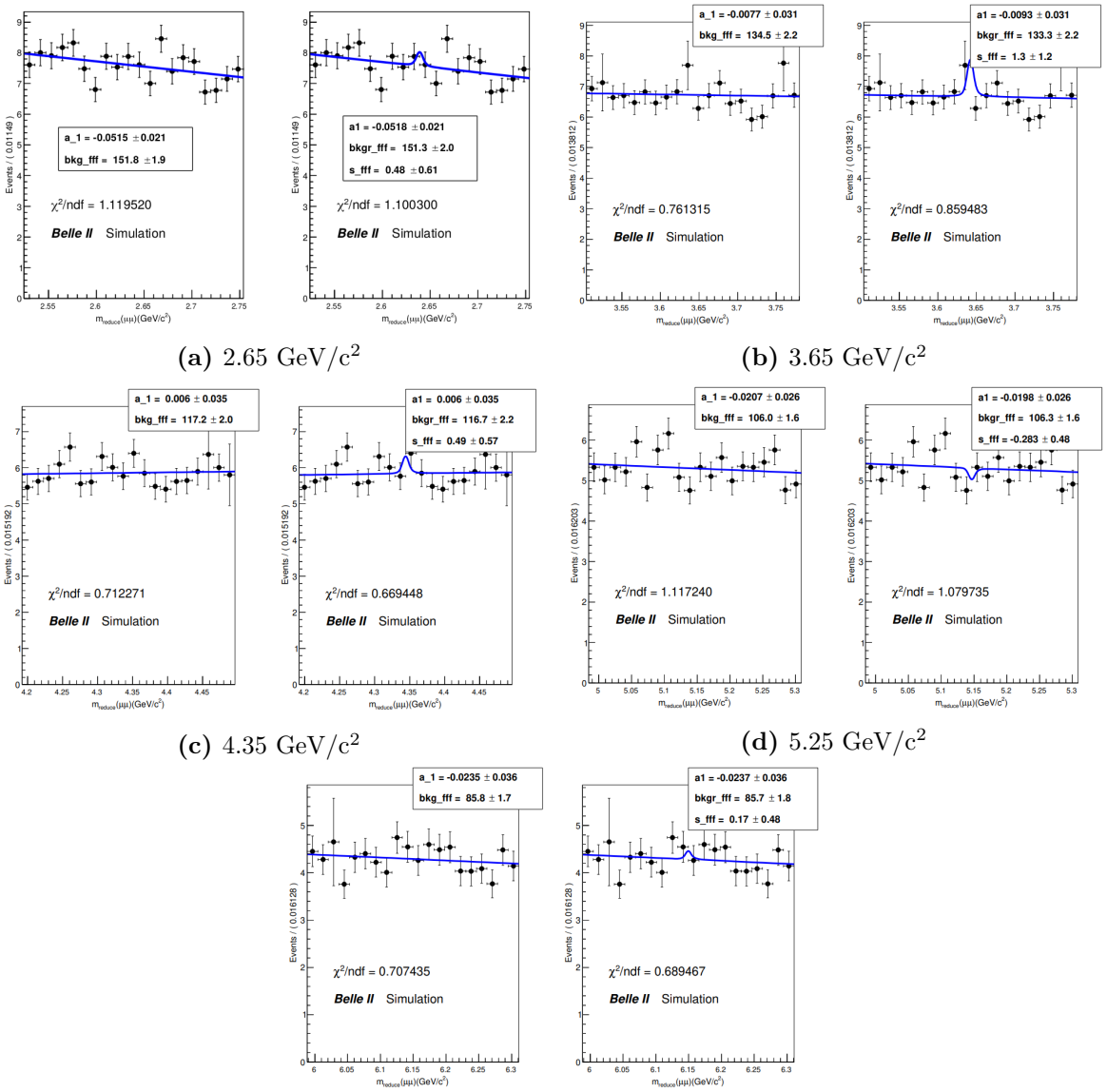

(a) 2.65 GeV/c^2 **(b)** 3.65 GeV/c^2

(c) 4.35 GeV/c^2 **(d)** 5.25 GeV/c^2

(e) 6.15 GeV/c^2

Figure 3.43: Fit results for mass points 2.65 GeV/c^2, 3.65 GeV/c^2, 4.35 GeV/c^2, 5.25 GeV/c^2, 6.15 GeV/c^2: background-only (left) and signal+background (right) hypotheses.

The procedure must be slightly changed if one wants to include the effect of systematic uncertainties in the fitting technique. The above explained model is now modified, with the number of events N_{sig} interpreted according to the well known equation

$$N_{sig} = \mathcal{L} \times \sigma \times \epsilon_{sig}, \tag{3.24}$$

where σ is the process cross section and ϵ_{sig} the signal efficiency. The signal + background model is therefore

$$f^{sig+bkg}(M) = \mathcal{L} \times \sigma \times \epsilon_{sig} \cdot (CB_1 + CB_2) + N_{bkg} \cdot (1 + a_1 \cdot M). \tag{3.25}$$

According to the approach used, systematic uncertainties affect the signal efficiency only, while the background is considered just as a result of the fit: the absolute background predictions are not reliable. In fact, it could be problematic, as the simulation

generators do not contain the important ISR contributions. Since the signal efficiency is always multiplied by the integrated luminosity (see Equation 3.25), the systematic uncertainties to the latter is technically assigned applying a Gaussian smearing whose effects then propagate on the cross section result. Quantitative estimates of the systematic uncertainties are discussed in section 3.9. The final model (PDF) used for our fits is:

$$f^{sig+bkg}(M) = G(\mathcal{L}) \times \sigma \times \epsilon_{sig} \cdot (CB_1 + CB_2) + N_{bkg} \cdot (1 + a_1 \cdot M) \tag{3.26}$$

where $G(\mathcal{L})$ is the Gaussian-smeared luminosity. The relevant fitted parameter is the process cross section σ.

The asymptotic calculator was used with a one-sided Profile likelihood test statistics to estimate 90% CL upper limits on the cross section σ_{UL}.

The corresponding 90% CL upper limit on the signal yield is

$$N_{UL}^{sig} = \mathcal{L} \times \sigma_{UL} \times \epsilon_{sig}, \tag{3.27}$$

where $\mathcal{L} =$ is the target integrated luminosity. The corresponding 90% CL upper limits in terms of the coupling constant g'^{UL} are given by

$$g'^{UL} = g'_{ref} \sqrt{\frac{\sigma^{UL}}{\sigma_{ref}}}, \tag{3.28}$$

where g'_{ref} is the reference coupling constant used in the **Madgraph** generator to compute the reference cross section (σ_{ref}).

3.9 Systematic uncertainties

Systematic uncertainties are evaluated for their effect on the signal efficiency, since the background is estimated directly from the fit and there is no need to rely on its absolute prediction. The main systematic uncertainties come from the tracking efficiency, the integrated luminosity, the trigger efficiency, the particle identification selections, the ISR cuts, the MLP selection, and the fitting procedure for the signal extraction. Other potential sources of systematic uncertainties, as those due to data and MC discrepancies in momentum resolution and beam energy shift, were found to be negligible, due to their intrinsic smallness and to the 4C kinematical fitting procedure.

3.9.1 Tracking

The tracking efficiency is taken from an existing study within the Belle II collaboration where a per track data-MC discrepancy of the efficiency is found to be 0.13 ± 0.16(stat) $\pm$ 0.89(syst)%. Since exactly 4 tracks are required, loosing even one track would cause the event to be discarded. The associated systematic uncertainty is propagated in quadrature 4 times, taking into account both statistic and systematic errors (as reported in Equation 3.29).

$$syst(\%) = \sqrt{4 \cdot (0.13^2 + 0.16^2 + 0.89^2)} \tag{3.29}$$

where also the average discrepancy is considered as a contribution to the systematic uncertainty. The final systematics is thus evaluated to be 1.80%.

3.9.2 Luminosity

The integrated luminosity has been evaluated by Belle II based on the detected number of Bhabha events and, with smaller precision, of $\gamma\gamma$ events. with a systematic uncertainty of 1%, and a negligible statistical error.

3.9.3 Trigger

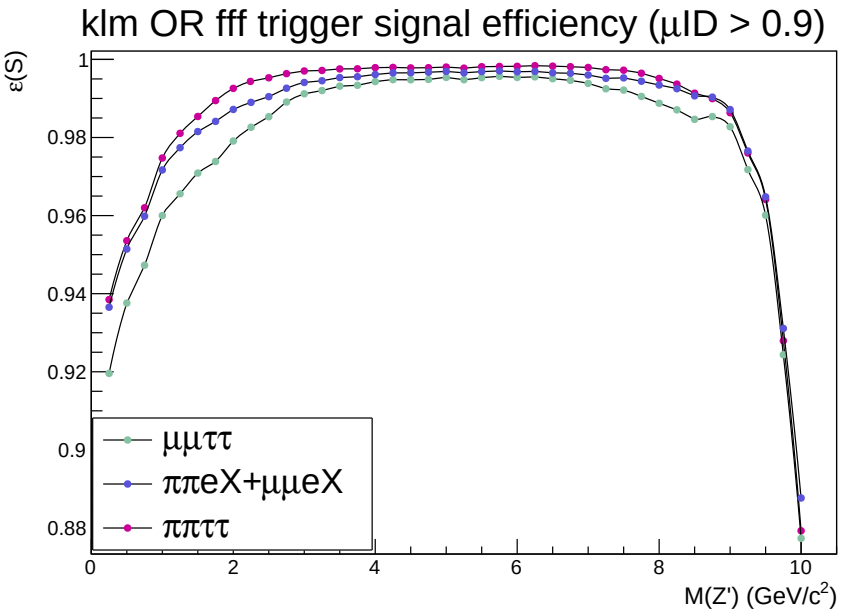

Figure 3.44: Total signal trigger efficiency (CDCKLM OR fff) as a function of the Z′ mass for different evaluations of the fff triggers. The different fff curves refer to different final states used to evaluate the efficiency.

This source of systematics was evaluated calculating the signal trigger efficiency as a function of the Z' mass for different combinations of CDCKLM and fff triggers. As mentioned in section 3.4, the fff trigger was measured in different conditions, using different final states. Figure 3.44 shows the total CDCKLM OR fff efficiency as a function of the Z' mass when fff efficiencies measured on different final states are used. The size corresponding to half of the band shown in Figure 3.44, corresponding to about 1%, is taken as the systematic uncertainty due to this source. Systematic contributions related to the CDCKLM trigger were evaluated by moving all the efficiencies in the cells shown in section 3.4 accordingly to a gaussian distribution, centred around the CDCKLM efficiency value and with a width corresponding to the quadratic sum of the systematic and statistic uncertainties. The procedure was repeated 100 times for each mass hypothesis. An example of the trigger efficiency distribution, for a Z' mass of 2750 MeV/c^2, is shown in Figure 3.45. Finally, a fit of these distributions is performed (the red line in Figure 3.45) and a systematic uncertainty is determined as a function of the Z' mass, using the fit parameters. This is shown in Figure 3.46. The case when all the CDCKLM efficiencies are completely correlated has also been taken into account, repeating the procedure by moving all the cells coherently in the same direction and by the same fractional amount.

The results for the correlated case are shown in Figure 3.47 and Figure 3.48. The evaluation of the systematic uncertainties has been done for both cases: μID > 0.5 and μID > 0.9. Results are very similar for both values of the particle ID threshold and are around $\sim 0.2 \div 0.5$ %.

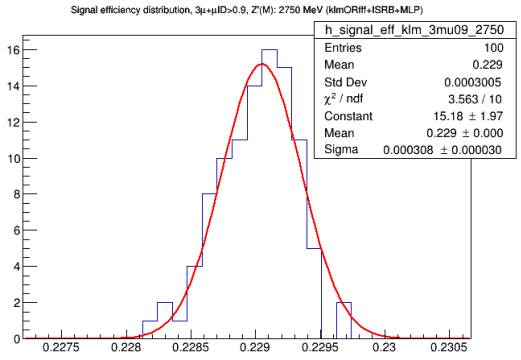

Figure 3.45: CDCKLM OR fff trigger efficiency distribution obtained by the iteration of the systematic evaluation procedure, for a Z' mass of 2750 MeV/c^2.

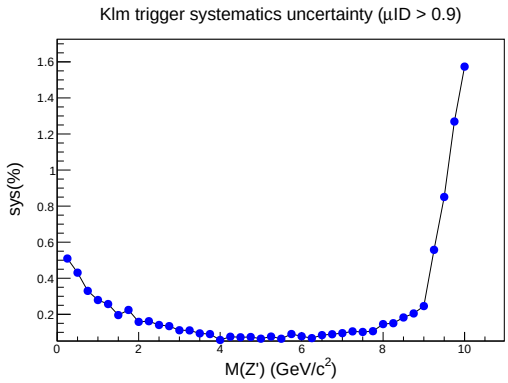

Figure 3.46: CDCKLM OR fff trigger systmatic uncertainties as a function of the Z' mass, μID > 0.9, after the MLP application.

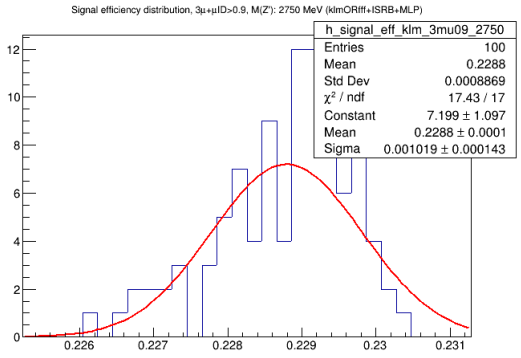

Figure 3.47: CDCKLM OR fff trigger efficiency distribution obtained by the iteration of the systematic evaluation procedure, for a Z' mass of 2750 MeV/c^2 (correlated case).

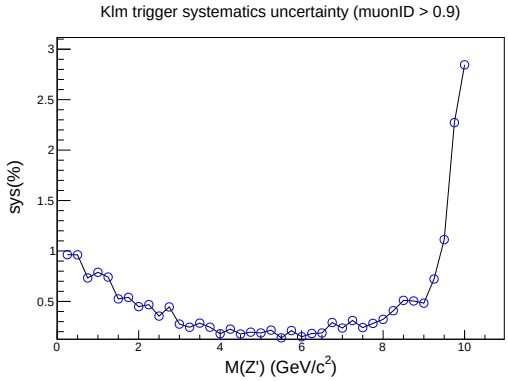

Figure 3.48: CDCKLM OR fff trigger systematic uncertainties as a function of the Z' mass, μID > 0.9, after MLP application (correlated case).

3.9.4 Particle identification

Systematic uncertainties from particle identification were evaluated by considering the official Belle II efficiency and fake rate corrections provided by the LeptonID and the HadronID working groups. Corrections are expressed as a function of the momentum p and the polar angle θ (or $cos\theta$) of the track for a specific cut on the PID variable. For each track with a given momentum and polar angle (p, θ), the PID correction and the associated statistic and systematic uncertainties are selected.

For each track the procedure is identical to the one used for the CDCKLM trigger systematics evaluation (see previous subsection, 3.9.3), with statistical and systematic uncertainties summed in quadrature. Also in this case, the systematics have been evaluated in both uncorrelated and (more conservative) correlated scenario.

Figure 3.49 and Figure 3.50 show the PID efficiency distribution and systematics in the uncorrelated case. Figure 3.51 and Figure 3.52 show the PID efficiency distribution and systematics in the correlated case.

The systematic uncertainty conservatively assumed for the PID correction is that corresponding to the correlated case, see Figure 3.52.

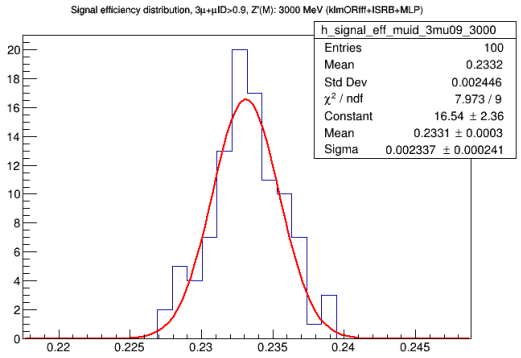

Figure 3.49: PID efficiency distribution obtained by the iteration of the systematics evaluation procedure, for a Z′ mass of 3000 MeV/c^2.

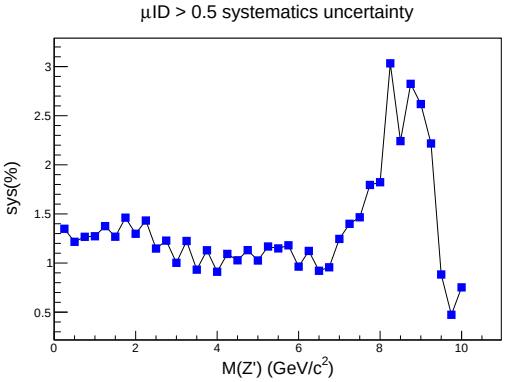

Figure 3.50: PID systematic uncertainties as a function of the Z′ mass, for μID > 0.9, after MLP application.

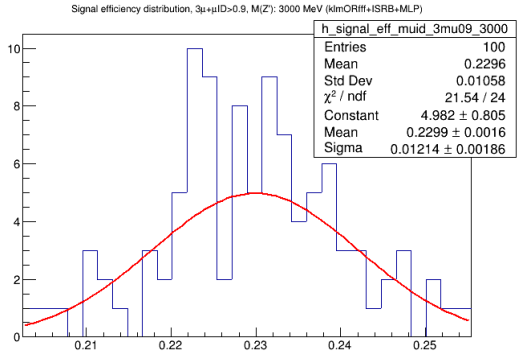

Figure 3.51: PID efficiency distribution obtained by the iteration of the systematics evaluation procedure, for a Z′ mass of 3000 MeV/c^2.

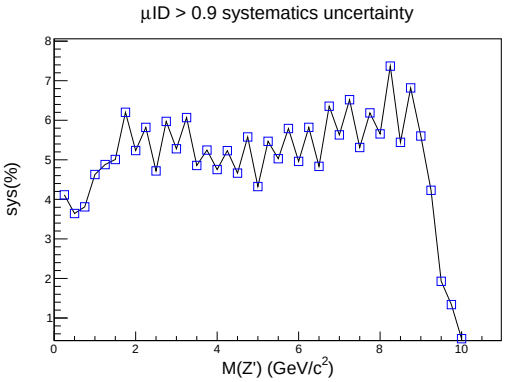

Figure 3.52: PID systematic uncertainties as a function of the Z′ mass, for μID > 0.9, after MLP application (correlated case).

3.9.5 ISR cut

Systematic uncertainties due to the ISR selections (see subsection 3.3.3) affect the signal efficiency through various effects. The signal generator includes the ISR process, but not the large-angle hard-radiation component, which can produce photons in acceptance. The signal efficiency needs to be corrected for this effect, expected to be of the order of α_{em}, at the percent level. Events can be rejected due to the presence of photons from beam backgrounds. All the samples used in this analysis, both signal and background, do contain beam background effects, which can be switched off if needed. The ISR cuts are based on the energy of clusters, for which the ECL has a finite resolution. At the energy of the selection (0.4 GeV) the ECL energy resolution is conservatively assumed to be 5%.

The effect of the lack of the hard ISR component in the signal generator has been studied using the $\mu\mu(\gamma)$ process. Events are simulated with `KKMC` and the presence of the beam background is switched off, to isolate the effect. The reconstructed events are requested to have a di-muon mass in the range 10-11 GeV/c^2, to emulate the selection applied in the $Z' \to \mu^+\mu^-$ search on the 4-track invariant mass, which intrinsically limits the maximum energy at which a photon can be radiated. In these conditions, the ISR selections rejected 2.8% of the events. This quantity, which turns out to be of the order of α_{em}, as expected, was used to correct the signal efficiency. Then the effect of changing the energy cut used in the ISRB selections (see subsection 3.3.3) by $\pm 5\%$ was checked. It turned out that, in the sample without beam background, the effect is negligible. When the beam background contribution was switched on at simulation level a variation of $\pm 0.26\%$ is obtained.

The effect of the beam background in ISR selections was checked on the signal simulation too, in a similar way. The result, as a function of the Z$'$ mass, is shown in Figure 3.53, which fully confirms, for the beam background only, what found for the $\mu\mu(\gamma)$ process.

Finally, these effects were cross checked on the ee$\mu\mu$ control sample in data, after the MLP selection. Due to the presence of electrons, FSR processes are also expected to contribute. The effect of changing by $\pm 5\%$ the energy cut in the ISRB selection (see section 3.3.3) is shown in Figure 3.54, as a function of the dimuon mass. Once again, it confirms the MC based estimates.

The largest among the effects in Figure 3.53 and 3.54 was considered, as a function of the mass, as the systematic uncertainty due to this source.

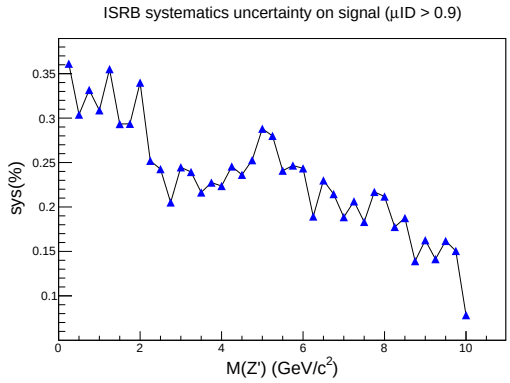

Figure 3.53: ISR cut systematic uncertainties on the signal, as a function of Z′ mass.

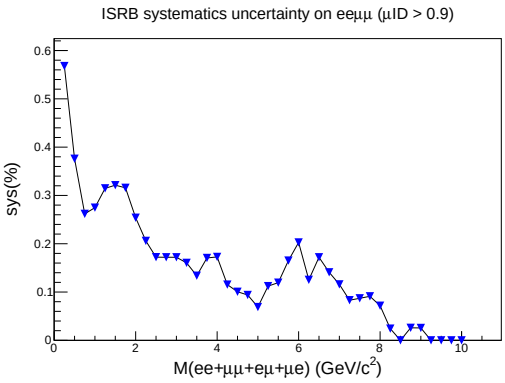

Figure 3.54: ISR cut systematic uncertainties on ee$\mu\mu$ data.

3.9.6 MLP

This is one of the hardest tasks of this search. The goal is to evaluate the systematic uncertainties affecting the signal efficiency due to the MLP selection, but all what is in data is background. The possibility of using event samples with some resonances (J/ψ, $\Upsilon(1,2,3S)$, ...) was studied, but it turned out that, because of the different production mechanism compared to signal, they are heavily suppressed by the MLP selection. Therefore this study relies on the ee$\mu\mu$ control sample, and particularly on those about data and MC comparisons of MLP relative efficiencies (see subsection 3.5.2), which are of course related to the background, and assume that the uncertainties estimated in those conditions are representative of the signal too. This is a conservative approach, in a sense, because MLPs are designed to select a good fraction of signal events and to suppress a very large amount of background, keeping small corners of the phase space, with potentially relevant uncertainties.

Table 3.4: p_0 parameters from polynomial fits on data/MC MLP relative efficiency ratios in the four MLP mass ranges.

	"ISR" cuts	μID	0-0.5 (GeV/c^2)	0.5-1 (GeV/c^2)	1-7 (GeV/c^2)	7-10 (GeV/c^2)
ee$\mu\mu$	B	0.5	0.88	0.93	1.14	0.96
		0.9	0.9	0.97	1.1	10.95
	C	0.5	0.88	0.94	1.13	0.95
		0.9	0.91	1	1.1	0.95
ee+$\mu\mu$+eμ+μe	B	0.5	0.86	0.94	1.18	1.09
		0.9	0.85	0.99	1.13	1.03
	C	0.5	0.86	0.95	1.17	1.04
		0.9	0.88	1.02	1.12	0.95
ee	B	0.5	-	-	0.98	0.99
		0.9	-	-	0.95	0.96
	C	0.5	-	-	0.99	0.85
		0.9	-	-	0.96	0.79
$\mu\mu$	B	0.5	-	0.9	1.13	1.1
		0.9	-	0.95	1.13	1.11
	C	0.5	-	0.91	1.1	1.1
		0.9	-	0.98	1.09	1.08

The results found in subsection 3.5.2 on the relative MLP efficiencies following a

restricted cut on the ee$\mu\mu$ invariant mass around the $\Upsilon(4S)$. The basic assumption is that, in this situation, data and MC are more directly comparable, because ISR and FSR effects (absent in MC) are less relevant. The further assumption is that the uncertainties found in these conditions hold in the full mass interval 10-11 GeV/c^2 and, finally, as anticipated, that they hold for the signal too. The results are summarized in Table 3.4, where also the p_0 parameters obtained with different and more restrictive ISR cuts ("ISRC", see subsection 3.3.3) and μID threshold conditions are shown.

The discrepancies found in the relative MLP efficiencies in subsection 3.5.2 and in Table 3.4 are of the order of 10%, a value which is assumed for the full mass range as the systematic uncertainty due to this source.

3.9.7 Fit

The systematic uncertainties due to the fit procedure are evaluated by changing the background modeling description and measuring the impact on the signal estimate. In particular, the PDF function used to model the background is replaced by a Chebychev polynomial of second degree, compared to the first degree used in section 3.8, while the signal description is left unchanged (sum of two CB functions). A series of signal + background fits is performed on many MC samples after all the selections, with a background statistics equivalent to that expected for the target luminosity of 54 fb^{-1}, where events are selected with a bootstrap technique. A number of signal events is also injected for each Z' mass according to a Poissonian distribution with expected value set to the 90%CL excluded yield, evaluated using a background-only sample with first order Chebychev polynomial to describe the background, without taking into account systematic effects. Fitted signal yields are compared with the true number of injected events and a pull distribution is built for each Z' mass. Pull mean values and pull widths are shown in Figure 3.55. The result shows that this procedures overestimates the signal yield by ∼8% on average: this value was assumed as a systematic uncertainty due to the fit stability.

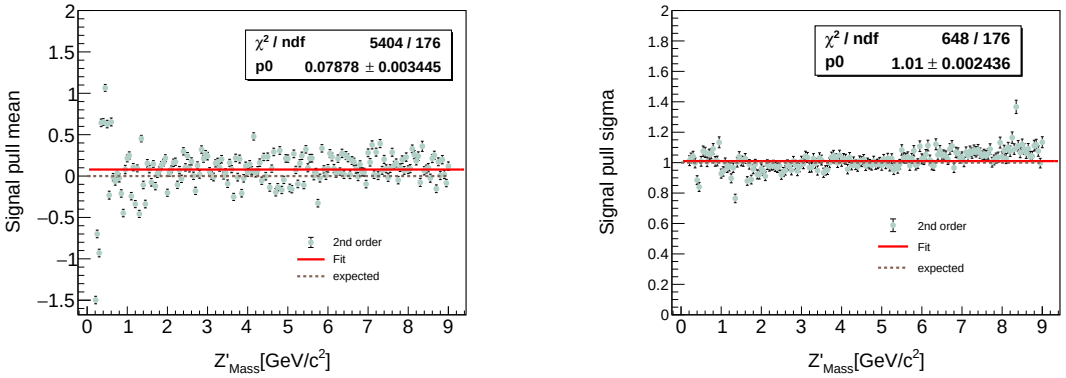

Figure 3.55: Distribution of the mean μ and width σ of the pulls for different Z' mass hypothesis.

3.9.8 Summary of systematic uncertainties

All the systematic uncertainties estimated in the previous subsections are summed in quadrature. The result is shown in Figure 3.56 as a function of the Z′ mass. The total uncertainty is quite stable and ranges from 13.2% to 14.6%. A simple interpolation of the points in Figure 3.56 allows to get a value for the systematic uncertainty on the signal efficiency at any Z′ mass.

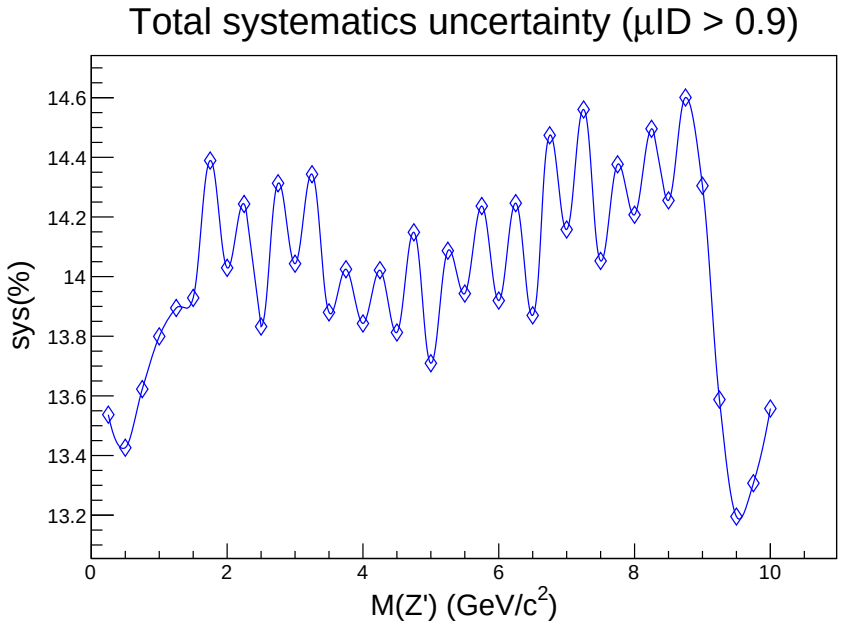

Figure 3.56: Total systematic uncertainties obtained as the quadratic sum of all the individual source contributions.

Chapter 4

Results and conclusions

4.1 Sensitivity

The fit procedures explained in section 3.8 were used to evaluate the final sensitivity of the search $e^-e^- \to \mu\mu Z'(Z' \to \mu\mu)$. Systematic uncertainties are those evaluated in section 3.9: the values shown in Figure 3.56 have been interpolated, in order to provide a systematic uncertainty on the signal efficiency for each mass point.

Figure 4.1 shows the expected 90% CL upper limits on the cross section σ_{UL} for mass points 0.7 GeV/c^2, 1.1 GeV/c^2, 1.95 GeV/c^2, 2.55 GeV/c^2 using the described procedure.

Figure 4.2 and Figure 4.3 show the upper limits on the cross section and on the signal yield mass by mass for integrated luminosities of 54 fb^{-1} and 200 fb^{-1}.

Finally, Figure 4.4 shows the expected 90% CL sensitivity for the $e^-e^- \to \mu\mu Z'(Z' \to \mu\mu)$ process for 54 fb^{-1} and 200 fb^{-1} integrated luminosities, compared with the results from *BABAR*. These plots show that the followed strategy of aggressive background suppression works very well. It is clear that, to be competitive and actually better than *BABAR* on most of the mass range, we must base this search on 200 fb^{-1}, rather than on the 54 fb^{-1} available now for this analysis.

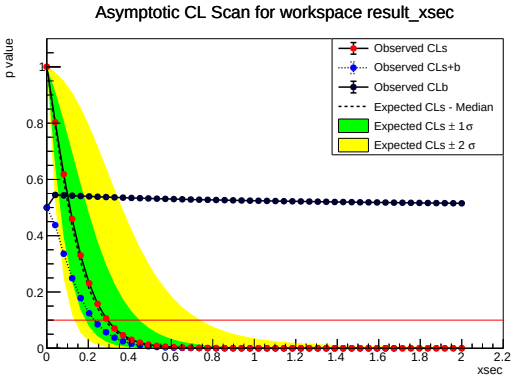

(a) 0.7 GeV/c^2

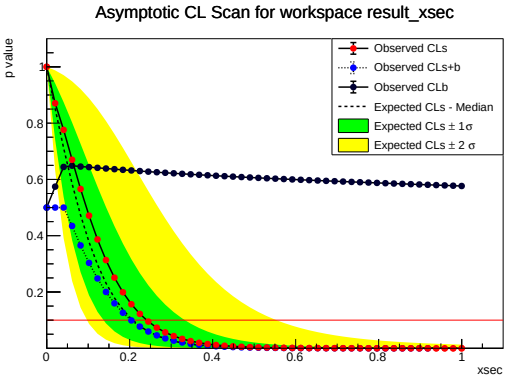

(b) 1.1 GeV/c^2

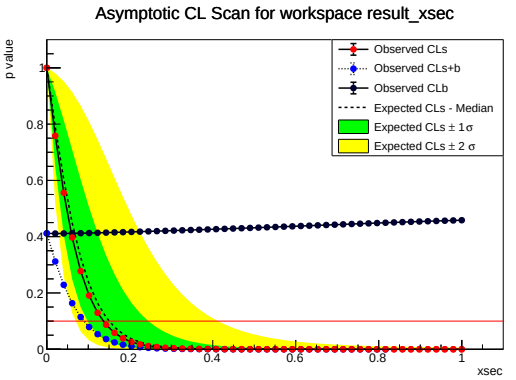

(c) 1.95 GeV/c^2

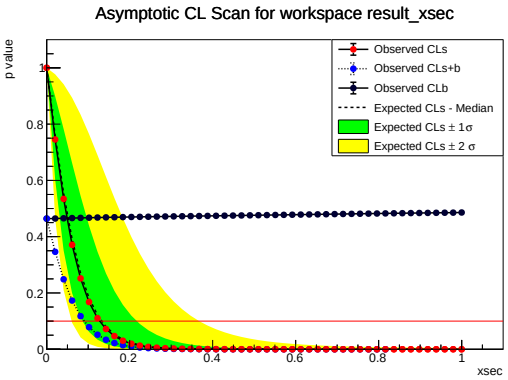

(d) 2.55 GeV/c^2

Figure 4.1: Cross section upper limit estimations (x axis) for masses of 0.7 GeV/c^2 (Figure 4.1a), 1.1 GeV/c^2 (Figure 4.1b), 1.95 GeV/c^2 (Figure 4.1c), 2.55 GeV/c^2 (Figure 4.1d). Systematic uncertainties taken into account.

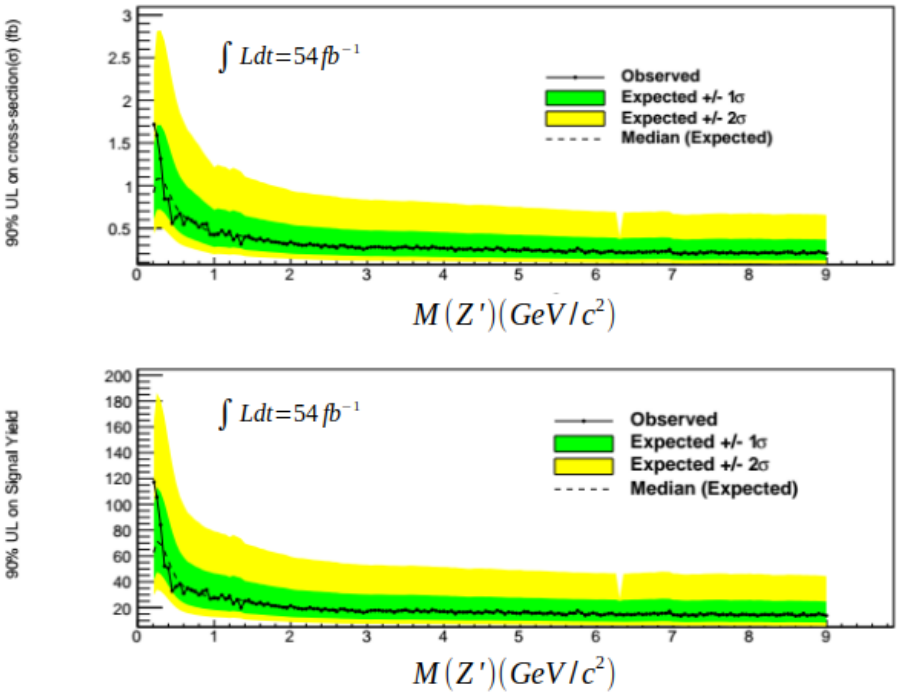

Figure 4.2: Estimated 90% CL upper limit on the cross section (top) and on the signal yield (bottom) for the process $e^-e^- \to \mu\mu Z'(Z' \to \mu\mu)$ for 54 fb^{-1} with systematic uncertainties taken into account.

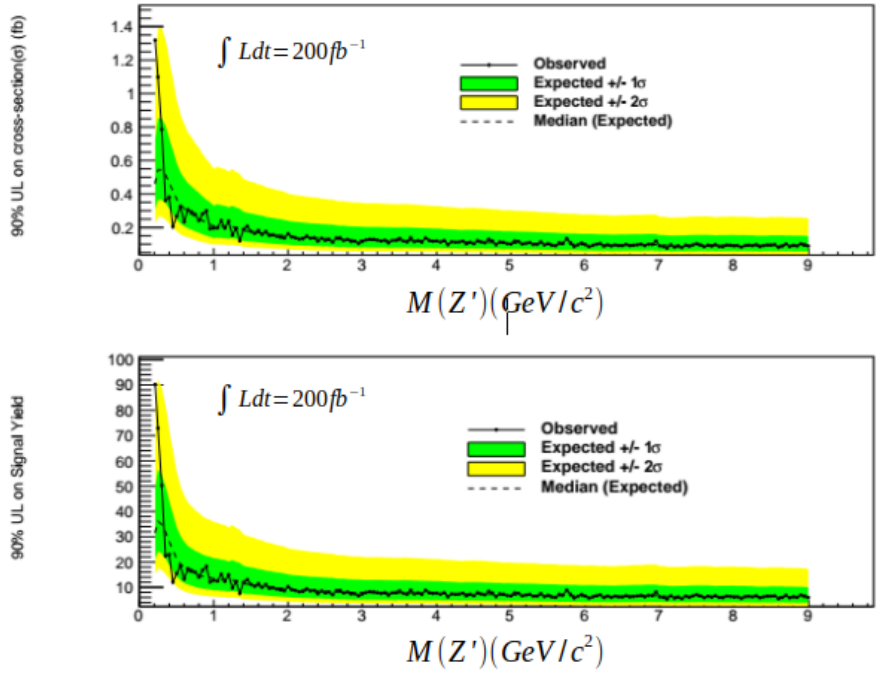

Figure 4.3: Estimated 90% CL upper limit on the cross section (top) and on the signal yield (bottom) for the process $e^-e^- \to \mu\mu Z'(Z' \to \mu\mu)$ for 200 fb^{-1} with systematic uncertainties taken into account.

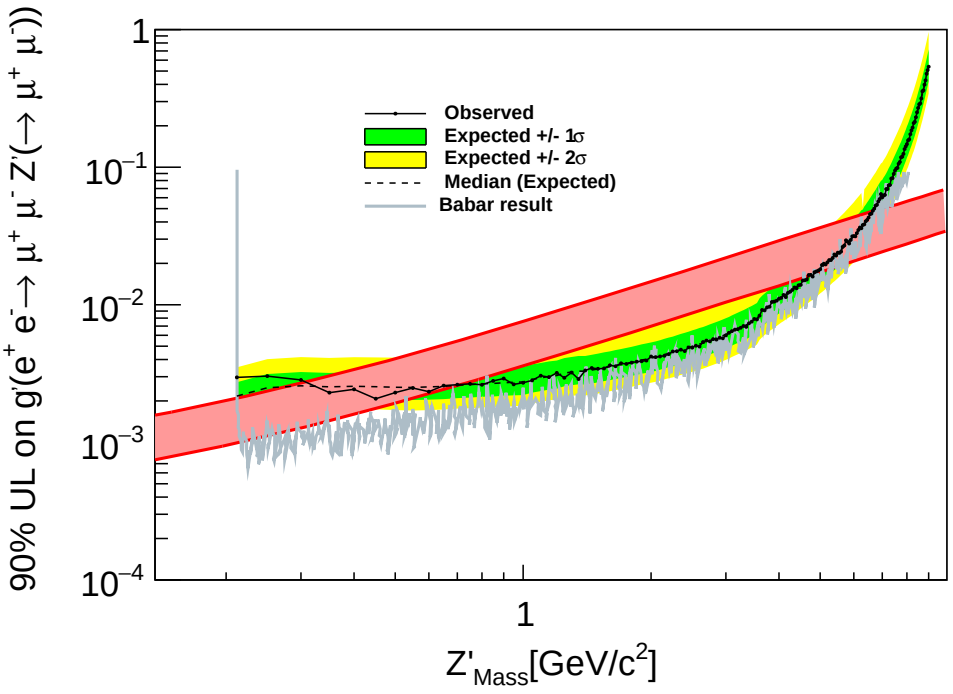

(a) 54 fb^{-1}

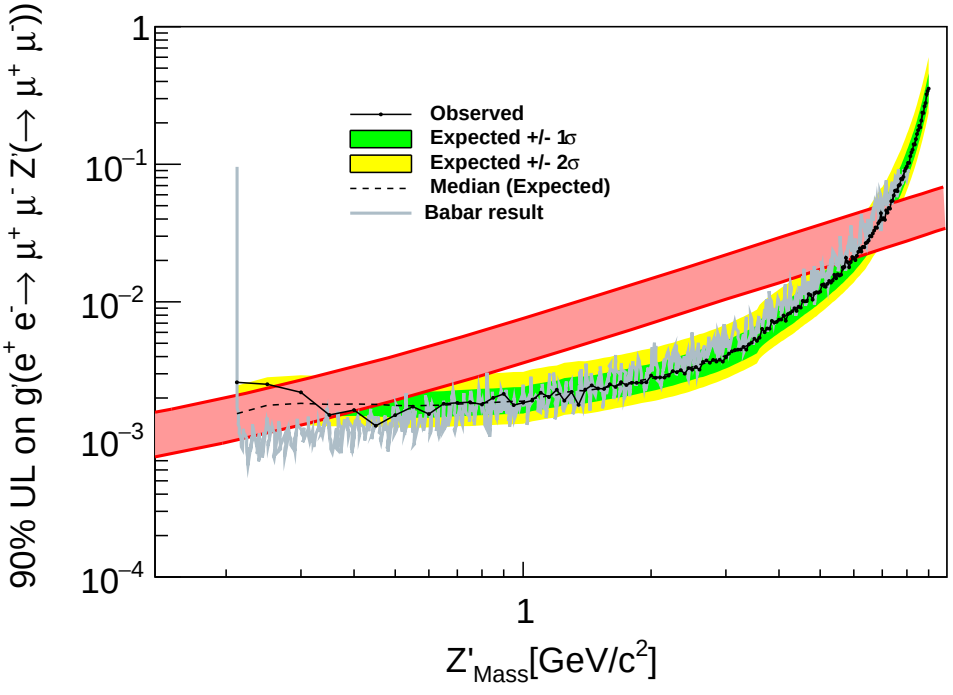

(b) 200 fb^{-1}

Figure 4.4: Estimated 90% CL sensitivity on the coupling constant g' for $e^-e^- \to \mu\mu Z'(Z' \to \mu\mu)$ for 54 fb^{-1} (Figure 4.4a) and 200 fb^{-1} (Figure 4.4b) integrated luminosity. Systematic uncertainties taken into account. Also shown is the band that would explain the observed $(g-2)_\mu$.

4.2 Results on a 10% unveiled sample

In this thesis, the work on the analysis $e^+e^- \to \mu^+\mu^- Z'(Z' \to \mu^+\mu^-)$ has been presented, where a visibly decaying Z′ boson is searched for in a 4-muon final state.

After the concluding remarks of section section 4.1, the target luminosity of this measurement, finalized to a journal publication, has been set to 200 fb^{-1}. This sample corresponds to the luminosity collected by Belle II up to the summer 2021 and is now available for data analysis. It requires some time, however, to do it in practice, as the operation involves also some technical changes: a new software release, a new Monte Carlo release, new trigger efficiencies to be evaluated (the KLM trigger conditions are different in 2021 compared to 2020, with lower thresholds). Taking all this into account, the time for a paper submission to a physics journal is planned in summer 2022, beyond the horizon of this thesis. For all these reasons, the analysis did not receive yet the Collaboration approval, postponed to the next summer.

Nevertheless, specifically for this thesis, the permission to unveil a sample corresponding to 10% of the original target luminosity of 54 fb^{-1} has been asked and obtained to the Collaboration: in the rest of this chapter, the results on 5.4 fb^{-1} in the signal region are shown. The applied selections have been extensively explained in section 3.3.

Figure 4.5 shows the data 4-track "4μ" invariant mass distribution after all the selections but the MLP: the expected MC background is superimposed, including all the concurring processes.

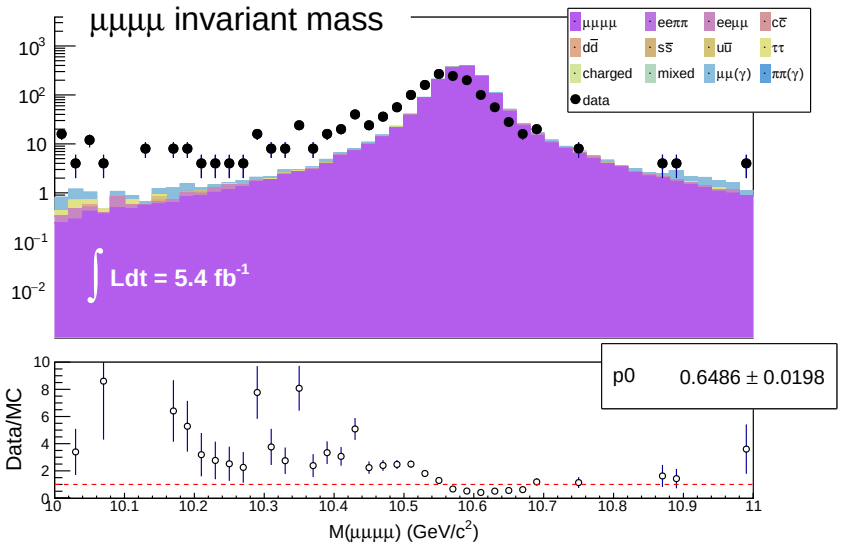

Figure 4.5: $\mu\mu\mu\mu$ invariant mass distribution for data and MC after all selections but MLP.

The bottom panel of Figure 4.5 shows the ratio $\frac{data}{MC}$ and the constant polynomial fit to evaluate the average discrepancy. We have a discrepancy of ∼35%, as expected from the lack of the ISR effects in the generator of the dominant background and from the *BABAR* and Belle experiences.

The 4μ invariant mass distribution for data and MC after the MLP selection is shown Figure 4.6. Discrepancies between data and MC are still evident in all the four MLP application ranges.

The MLP relative efficiencies for data and MC are shown in Figure 4.7, where

we restrict the total invariant mass to be strictly around the $\Upsilon(4S)$: 10.54 GeV/c^2 < M(4-tracks) < 10.62 GeV/c^2. As expected, the MLP relative efficiencies show a much better agreement than the data/MC ratios, not exceeding the 10% level, as found with the ee$\mu\mu$ control sample too. This reinforces the reliability of the systematic uncertainty estimated as due to this source (see section 3.9).

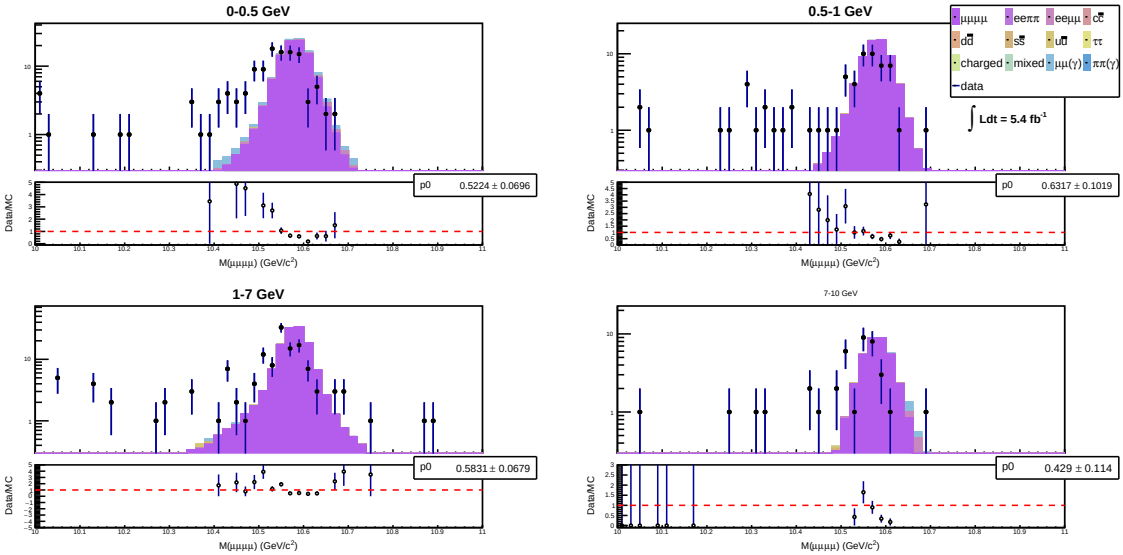

Figure 4.6: 4-track invariant mass distribution after all selections and MLP application, with data superimposed.

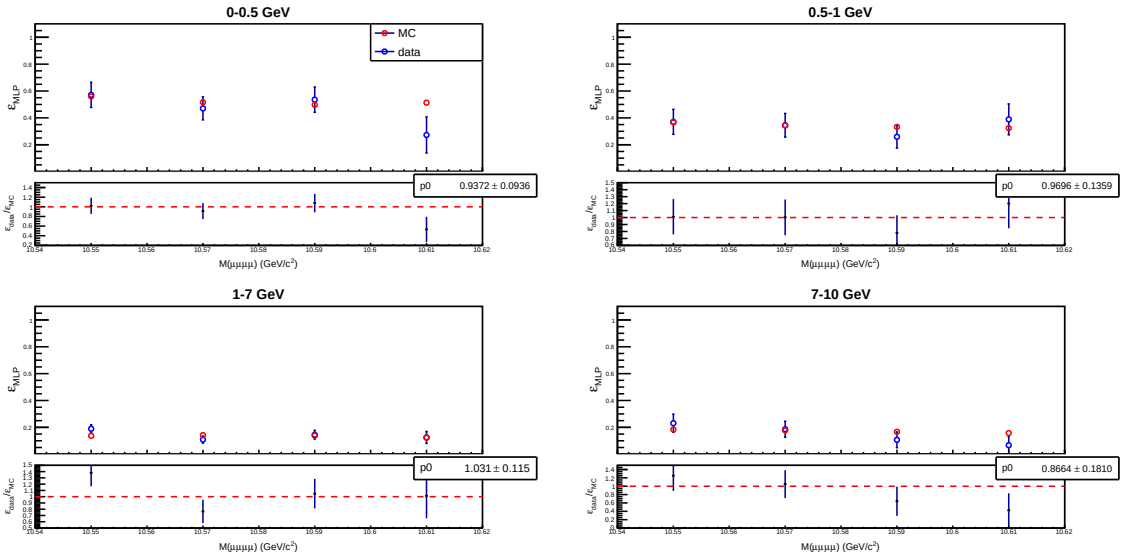

Figure 4.7: Data and MC relative MLP efficiencies as a function of the 4μ invariant mass, in the four MLP mass ranges, when a narrow cut around the υ(4S) is applied.

The invariant mass of the candidate muon pair is shown in Figure 4.8 before and after the MLP application in the four mass ranges. This is the place where to look for local excesses possibly due to the presence of a Z' decaying in two muons. Here we observe a better agreement between data and MC, not completely expected. This last point will have to be confirmed after the full luminosity studies.

A concern we had before this 10% partial unveiling was the expectation of observing large backgrounds in the low dimuon mass region, mostly due to hadronic processes, mainly through light resonances (ρ, ω, ...) with low momentum pions misidentified as muons. Such a high background was observed by Belle, but apparently not by *BABAR*. The plot in Figure 4.8 is reassuring under this respect. We think this is due to the choice of requiring three identified muons, while Belle required only two.

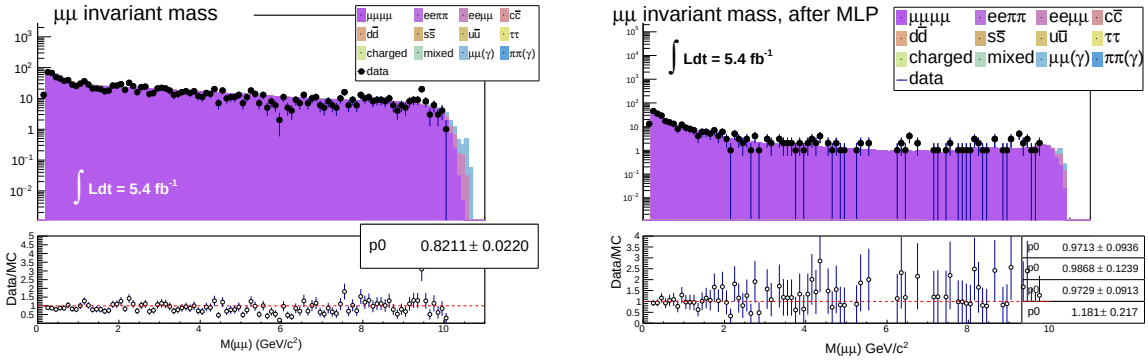

(a) Before MLP. **(b)** After MLP.

Figure 4.8: $\mu\mu$ invariant mass distribution before (Figure 4.8a) and after (Figure 4.8b) MLP, with data superimposed.

4.3 Conclusions

As the search $e^-e^- \to \mu\mu Z'(Z' \to \mu\mu)$ has already been published by *BABAR* [20] and Belle (Figure 4.9) using integrated luminosities much larger than that of Belle II, the analysis was designed and performed using a completely different approach on the background suppression, which exploits discriminant kinematic variable differences between signal and background.

It is finally demonstrated that this approach allows to get better results and more restrictive limits for Z' masses larger than 1 GeV/c^2, on the g$'$ coupling constant, with a 200 fb^{-1} integrated luminositiy, which is now the Belle II target for the journal publication.

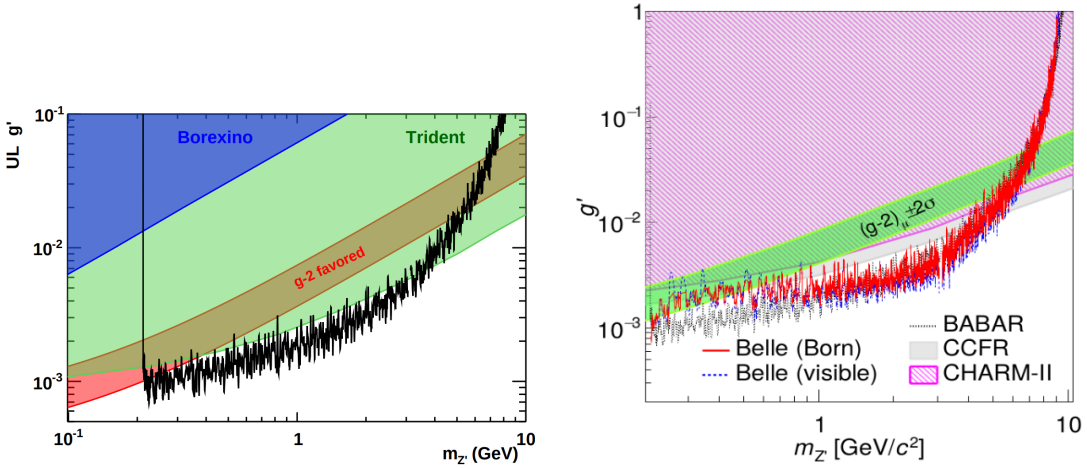

Figure 4.9: existing g$'$ upper limits on $Z' \to \mu^+\mu^-$ from *BABAR* (left) and Belle (right).

Bibliography

[1] X.-G. He, G. C. Joshi, H. Lew, and R. R. Volkas, *New Z' phenomenology*, Phys. Rev. D **43** (1991) R22–R24.

[2] X.-G. He, G. C. Joshi, H. Lew, and R. R. Volkas, *Simplest Z' model*, Phys. Rev. D **44** (1991) 2118–2132.

[3] M. Pospelov, *Secluded $U(1)$ below the weak scale*, Phys. Rev. D **80** (2009) 095002, arXiv:0811.1030 [hep-ph].

[4] B. Shuve and I. Yavin, *Dark matter progenitor: Light vector boson decay into sterile neutrinos*, Phys. Rev. D **89** (2014) 113004, arXiv:1403.2727 [hep-ph].

[5] W. Altmannshofer, S. Gori, S. Profumo, and F. S. Queiroz, *Explaining dark matter and B decay anomalies with an $L_\mu - L_\tau$ model*, Journal of High Energy Physics **2016** (2016) no. 12, 106, arXiv:1609.04026 [hep-ph].

[6] K. Akai, K. Furukawa, and H. Koiso, *SuperKEKB collider*, Nuclear Instruments and Methods in Physics Research Section A **907** (2018) 188–199, arXiv:1809.01958 [physics.acc-ph].

[7] J. Lees, V. Poireau, V. Tisserand, E. Grauges, A. Palano, G. Eigen, D. Brown, Y. G. Kolomensky, H. Koch, T. Schroeder, et al., *Search for a muonic dark force at BaBar*, Physical Review D **94** (2016) no. 1, 011102.

[8] N. Aghanim et al., Planck Collaboration, *Planck 2018 results*, AA **641** (2018) .

[9] R. Essig et al., *Dark Sectors and New, Light, Weakly-Coupled Particles*, 2013. https://arxiv.org/abs/1311.0029.

[10] V. C. Rubin, W. K. Ford, Jr., and N. Thonnard, *Rotational properties of 21 SC galaxies with a large range of luminosities and radii, from NGC 4605 (R = 4kpc) to UGC 2885 (R = 122 kpc)*, Astrophysical Journal **238** (1980) 471–487.

[11] A. G. Bergmann, V. Petrosian, and R. Lynds, *Gravitational lens models of arcs in clusters*, Astrophysical Journal **350** (1990) 23–35.

[12] J. Jaeckel and A. Ringwald, *The Low-Energy Frontier of Particle Physics*, Annual Review of Nuclear and Particle Science **60** (2010) 405–437, arXiv:1002.0329 [hep-ph].

[13] W. Altmannshofer, S. Gori, S. Profumo, and F. S. Queiroz, *Explaining dark matter and B decay anomalies with an $L_\mu - L_\tau$ model*, JHEP **12** (2016) 106, arXiv:1609.04026 [hep-ph].

[14] B. Shuve and I. Yavin, *Dark matter progenitor: Light vector boson decay into sterile neutrinos*, Phys. Rev. D **89** (2014) no. 11, 113004, arXiv:1403.2727 [hep-ph].

[15] W. Altmannshofer, S. Gori, M. Pospelov, and I. Yavin, *Quark flavor transitions in $L_\mu - L_\tau$ models*, Phys. Rev. D **89** (May, 2014) 095033. https://link.aps.org/doi/10.1103/PhysRevD.89.095033.

[16] T. Araki, S. Hoshino, T. Ota, J. Sato, and T. Shimomura, *Detecting the $L_\mu - L_\tau$ gauge boson at Belle II*, Physical Review D **95** (2017) no. 5, . http://dx.doi.org/10.1103/PhysRevD.95.055006.

[17] W. Altmannshofer, S. Gori, M. Pospelov, and I. Yavin, *Quark flavor transitions in $L_\mu - L_\tau$ models*, Physical Review D **89** (2014) no. 9, . http://dx.doi.org/10.1103/PhysRevD.89.095033.

[18] I. Adachi et al., Belle-II, *Search for an invisibly decaying Z' boson at Belle II in $e^+e^- \to \mu^+\mu^-(e^\pm\mu^\mp)$ plus missing energy final states*, arXiv:1912.11276 [hep-ex]. https://arxiv.org/abs/1912.11276.

[19] J. Lees, V. Poireau, V. Tisserand, E. Grauges, A. Palano, G. Eigen, D. Brown, M. Derdzinski, A. Giuffrida, Y. Kolomensky, and et al., *Search for Invisible Decays of a Dark Photon Produced in e+e- Collisions at BaBar*, Physical Review Letters **119** (2017) no. 13, .

[20] J. P. Lees et al., BaBar Collaboration, *Search for a muonic dark force at BaBar*, Phys. Rev. D **94** (2016) 011102, arXiv:1606.03501 [hep-ex].

[21] T. Abe et al., Belle II Collaboration, *Belle II Technical Design Report*, arXiv:1011.0352 [physics.ins-det].

[22] E. Kou, P. Urquijo, et al., *The Belle II Physics Book*, Progress of Theoretical and Experimental Physic **2019** (2018) no. 12, 123C01, arXiv:1808.10567 [hep-ex].

[23] S. Agostinelli et al., GEANT4 Collaboration, *GEANT4 - a simulation toolkit*, Nuclear Instruments and Methods in Physics Research Section A **506** (2003) 250–303.

[24] J. Alwall, R. Frederix, S. Frixione, V. Hirschi, F. Maltoni, O. Mattelaer, H.-S. Shao, T. Stelzer, P. Torrielli, and M. Zaro, *The automated computation of tree-level and next-to-leading order differential cross sections, and their matching to parton shower simulations*, Journal of High Energy Physics **2014** (2014) no. 7, 79, arXiv:1405.0301 [hep-ph].

[25] W. Verkerke and D. P. Kirkby, *The RooFit toolkit for data modeling*, eConf **C0303241** (2003) MOLT007, arXiv:physics/0306116 [physics].

[26] J. Alwall, R. Frederix, S. Frixione, V. Hirschi, F. Maltoni, O. Mattelaer, H.-S. Shao, T. Stelzer, P. Torrielli, and M. Zaro, *The automated computation of tree-level and next-to-leading order differential cross sections, and their matching to parton shower simulations*, Journal of High Energy Physics **2014** (Jul, 2014) . http://dx.doi.org/10.1007/JHEP07(2014)079.

[27] F. A. Berends, P. H. Daverveldt, and R. Kleiss, *Complete lowest-order calculations for four-lepton final states in electron-positron collisions*, Nuclear Physics B **253** (1985) 441–463.

[28] S. Jadach, B. F. L. Ward, and Z. Was, *The precision Monte Carlo event generator KK for two-fermion final states in e^+e^- collisions*, Computer Physics Communications **130** (2000) no. 3, 260–325, arXiv:hep-ph/9912214 [hep-ph].

[29] N. Davidson, G. Nanava, T. Przedziński, E. Richter-Was, and Z. Was, *Universal interface of TAUOLA: Technical and physics documentation*, Computer Physics Communications **183** (2012) no. 3, 821–843, arXiv:1002.0543 [hep-ph].

[30] H. Czyż, M. Gunia, and J. H. Kühn, *Simulation of electron-positron annihilation into hadrons with the event generator PHOKHARA*, Journal of High Energy Physics **2013** (2013) no. 8, 110, arXiv:1306.1985 [hep-ph].

[31] G. Punzi, *Sensitivity of searches for new signals and its optimization*, eConf **C030908** (2003) MODT002, arXiv:physics/0308063.

[32] T. Ferber, OrcaKinFit*: Kinematic Fitting for Belle II*, 2017. BELLE2-NOTE-PH-2017-002.

[33] T. Kuhr, C. Pulvermacher, M. Ritter, T. Hauth, and N. Braun, Belle II Framework Software Group, *The Belle II Core Software*, Computing and Software for Big Science **3** (2019) no. 1, 1, arXiv:1809.04299 [physics.comp-ph].